# REFINING CRYSTAL SIZE DISTRIBUTIONS AND KINETIC HISTORIES USING AUTOMATED SCANNING ELECTRON MICROSCOPY AND MANUAL METHODS: A HYBRID APPROACH

by

Kim A. Cone

A thesis submitted to the Faculty and the Board of Trustees of the Colorado School of Mines in partial fulfillment of the requirements for the degree of Master of Science (Geology).

Golden, Colorado

Date _____

Signed: _____
Kim A. Cone

Signed: _____
Dr. Richard F. Wendlandt
Thesis Advisor

Golden, Colorado

Date _____

Signed: _____
Dr. M. Stephen Enders
Professor and Department Head
Department of Geology and Geological Engineering

ABSTRACT

Igneous rock textures are directly tied to pre-, syn- and post-eruptive processes that occur throughout the evolution of a melt. One aspect of texture concerns crystal size distributions (CSDs), which are volume-based, individual counts of crystals from a defined volume of rock. CSDs provide insight into the kinetic evolution of igneous rocks. Direct measurements of crystal volumes from rock samples are often impractical, forcing the use of crystal lengths from thin sections as proxies for crystal volumes. We use a combination of manual tracing and automated SEM-based methods to delineate crystal borders while software (ImageJ, CSDSlice and CSDCorrections) addresses direct length acquisition and stereological conversions. Using texturally diverse lava samples, we demonstrate that this hybrid approach 1) preserves the crystal-length accuracy of manually traced phenocrysts while 2) refining groundmass crystal lengths through automated SEM-based analysis. High-resolution SEM-based imaging produces groundmass crystal length that refine nucleation densities when compared to back-extrapolations from manually-derived CSD curves. Using energy-dispersive X-ray spectroscopy to produce crystal images permits population size characterization by geochemistry while electron backscatter diffraction images allow detection of discrete crystals within complexly twinned plagioclase crystal clusters using lattice orientation. CSD curves from lava samples suggest that manual methods often produce reduced and misleading nucleation densities and shallower CSD slopes, which in turn decrease apparent average residence times. The hybrid method preserves the integrity of the portions of CSDs represented by manually traced crystals while introducing improved resolution of CSDs at the finer size fraction.

TABLE OF CONTENTS

LIST OF FIGURES

LIST OF TABLES

ACKNOWLEDGEMENTS

I would like to thank Dr. Richard Wendlandt, my advisor, for the opportunity to serve as his teaching assistant for three years. I learned that I certainly did not learn half as much as an undergrad in my mineralogy and petrology classes as I did being a teaching assistant for Dr. Wendlandt. I learned to become a more effective teacher in the process and to appreciate (and cope with) the eccentricities of our talented undergraduates. An additional thank you for introducing the Cashman and Marsh (1988) paper in the graduate igneous petrology class that sparked this project. And of course, for the project samples from Iceland and the generous funding over the years.

Thank you to my committee members, Dr. Katharina Pfaff and Dr. Wendy Harrison, for the valuable feedback on thesis revisions and for pulling me away from my sometimes myopic focus.

I'd also like to thank the following: Jae Erickson, our relentless thin section lab manager; Tyler Brown at the University of Wyoming Materials Characterization Lab, for introducing me to beginning EBSD and for taking the time on weekends to assist even though he was busy with his own PhD research; and Omero "Phil" Orlandini at UC Boulder, for the multiple discussions and email exchanges on EBSD and for being a MTEX/MATLAB wiz. Without his help, the EBSD portion of my work would have remained [more] incomplete. Finally, I want to thank the following researchers for their email correspondence (as the crystal size distribution analysis crowd remains somewhat scattered and few in number, their feedback kept me on the right track and provided much needed clarification): Dr. Michael Higgins, Dr. Brush Marsh and Dr. Daniel Morgan, all CSD gods. To all of the undergraduates I've met through Mineralogy and Petrology labs, you've thoroughly entertained and/or challenged me, and I am doubtless that I will find myself teaching in the near future.

# CHAPTER 1

# GENERAL INTRODUCTION

## 1.1 Introduction

This research focuses on an aspect of textural analysis using crystal size distribution theory (CSD theory). The theory links volumetrically-based crystal population counts of a single phase to an ideal crystallization environment. In this research, an open steady-state system defined by constant nucleation and growth is assumed as the ideal crystallization environment for four basaltic lava samples from the large volume 1783-1784 Laki fissure eruptions in Iceland. Length measurements of plagioclase crystals are obtained using a combination of manual and SEM (scanning electron microscopy)-based methods to produce CSD plots. Although the more traditional method of manually tracing crystals from digital images can produce accurate crystal lengths for CSD plots, the process is time-consuming and introduces user bias. Automated SEM-based methods offer an approach to eliminating user bias while increasing efficiency and accuracy in obtaining crystal lengths. The methods explored here involve the use of two automated SEM-based techniques (automated mineralogy and electron backscatter diffraction (EBSD)) as well as freeware programs ImageJ (Schneider et al., 2012), CSDSlice (Morgan and Jerram 2006) and CSDCorrections (Higgins 2000, 2006). To create CSD plots, the two main aspects involve 1) obtaining crystal length measurements from photomicrographs and from either element-based digital images (automated mineralogy) or orientation-based digital images (EBSD), and 2) converting those measurements to discrete crystal volumes using the above software.

The conversion of lengths derived from two-dimensional thin-sections to meaningful volumetric equivalents is not straightforward for shapes other than spheres. This problem falls into the field of stereology, which attempts to interpret some aspect of three-dimensionality from two-dimensional planar cuts of objects. For this purpose, CSDSlice and CSDCorrections are used to address stereological issues from both modelling and mathematical perspectives, respectively. Using a combination of methods on texturally diverse, well-characterized lava samples, a new hybrid approach is described here that extracts

plagioclase crystal lengths to produce more accurate CSD plots than can be created from lengths derived from manual methods alone.

## 1.2 Thesis Organization

There are two overarching parts to this thesis: 1) methods development and 2) application of those methods on igneous rock samples. The first part involves the instrumentation and methods used to obtain crystal size distributions for the Laki basalts and centers around 1) manual methods, 2) automated SEM-based imaging, as well as 3) a foray into electron backscatter diffraction analysis. The second part focuses on the application of the above methods to obtain crystal size distributions from natural samples.

Chapters 2 and 3 consist of manuscripts for future submission to *American Mineralogist* but may be modified for submission to other journals. Chapter 2 focuses on methods development and integration of manual and automated approaches for obtaining crystal size distributions from two texturally diverse lava samples. Chapter 3 focuses on the interpretation of crystal size distributions of the four Laki basalt samples using methods from Chapter 2. Kim Cone is the primary author (Master of Science student, Colorado School of Mines). Co-authors for the final manuscript submission will include Dr. Richard F. Wendlandt (professor, Colorado School of Mines), Dr. Katharina Pfaff (Assistant Research Professor, Colorado School of Mines), and Omero Felipe Orlandini (PhD candidate, University of Colorado, Boulder).

Chapter 4 is a summary conclusion that draws from chapters 2 and 3.

Appendix A contains full thin section scans and Appendix B contains the MTEX MATLAB script used to address plagioclase twinning in EBSD analysis.

CHAPTER 2

# EXPLORING AUTOMATED SEM-BASED METHODS FOR REFINING CRYSTAL SIZE DISTRIBUTIONS: A HYBRID APPROACH

A paper to be submitted to *American Mineralogist*

K A. Cone, R. F. Wendlandt, K. Pfaff, O. F. Orlandini

## 2.1 Abstract

Igneous textures are records of melt chemistry, temperature and pressure conditions, volatile contents, and the physical dynamics of pre-, syn- and post-eruptive processes. Textural analysis therefore can reveal aspects of conditions under which rocks crystallize. One type of textural analysis involves the counts of crystals as reflected by their individual volumes. These counts produce what is known as a crystal size distribution (CSD). Crystal size distributions (CSDs) in igneous rocks reflect the interplay of mechanical processes that occur throughout crystallization and are crucial for a complete understanding of the evolution of volcanic eruptions. Producing CSD plots involves obtaining accurate crystal volumes. In many cases, direct measurements are not feasible and so crystal length measurements from thin sections are used as proxies for volumes. Obtaining lengths from a thin section traditionally involves manual tracing of crystals from photomicrographs or backscatter electron (BSE) images. The suitability of such images is dependent on both the mineral used and texture of the sample. In the case of plagioclase in lava samples (which we use here), textural aspects such as 1) crystal sizes that are too small to accurately resolve in photomicrographs and 2) crystal clustering, can discourage the use of CSDs to characterize igneous samples. Automated mineralogy and EBSD can assist in both reducing the time required to obtain crystal lengths while increasing the accuracy of CSD plots by refining the smallest-size crystal fraction. A hybrid method combining crystal lengths derived from both manual tracings of photomicrographs and SEM-based images provides an optimal approach that exploits the strengths of the individual methods to produce more accurate CSD plots. Kinetic parameters teased from CSD plots such as nucleation population and residence times are therefore improved and can reveal subtle differences in crystallization environments for samples that appear texturally similar.

## 2.2 Introduction

Textural analysis is essential for understanding many geologic processes. An increasingly common tool for gaining insight into crystallization dynamics is the use of crystal size distributions (Marsh, 1988, 1998; Cashman and Marsh, 1988; Higgins, 2000, 2006). Petrologic studies that focus on geochemistry and phase equilibria as primary means to explore geologic questions can utilize textural analysis through crystal size distributions, as texture lends insight into the evolution of magma systems and eruptive processes.

For a steady-state, open igneous system, there is an ideal linear relationship between crystal population count and crystal size, when displayed on a log-linear plot. Natural lava samples mimic this relationship, where crystals constantly nucleate and grow through size populations, producing what is ideally a seriate texture. This is mathematically and graphically shown by the following:

$$\ln (n(L)) = - L/(G\tau) + \ln (n^0) \quad (1)$$

where the first term is the population density, L is the 3D length (usually confined to interpreting measurements derived from thin sections), G is the average crystal growth rate (often assumed from experimental values (Kirkpatrick, 1977; Cashman, 1993; Cashman and Marsh, 1988), $\tau$ is the residence time, and $n^0$ is the nucleation density. Other characteristics may be determined from the equation: characteristic length (C) can be calculated as $G\tau$, and nucleation rate (J) is equivalent to $n^0G$.

Plagioclase is a ubiquitous phase in lavas and serves as a sensitive fingerprint of changes in melt conditions and in physical processes (e.g. magma mixing and crystal settling). Because it often nucleates and grows over a wide temperature and pressure regime during the eruptive process, polydisperse populations (multiple true sizes) and multiple aspect ratios are common in volcanic products (Guilbaud et al., 2007; Neave et al., 2013) and can reflect different cooling rates (Brugger and Hammer, 2010 and references therein). Fast-cooling upon eruption often produces anhedral plagioclase microlites (Brugger and Hammer, 2015) with swallowtail morphology and twinning styles that may point to conditions of crystallization and growth histories (Xu et al., 2016). Multiple plagioclase habits in a single sample are often treated with stereological corrections in order to produce meaningful CSDs, as true crystal lengths

that represent actual three-dimensional crystal (3D) volumes are not represented in two-dimensional (2D) thin sections. Lava flow textures may suggest localized regions of crystal preferred orientation in photomicrographs, and so stereological interpretations of length measurements from 2D thin sections may be subsequently affected.

Various aspects of CSD analysis have been examined over the last 30 years since the seminal works of Marsh (1988) and Cashman and Marsh (1988) on the Makaopuhi lava lake, having borrowed the idea of crystal population balance from the field of chemical engineering (Randolph and Larson, 1971). Recent topics include confocal microscopy and microlite measurement in thin section (Castro et al., 2003), stereological corrections concerning cut section effects and intersection probability effects (Higgins, 2000, 2006; Mock and Jerram, 2005; Morgan and Jerram, 2006), decompression-induced twinning styles in plagioclase microlites as revealed by electron backscatter diffraction (EBSD) analysis (Brugger and Hammer, 2015), and most recently the use of automated mineralogy in obtaining CSDs from plagioclase populations in a large volume lava eruption (Neave et al., 2017). Although manual methods are considered the most reliable (and the least expensive) means of obtaining crystal length measurements, this process can be time consuming when manually tracing tens of thousands of crystals from photomicrographs or BSE images. Manual tracing by multiple users for multiple images from a single sample introduces not only user bias in measurements, but also bias in distinguishing discrete plagioclase crystals within crystal clusters (glomerocrysts). At the pixel scale, crystal borders may be indistinct in digital images and difficult to consistently determine. As a result, CSD analysis for igneous rocks is often confined to measuring visually-distinct phenocryst populations while the groundmass size populations are interpreted by back-extrapolation from phenocryst-based CSD curves. Even phenocrysts that exist as monomineralic clusters are often treated for the purpose of manual tracing as single entities (i.e. the entire cluster is treated as a single crystal) which they are clearly not.

The purpose of this paper is to explore the creation of CSD plots using a combination of both manual and automated SEM-based methods. The lengths of plagioclase crystals of four lava samples from the Laki fissure eruptions of 1783-1784 provide the textural variety necessary against which to test the

methods developed here. The geochemical characteristics are well-constrained across multiple research for the Laki region (Bindeman et al., 2006; Guildbaud et al., 2007; Passmore et al., 2012; Neave et al., 2013; and Neave et al., 2017). The Laki flows are tholeiitic and consist of plagioclase, clinopyroxene, olivine, and titanomagnetite.

### 2.3 The Laki fissure eruptions of 1783-1784

The eight-month long fissure eruptions in the Eastern Volcanic Zone of Iceland lasted from June 8, 1783 to February 7, 1784 and produced ~15.1 $km^3$ of lava, covering 565 $km^2$. Ten separate eruptions coincided with the creation of ten partially-overlapping, en-echelon fissures trending northeast-southwest, produced as a result of spreading between the North American and European plates (Thordarson and Self, 1993; Figs. 2.1 and 2.2). Earthquake swarms began in May of 1783 as the fissure system began to propagate northeast toward Grímsvötn, followed by the first eruptive episode in June. The ten discrete eruptive episodes were recorded based on preserved tephra deposits, stratigraphy, and historical accounts, with each episode experiencing an initial stage of phreatomagmatic explosivity caused by the high position of the water table. Eruptive styles changed to sub-Plinian and then to Hawaiian activity as the water table lowered (Thordarson and Self, 1993). The first five episodes (and hence the first five fissures) occurred on the southwest side of Laki mountain and produced magma that discharged toward the south within the Skaftá river gorge. The last five episodes occurred on the northeast side of Laki and were channeled southward within the Hverfisfljót river gorge.

Early research suggested isotopic and trace element homogeneity and a quartz-normative composition (Sigmarsson et al., 1991). Later research by Passmore et al. (2012) considered forty-seven basalt samples and seven tephra samples across the entire ten-fissure event in an extensive determination of major, minor, and trace element concentrations. They found that crystal mush entrainment was greater on average at later stages of the eruption, coinciding with the presence of anorthitic plagioclase (Passmore et al., 2012; Neave et al., 2013). Neave et al. (2013) investigated the relationship between crystal and carrier melt for the Laki system and suggested that trace element analysis of olivine-hosted melt inclusions pointed to concurrent mixing and crystallization of different sources. They concluded that

zoned plagioclase cores were the most primitive in composition of all macrocrysts and that these crystals originated in the shallow mantle.

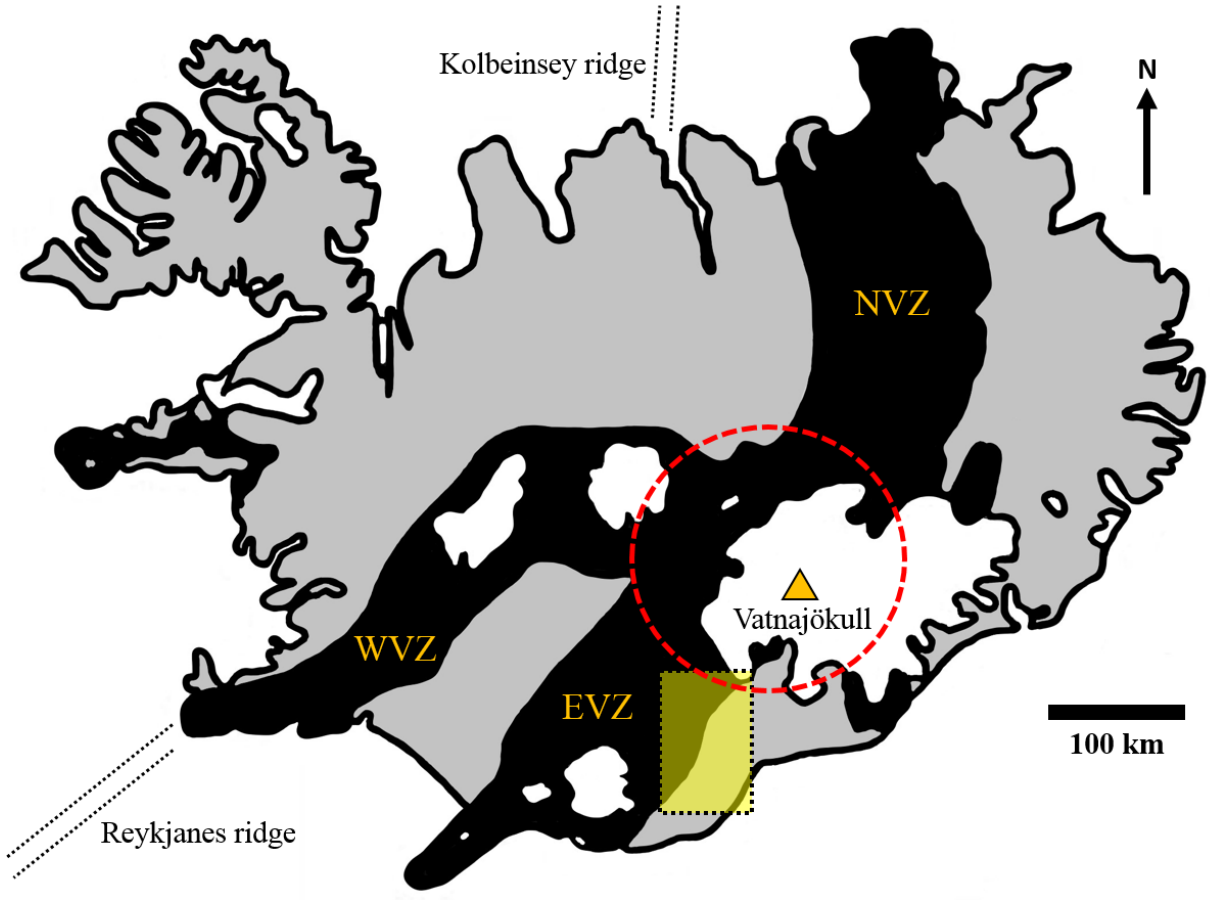


Fig. 2.1. The Neovolcanic Zone of Iceland. The Neovolcanic zone (in black) is defined as a set of three tectonically and volcanically active belts that were created during the early Cenozoic through today; they include the Eastern Volcanic Zone (EVZ), Western Volcanic Zone (WVZ), and the Northern Volcanic Zone (NVZ). The shaded yellow region represents the area shown in Figure 2.2 where the four samples were collected. The red dashed circle indicates the approximate region of the underlying mantle plume, derived from Thordarson and Höskuldsson (2008). The orange triangle represents Grímsvötn. Internal white areas represent glaciers. The dotted black lines to the north and southwest show the approximate locations and directions of the northern and southwest oceanic rift zones. The general outline of Iceland and the Neovolcanic Zone locations are modified from Passmore et al. (2012).

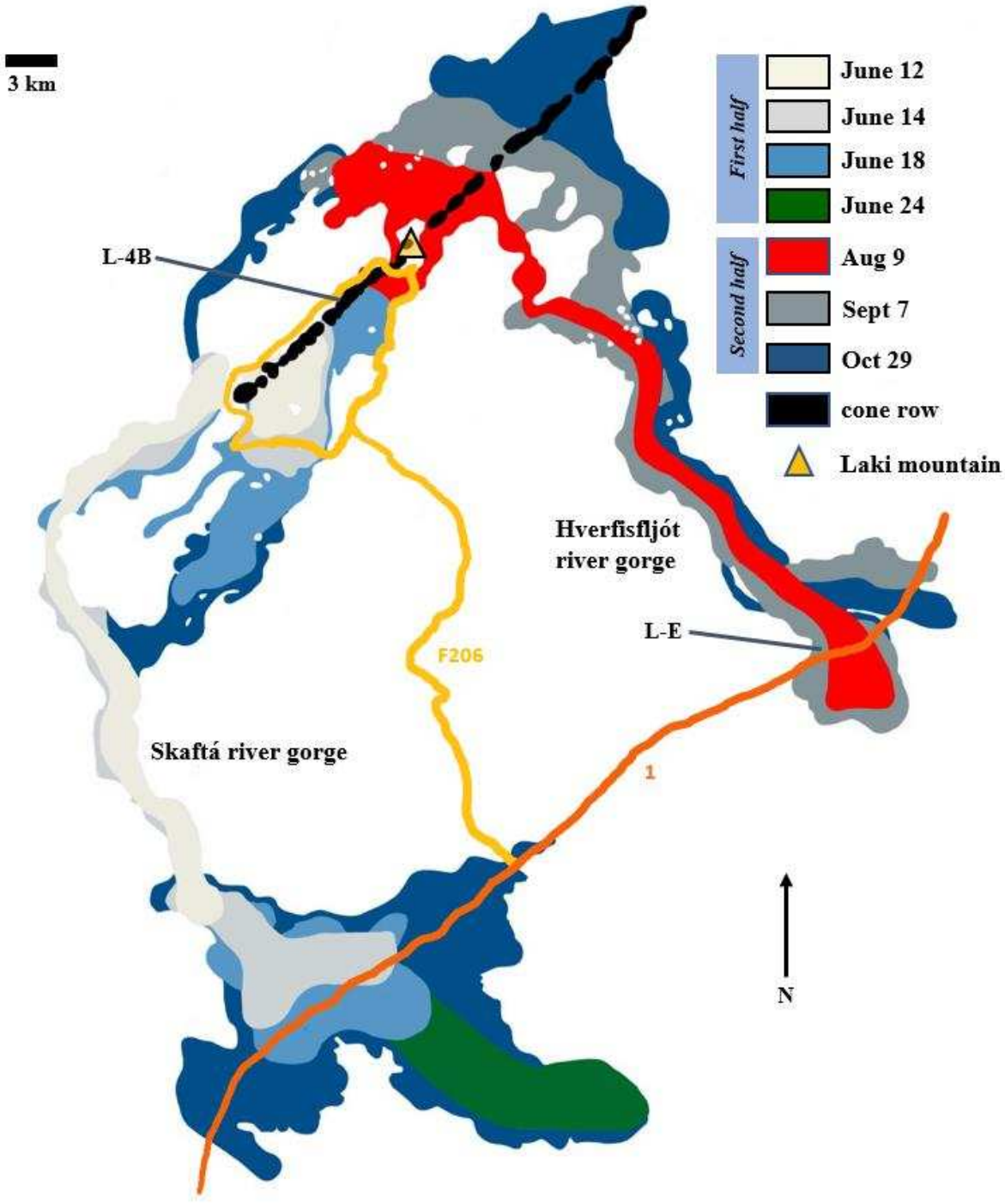


Fig. 2.2. The Laki flow branches and dates of occurrence, with locations for L-4B and L-E. The triangle at the center of the cone row represents Laki mountain which is used to define the NE and SW fissure boundary. Route locations are approximate. Figure modified from Passmore et al. (2012).
.

## 2.4 Sample characteristics

Two samples (L-4B and L-E) were collected along roadways F206 and Route 1 (Fig. 2.2), representing varieties of vesiculated, microporphyritic basalt textures from both the first and second halves of the eight-month long Laki eruption. L-4B is proximal to its originating fissures and was produced during the first half (the first five eruptions). L-E is a distal sample produced during the second half. Both samples contain plagioclase, clinopyroxene, olivine and dendritic magnetite. Dendritic magnetite only occurs in the groundmass while plagioclase, clinopyroxene and olivine occur as both phenocryst and groundmass. Sample L-4B contains the finest groundmass and provides the starkest contrast between phenocryst and groundmass crystal population sizes, appearing classically bimodal. L-E contains the coarsest groundmass with a sub-seriate crystal population. Since a central focus of this paper concerns how groundmass-dominated and phenocryst-dominated textures shape CSD plots, L-4B and L-E are suitable as they represent two extreme variations of volcanic texture (exceptionally fine-grained and coarsely seriate microporphyritic basalts, respectively). Based on initial optical microscopy observations, L-4B contains discrete plagioclase phenocrysts up to ~0.70 mm, close to that of L-E's maximum crystal length of ~ 0.80 mm. In both samples, the dominant shape of discrete plagioclase crystals is subhedral to euhedral. Plagioclase-only clusters attain maximum lengths of up to ~3.5 mm in L-E and ~2.0 mm in L-4B. With clusters involving plagioclase and clinopyroxene (with or without olivine), cluster lengths were slightly smaller in L-4B as well. Tables 2.1 and 2.2 present summaries of major textural characteristics for both samples' phenocrysts. Figures 2.3, 2.4 and 2.5 show the various types of phenocrysts that occur in L-4B and L-E.

Table 2.1. Major characteristics of discrete-style (single crystal) phenocrysts. For sample L-E, rare, tabular occurrences of internally, strongly sieved plagioclase crystals occur.

| Laki basalt phenocryst characteristics (Discrete) | | | |
|---|---|---|---|
| Sample | Phase | ~Size (mm) | Shape |
| L-4B | pl | up to 0.70 | subhedral to euhedral |
| | cpx | up to 0.15 | euhedral, equant |
| | ol | up to 0.30 | subhedral, equant to subequant |
| L-E | pl | up to 0.80 | subhedral to euhedral |
| | cpx | up to 0.30 | equant |
| | ol | up to 0.45 | subhedral euhedral |

Table 2.2. Major characteristics of cluster-style phenocrysts.

| Laki basalt phenocryst characteristics (Cluster) | | | |
|---|---|---|---|
| Sample | Style | ~Size (mm) | Texture/Observations |
| L-4B | pl-only | up to 2.0 | sometimes continuous extinction; zoned and twinned |
| | cpx-only | up to .25 | clusters of two to four crystals |
| | pl+cpx | up to 1.35 | often sub-ophitic with smaller occurrences larger ones are discrete-discrete clusters |
| | pl+cpx+ol | up to 0.40 | rare |
| L-E | pl-only | up to 3.5 | microlite flow alignment around largest cluster/s (product of two joined discrete-clusters?) |
| | cpx-only | up to 0.40 | up to three contiguous members |
| | pl+cpx | up to 2.0 | often sub-ophitic; largest cluster contains largest cpx crystals, up to 1.1mm |
| | pl+cpx+ol | up to 0.90 | rarely observed |

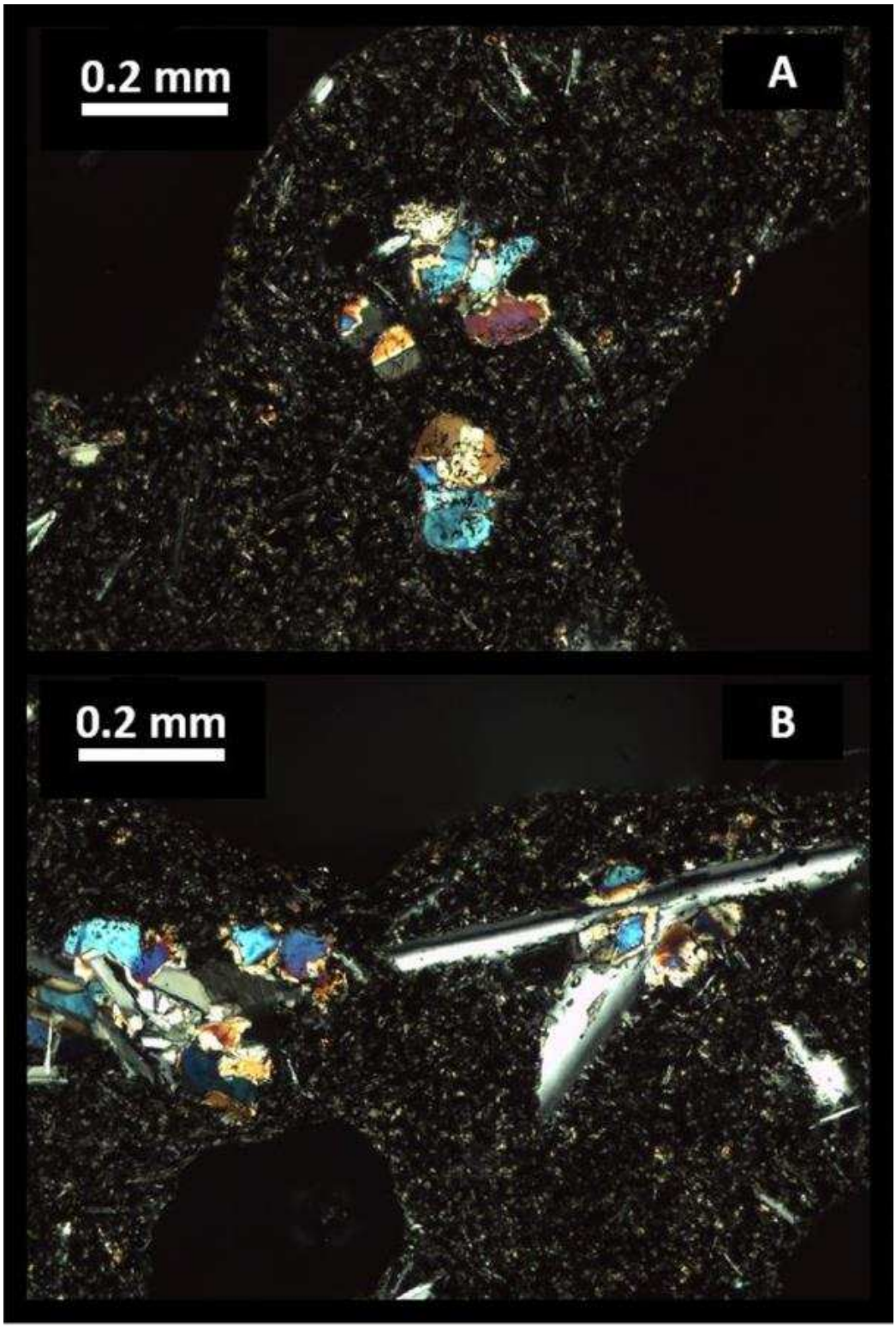


Fig. 2.3. Discrete crystals within crystal clusters in Sample L-4B, cross polarized light. Image A shows typical all-cpx clusters as well as isolated cpx crystals (center-left, twinned). Image B shows the common occurrence of pl+cpx clusters. The cluster on the right shows elongated plagioclase with indistinct boundaries.

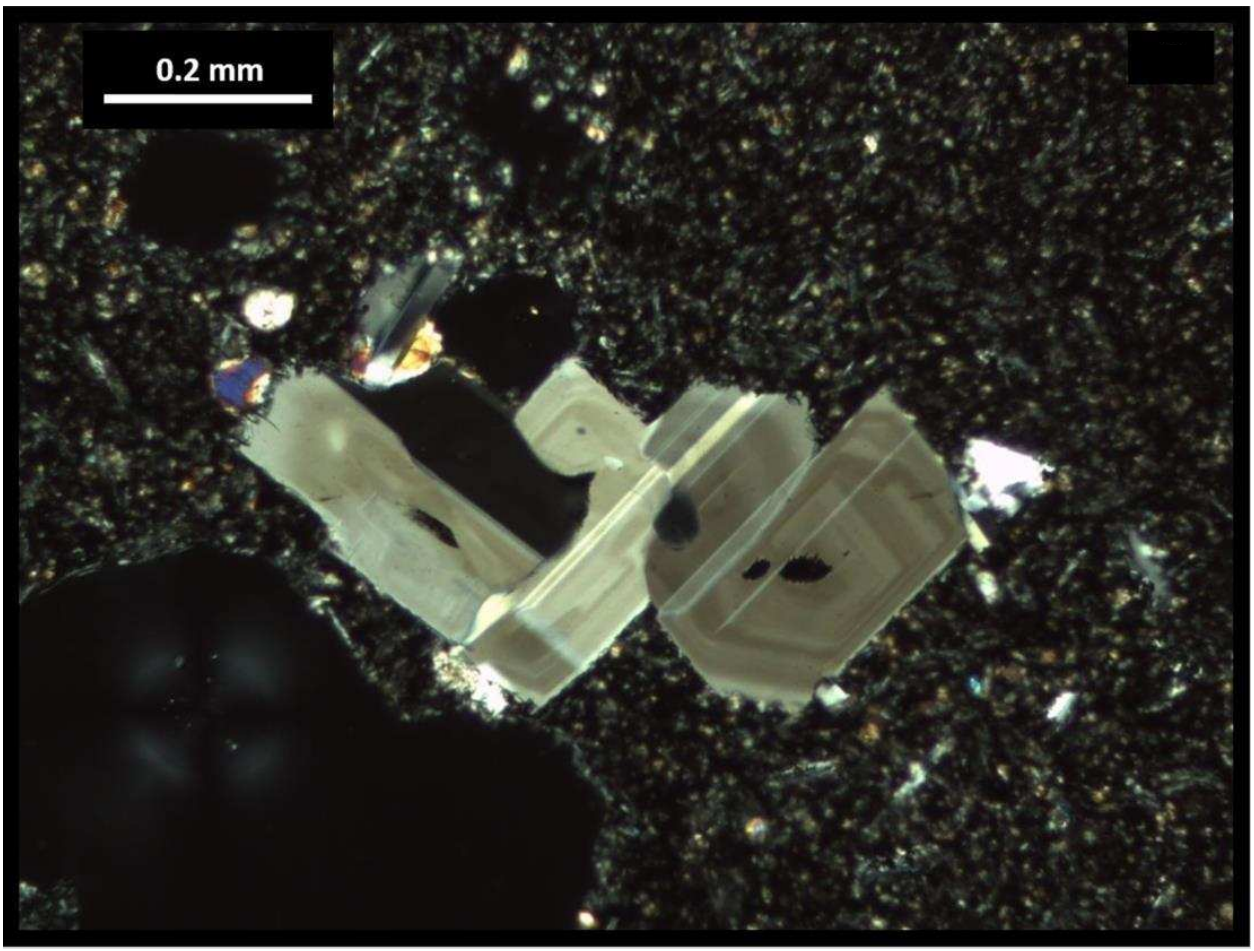


Fig. 2.4. An all-plagioclase glomerocryst from sample L-4B, cross polarized light. Note the strong degree of optical continuity as suggested by shared extinction behavior. This continuity suggests that the individual crystals within the cluster are similarly oriented.

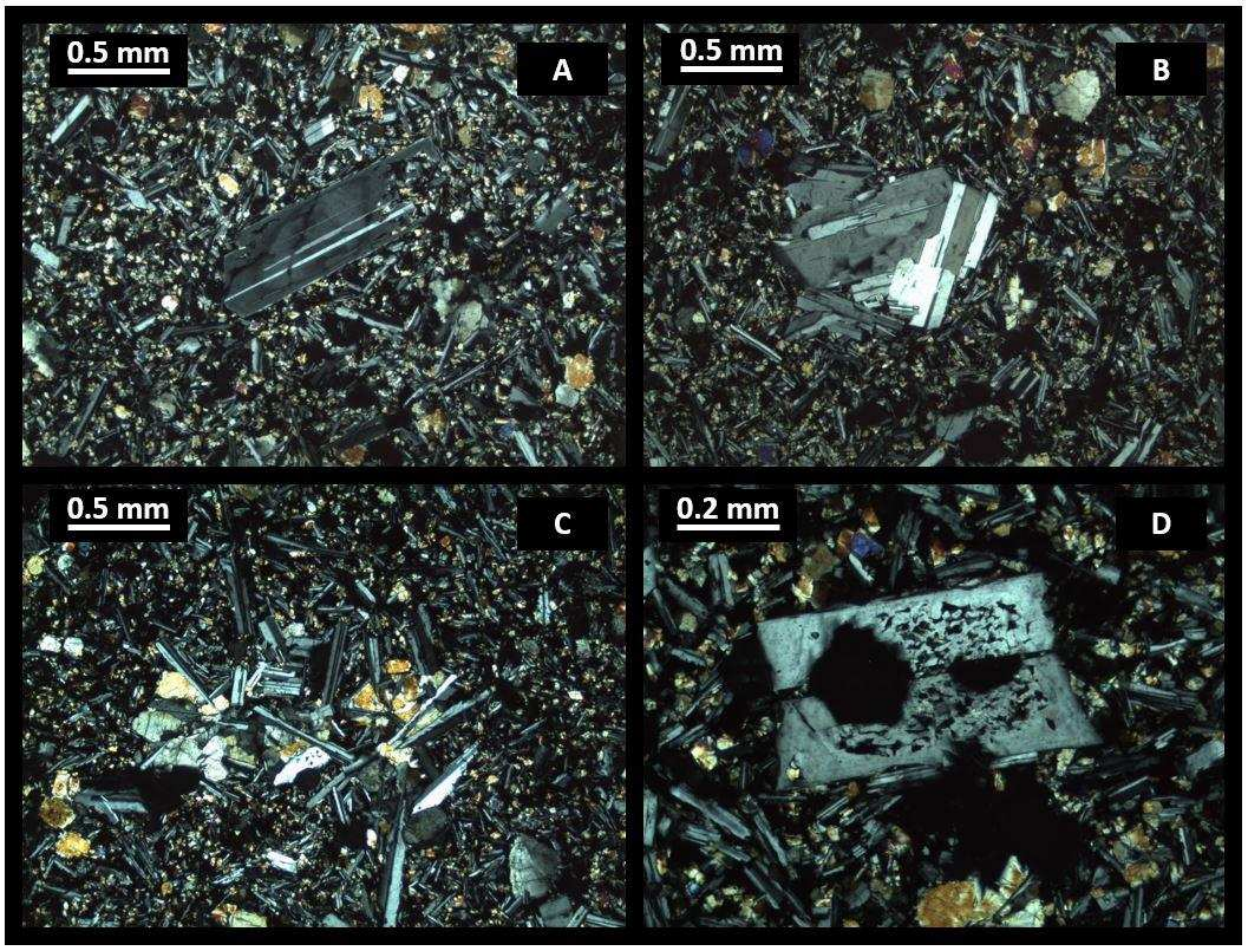


Fig. 2.5. Discrete crystals and crystal cluster types in sample L-E, cross polarized light. Crystal cluster types are similar to those of L-4B. Note in D the pronounced internal sieving of the discrete plagioclase phenocryst, suggesting disequilibrium conditions. A and B show discrete and cluster styles of plagioclase, respectively. C shows a slight variation of pl+cpx clustering, where plagioclase microlites are highly elongate.

## 2.5 Automated SEM-based imaging

SEM-based images can be acquired from software-controlled systems that scan user-defined areas of a polished sample and automatically stitch together multiple scanned fields to produce a larger pixel-based image. Automated SEM-based imaging is capable of producing phase images from elemental information (Gottlieb, 2000). The phase images can then be used as crystal images from which crystal

lengths can be extracted. The user must establish a reliable protocol for defining the sought-after phase, but once completed, the protocol can be reused for the same phase from multiple samples.

The term "automated mineralogy" is often used to refer to a specific set of SEM-based systems (brands QEMSCAN, MLA and TESCAN TIMA, for example). The early use of automated SEM systems focused on mineral processing and ore identification in an attempt to optimize ore release from natural samples (Sutherland, 2007; Gu, 2003). This type of use remains dominant today (Gu et al., 2014). Each system has proprietary software that automates the scanning process while providing information such as particle size and area. Separate detectors for BSE and EDX (energy-dispersive x-ray spectroscopy) images are commonly part of the systems, but other detectors such as cathode luminescence (CL) detectors may be installed. However, SEM-based systems that possess some degree of automation are now commonly used across sub-disciplines in petrology, and so the use of the expression "automated mineralogy" is being increasingly abandoned in some areas of igneous petrology for more general expressions such as "automated SEM-based analysis" or "automated analysis". In this research, TESCAN TIMA (Tescan Integrated Mineral Analyser) and EBSD SEM-based automated systems are employed to obtain lengths from plagioclase crystals. Both systems produce phase images using different information about plagioclase. TIMA will produce plagioclase images based on elemental composition whereas EBSD produces information based on crystallographic orientation.

### 2.6 Materials and thin section preparation

Two orthogonally oriented thin sections were prepared from each of the two lava samples. Group A thin sections (L-4B and L-E) consisted of the original cut surface while group B thin sections (V4 and V1) consisted of lengthwise orthogonal cuts produced from the remaining billets of group A (Fig. 2.6). Orthogonal cuts can assist in fabric detection when statistically significant similarities in crystal orientations are present. Although three orthogonal cuts are ideal, we were limited to two here due to small hand sample sizes. Proximal orthogonal cuts can also assist in detecting localized fabric variations when analysis is performed along similar regions between the original and orthogonally prepared thin section. L-E and L-4B were prepared by Wagner Petrographics, Utah and polished to .25 µm. L-E also

incurred a final polish with 0.05 µm colloidal silica for ~20 hours on a Buehler Vibromet 2 vibratory polisher at 70% amplitude at the University of Wyoming's Material Characterization Laboratory. Thin sections V1 and V4 were prepared by the Colorado School of Mines' Thin Section Laboratory and polished with 0.05 µm alumina. All thin sections received a carbon coat to prevent charging during scans.

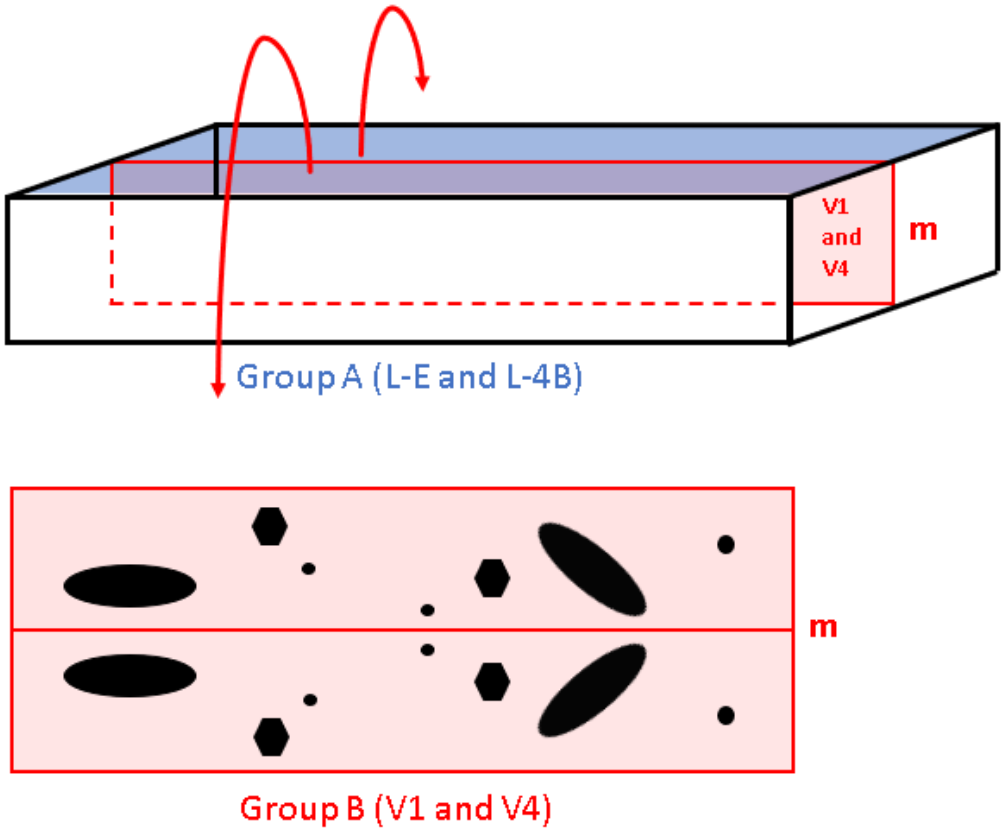


Fig. 2.6. The original billets from L-4B and L-E (the orientations of which is indicated by the blue plane in the top figure) were cut lengthwise down the center and opened and rotated 90° in the direction of the arrows, with the newly exposed faces (red surface in the bottom and top figure) serving as the new surfaces of orthogonally oriented V4 and V1, respectively.

## 2.7 Methods

### 2.7.1 Overview for determining crystal size distributions

CSD plots began with the acquisition of plagioclase crystal length measurements from digital images. Four types of digital images were produced: 1) photomicrographs, 2) BSE images, 3) TIMA phase images

and 3) EBSD orientation images. Plagioclase phenocrysts were manually traced in photomicrographs using Adobe Photoshop. For BSE, TIMA and EBSD images, no tracing was performed. All four image types were then imported into ImageJ freeware (Schneider et al., 2012). ImageJ is an image processing program which can determine length measurements after images are converted to grayscale (i.e. thresholding). Measurements from ImageJ were then imported into CSDSlice (where indicated), a program which determines a statistical best-fit aspect ratio for a group of length measurements. The program reflects the results of modelling cut sections through different crystal habits. The five most statistically significant aspect ratios are returned with their corresponding $R^2$ values in the form x: y: z, representing the short, intermediate, and long axes measurements (symbolized by S: I: L). A thorough discussion of CSDSlice is contained in (Morgan and Jerram, 2006). Since groundmass plagioclase and the larger phenocryst populations often have different shapes, particles were analyzed for our samples as two distinct populations in CSDSlice, separated by a size threshold of 150 µm as determined by previous research of Laki lavas (Passmore et al., 2012; Neave et al, 2013). At least 75 crystal sections are required in order to determine a robust best-fit aspect ratio for tabular crystals and at least 250 crystal sections for acicular ones (Morgan and Jerram, 2006).

Length measurements from ImageJ along with CSDSlice aspect ratios are then input into CSDCorrections (Higgins, 2000, 2006), a program that converts the ImageJ-derived measurements into true 3D volumetric equivalents by correcting for two effects: 1) the intersection-probability effect where smaller crystals are less likely to be intersected than larger ones, and for 2) the cut-section effect where the greatest length measurements are rarely reflected by random cuts (i.e. a particle is rarely to reflect maximum size). The program also corrects for vesicle/void percent and considers the area of the thin section analyzed. CSDs are determined in part based on bin widths that can be adjusted from two to ten bins per decade in CSDCorrections. Here, we use a minimum of five bins per decade (unless stated otherwise) to reduce uncertainty attributed to either using an increased number of smaller bins or to having an insufficient sample population. For the population density on the y-axis, the crystal count in each bin from the x-axis is divided by the area of the thin section on a vesicle-free basis. That value is

further divided by the bin width. The result is a unit of $mm^{-4}$ for population density. A characteristic length, C, is generated as well as the associated regression slope (-1/C) and a nucleation population density value of ln ($n^0$).

There are multiple approaches for obtaining an apparent length measurement from a 2D cut section with the goal that the measurement serves as the best proxy for actual 3D crystal volumes. Assumptions are often made for this purpose, such as a constant growth rate in a kinetically-driven environment, consistency and euhedrality in crystal forms, and the presence of a random fabric. Because plagioclase can acquire multiple habits reflecting magma geochemistry (Cheng et al., 2017), large crystal counts should be stereologically addressed separately from groundmass occurrences. Since groundmass plagioclase is often elongate in thin section, and given the above assumptions, a 3D tabular form is suggested. Phenocrysts often have smaller length-to-width ratios in cut section, suggesting they are blockier in form given a truly random fabric. In any case, equant forms are not expected with plagioclase and so length measurements using diameters of best-fit circles or the square root of an equal-area square are not considered here. TIMA software does provide crystal lengths based on the diameter of a best-fit circle, but plagioclase is not an isometric phase and so diameter measurements are not directly suitable. CSDSlice uses the best-fit ellipse approach and is a much-employed method for addressing aspect-ratio effects in 2D cut sections (Brugger and Hammer, 2010; Neave et al., 2013, 2017), and so it is used here in conjunction with CSDCorrections. The long axis of a best-fit ellipse serves as a strong proxy for actual size (L) (Higgins, 2006) given a random fabric and the assumption of non-cubic shapes.

For our investigation of plagioclase crystal clusters using EBSD, a freely available MATLAB tool box called MTEXT (Mainprice et al., 2015) was used to create a script to process raw diffraction files originating from Oxford Channel 5 acquisition software. The script provides a qualitative fabric descriptor called an M-index which is thoroughly discussed in Skemer et al. (2005). An M-index is based on the distribution of misorientation angles and requires ~150 orientation measurements to produce a meaningful result, on a scale of 0 to 1, where 0 indicates no preferred orientation and 1 indicates a strong preferred orientation.

### 2.7.2 Manual tracing

Plagioclase crystals from photomicrographs were traced using Adobe Photoshop. A 150 μm size threshold was used to define phenocrysts but smaller crystals were traced to minimize the chance of overlooking crystals that fit the size requirements. Tracings were infilled in Adobe Photoshop so that thresholding in ImageJ would be possible.

### 2.7.3 BSE imaging

For thin sections L-4B and V4 where CSDs are groundmass-dominated, a total of six BSE images were acquired using a TESCAN MIRA3 LMH Schottky field emission-scanning electron microscope (FE-SEM) equipped with a single-crystal YAG BSE detector and a Bruker XFlash 6/30 silicon drift detector at the Colorado School of Mines. Scan conditions included an accelerating voltage of 15kv and a working distance of 10mm. The BSE images were ~300 μm x 250 μm and only plagioclase crystal lengths ≤ 150 μm and ≥ 1 μm were considered for CSD plots. The BSE images were used to perform a relative-fabric analysis. This new fabric test consisted of comparing CSDs between three BSE images from L-4B and three BSE images from V4 (Fig. 2.7). If the general fabric was similar across samples, cut sections through crystals from the two orthogonal sets, regardless of crystal contiguity, should theoretically produce similar CSDs.

Vesicle borders were avoided to minimize bubble-induced orientation that can occur with vesicle interaction. This groundmass fabric test involved several assumptions across BSE images: late-stage crystallization must occur as a single, non-episodic process on the scale of the thin section area; images reflect crystals of similar aspect ratios and size populations (CSD Slice is therefore not required (i.e. no stereological correction was performed)); spatial distribution of other phases, and therefore ImageJ thresholding artifacts, are similar. To maintain consistency between image-derived length measurements in ImageJ, thresholding reflected a compromise where maximum values preserved plagioclase boundaries (excessive threshold values created artificially large plagioclase particles), but reduced fractures and speckling caused by the grayscale of clinopyroxene cores.

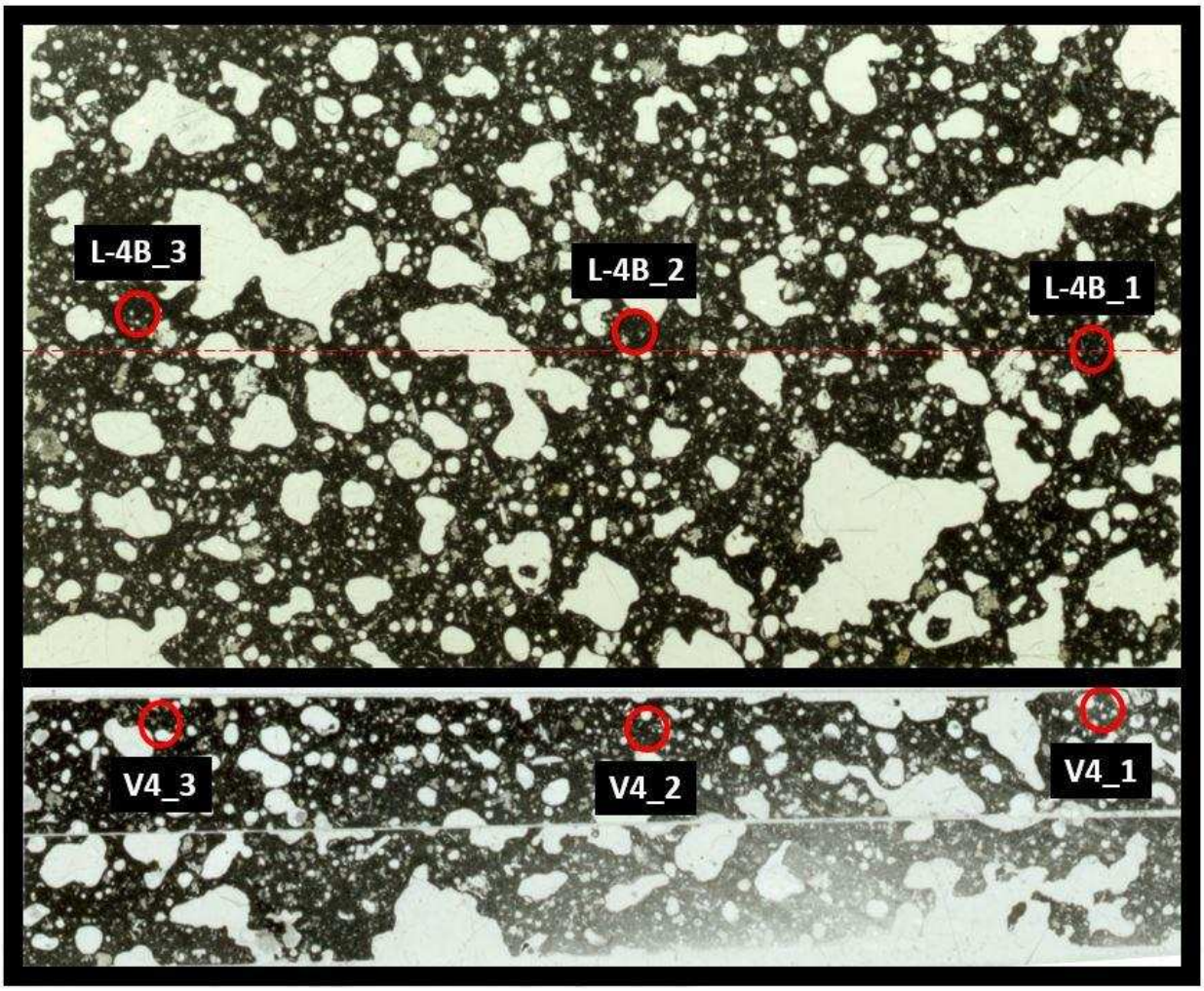


Fig. 2.7. The red circles represent the six regions from which BSE images were produced. L-4B (upper image, carbon coated) and orthogonally oriented V4 (lower image, pre-carbon coated) were sampled for groundmass crystal lengths only (crystal lengths under 150 μm). Since V4 is produced from a mid-sectional cut along the elongated direction of the billet from L-4B, more proximal areas to regions chosen in L-4B are closer to the upper and lower regions of the elongated direction as shown in V4. Field of view is ~30mm across.

The maximum upper value was determined visually from ImageJ threshold peaks, at the point where the right tail (upper portion of the threshold curve) for the plagioclase peak shows the largest change in slope. Only particles with major axes ≤ 150μm but ≥ 1μm were considered. Results for both edge-particle exclusion and inclusion were examined and void space was accounted for. The plagioclase groundmass aspect ratio was set to 1:4:8 and 1:8:8 in CSDCorrections, reflecting the minimum length-to-width ratio

of >4 reported by Neave et al., (2017) (2D longest length measurements more closely reflect actual 3D intermediate-values than actual 3D long-values, given S: I: L). BSE images show that discrete groundmass plagioclase crystals are often contiguous, producing a singly complex, large connected particle that is not acknowledged by ImageJ.

### 2.7.4 TESCAN TIMA automated imaging

Automated analysis was performed at the Colorado School of Mines' Automated Mineralogy Laboratory using a TESCAN-VEGA 3 Model LMU VP-SEM with four PulseTor 30 $mm^2$ EDX detectors, a YAG scintillator BSE detector, and TIMA software version 1.5.26. Analysis was initiated using the control program TIMA3. Scan conditions for EDX analysis included an accelerating voltage of 25 keV and a beam intensity of 14.

TIMA phase maps of plagioclase were binned by anorthite content: $An_0 - An_{50,}$ $An_{50} - An_{64,}$ $An_{64} - An_{89,}$ and $An_{89} - An_{100.}$ This logic follows the Passmore et al. (2012) definition of a plagioclase groundmass minimum of $An_{51}$ and a maximum of $An_{64}$ and plagioclase phenocryst cores up to $An_{89}$. Anorthite contents are similar to the reported values in Guilbaud et al. (2007), with primitive plagioclase cores >$An_{70}$ and groundmass similar to phenocryst rims of $An_{49-70}$ (lava, not tephra). Neave et al. (2017) also utilize $An_{64}$ as a separator to distinguish between groundmass and phenocryst of Laki basalts. All our samples show less than 40% vesicles (L-4B ~24% and L-E ~16%), as determined by ImageJ thresholding.

Plagioclase was defined for automated analysis first by establishing BSE brightness values from point analysis of plagioclase in the samples. Brightness values ranged from 19.8 to 22.5. When each scan point falls within the brightness range above, an EDX X-ray spectrum is acquired. EDX spectra for each pixel was produced from 1000 X-ray counts at a spatial resolution of 2 µm. The EDX spectra are compared against a look-up table which permits a mineral assignment on a per-pixel basis. Scan times were ~6 hours for L-4B and ~17 hours for L-E. Definitions were created for the degree of anorthite content shown in the bins listed above so that spectra produced images reflecting the binned anorthite values. Spectra acquisition occurs over multiple smaller fields and TIMA software automatically stitches

the fields together to produce the larger image. The final result is a digital image of plagioclase crystals superimposed onto a corresponding BSE image.

Two types of TIMA plagioclase phase images were used to obtain crystal length measurements. The image types are produced from a single scan but can be rendered differently. Type 1 images are panoramic phase images that represent the stitched-together fields of plagioclase+BSE information. Type 2 images are isolated-particle images where coherent plagioclase crystals are digitally isolated from the original full-scan, post-stitched area (i.e. from panoramas). The particles (or crystals) can be ordered by size. In the case of isolated-particles images (type 2), each coherent particle can be further reduced in size by digital clipping, or segmenting (Fig. 2.8). To distinguish between the two types of TIMA images, type 1 will be referred to as "panoramic" and type 2 as "isolated-particle". For both types of images, edge-bordering particles were manually deleted. Edge-bordering particles are those that appear at the borders of the panorama image and were partially cut off due to falling outside of the scan area. Particles that suggested fracturing and possible loss of area were included in size counts only when at least ~80% of the perceived original size was present.

TIMA determines size using the diameter of an equal-area circle rather than a best-fit ellipse. The former method for determining crystal lengths is only suitable for isometric phases and is not suitable for low symmetry phases or those that display large differences in aspect ratios. When crystal shapes cannot be determined directly and confidently from 2D cut sections (which is almost always the case), using diameters of equal-area circles can be misleading and produce erroneous CSD distributions. Most methods of defining linear 2D measurements produce similar values for equant shapes but values begin to diverge with decreased symmetry (Higgins, 2006). For TIMA-defined lengths (i.e. the diameter of a best-fit circle), ~80 μm approximated a longest-length of 150 μm for L-4B. For L-E, a TIMA diameter of ~90 μm closely approximately a maximum length of 150 μm. Maximum length is the greatest distance between the two farthest points on a particle outline.

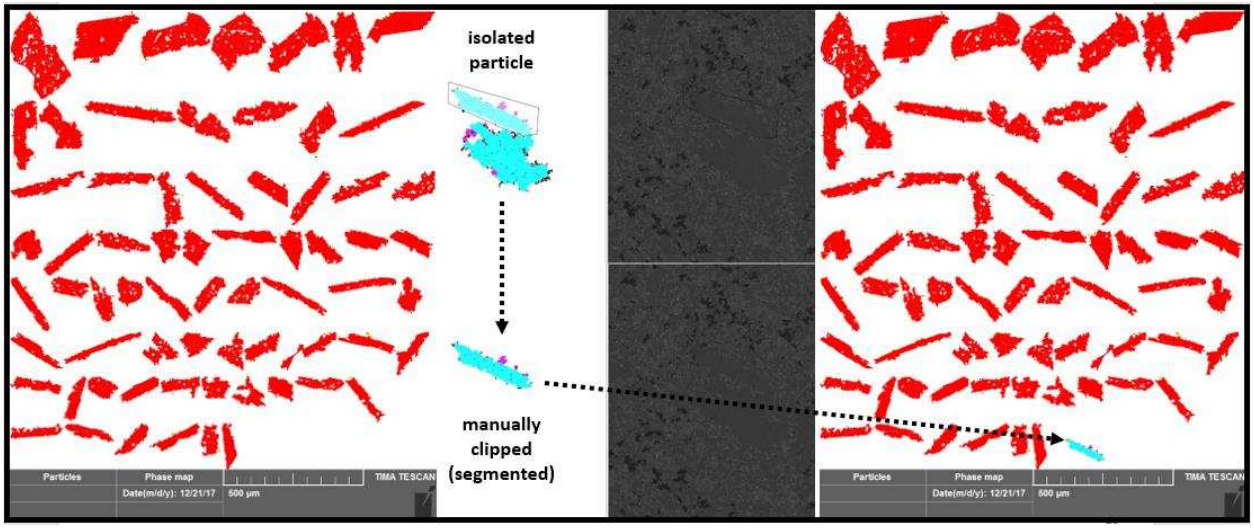


Fig. 2.8. An example of segmenting, or digitally clipping, a larger plagioclase cluster into smaller components. A particle from an isolated-particle image (left) is selected (center-left, in blue) and manually separated into smaller particles. The goal is to create discrete crystals for length measurements in ImageJ. The particle is then automatically placed back into the isolated-particle image (right) by size rank according to the diameter of a best-fit circle.

### 2.7.5 Electron backscatter diffraction imaging

Orientation analysis for a single glomerocryst in sample L-E was completed on a FEI QUANTA FEG 450 field emission scanning electron microscope equipped with an Oxford Instruments X-Max 80 $mm^2$ EBSD detector and a Centaurus BSE detector at the University of Wyoming's Material Characterization Laboratory. The following scan conditions were used: a sample tilt angle of 70 degrees, an accelerating voltage of 20 kV, a spot size of 5, a step size of 2.5 µm and a working distance of 30 mm. Oxford Instruments HKL Channel 5 software was used for both acquisition and noise reduction. Initial indexing occurred at a Hough transform resolution of 60 with subsequent re-indexings of 70 and 55. Noise reduction was performed after the three re-indexings, following Prior et al. (1999). A mean angular deviation (MAD) of ≥1° was used to define grain boundaries. MTEX was used to produce orientation data and crystal boundary maps from Channel 5 files. A MTEX script was created to account for the 12 plagioclase twin laws as described by Xu et al. (2016) for the purpose of defining discrete crystals.

## 2.8 Results

### 2.8.1 Relative-fabric test for groundmass orientation

Backscatter electron images of L-4B and V4 groundmass (Figs. 2.9 and 2.10) were converted to 8-bit grayscale and processed through ImageJ to obtain the major and minor axes of best-fit ellipses. Best-fit aspect ratios were not obtained as kinetic information such as nucleation rate and residence times were not of concern. Here, the general shape of CSD curves was examined to determine if there was consistency in plagioclase orientation across all areas sampled. Porosity per sample area was factored into CSDs as well as two aspect ratios that each considered edge-bordering (E) and non edge-bordering (NE) crystals. Figures 2.10 through 2.12 summarize findings.

L-4B sampled areas show strong similarities in CSD curvature at L values < ~25 μm and < ~15 μm for both E and NE types of analyses at aspect ratios of 1:4:8 and 1:8:8, respectively (Fig. 2.11), suggesting that crystal size distributions are similar among the three spatially separated regions within sample L-4B. E-style (edge-bordering) analyses produce larger L values due to the effects of increased contiguity. Divergence of CSDs occur toward the larger L values as smaller particles are likely contributing to the contiguity affect and are therefore not counted in smaller L-bins. Sampled regions within V4 display similar CSDs but divergence occurs much earlier at ~L=10 for 1:4:8 and ~L=5 for 1:8:8.

The BSE image for V4 1 (Fig. 2.10) initially suggests a coarser population but the average particle size is C=3.37 μm. Average particle sizes for V4 2 and V4 3 are 3.43 and 3.36 μm, respectively, indicating ~2% maximum difference. Despite the potential artifacts of thresholding BSE images in ImageJ, CSD curves are remarkably similar in shape for a given aspect ratio, suggesting consistency in fabric within L-4B and L-E. Similarity in curve shape does not, however, suggest that no fabric actually exists. Although growth rate and residence time were not of concern here, the effects of particle shape choice on kinetic information is apparent.

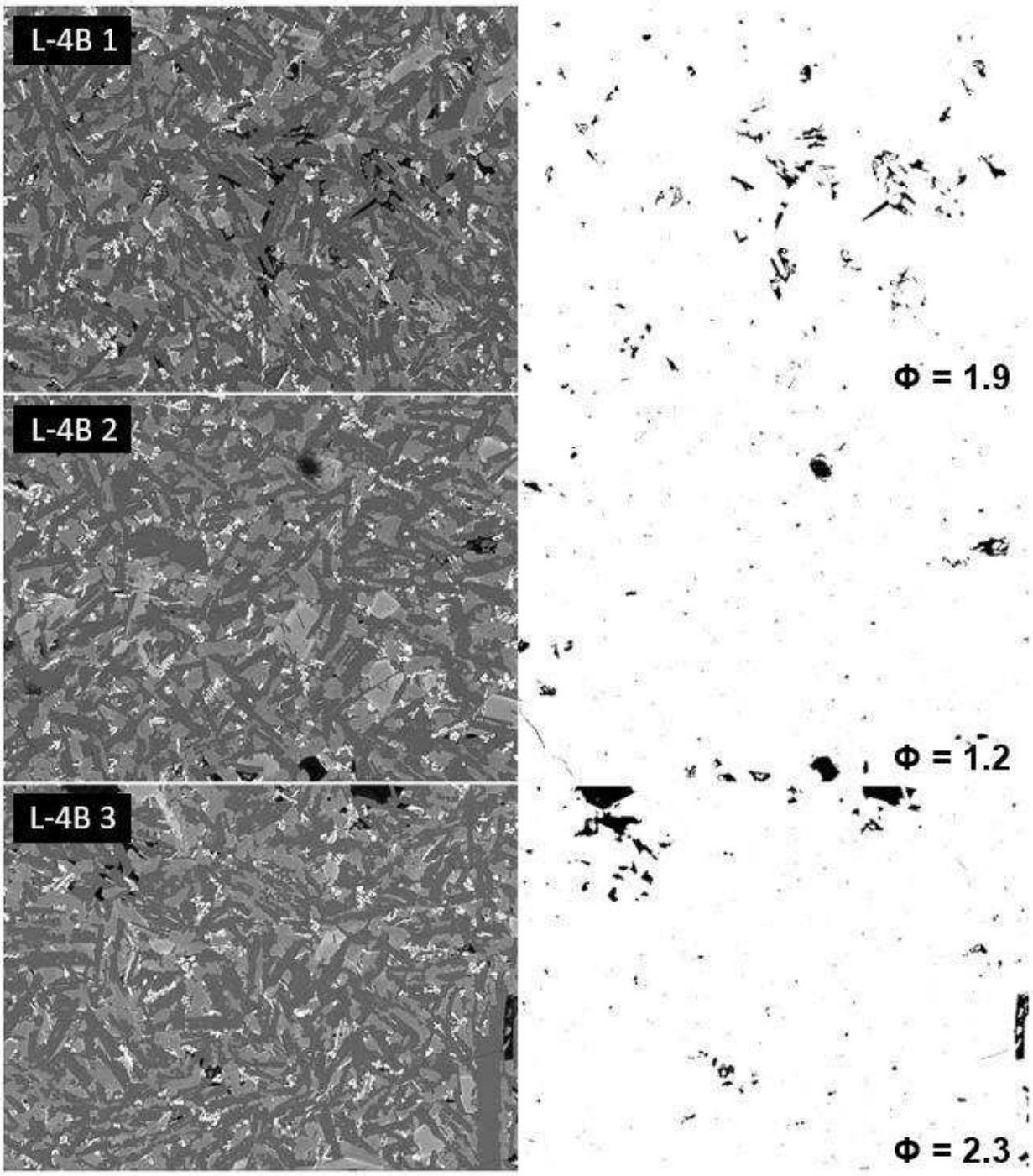


Fig. 2.9. ~300 µm x ~250 µm BSE images from L-4B (Group A). Figure 2.7 shows the location of the sampled groundmass areas. Feldspars appear dark gray. Microlite texture appears random with minimal porosity (Φ) regions chosen. Areas near vesicles were avoided. Lighter phases are olivine, clinopyroxene and opaques.

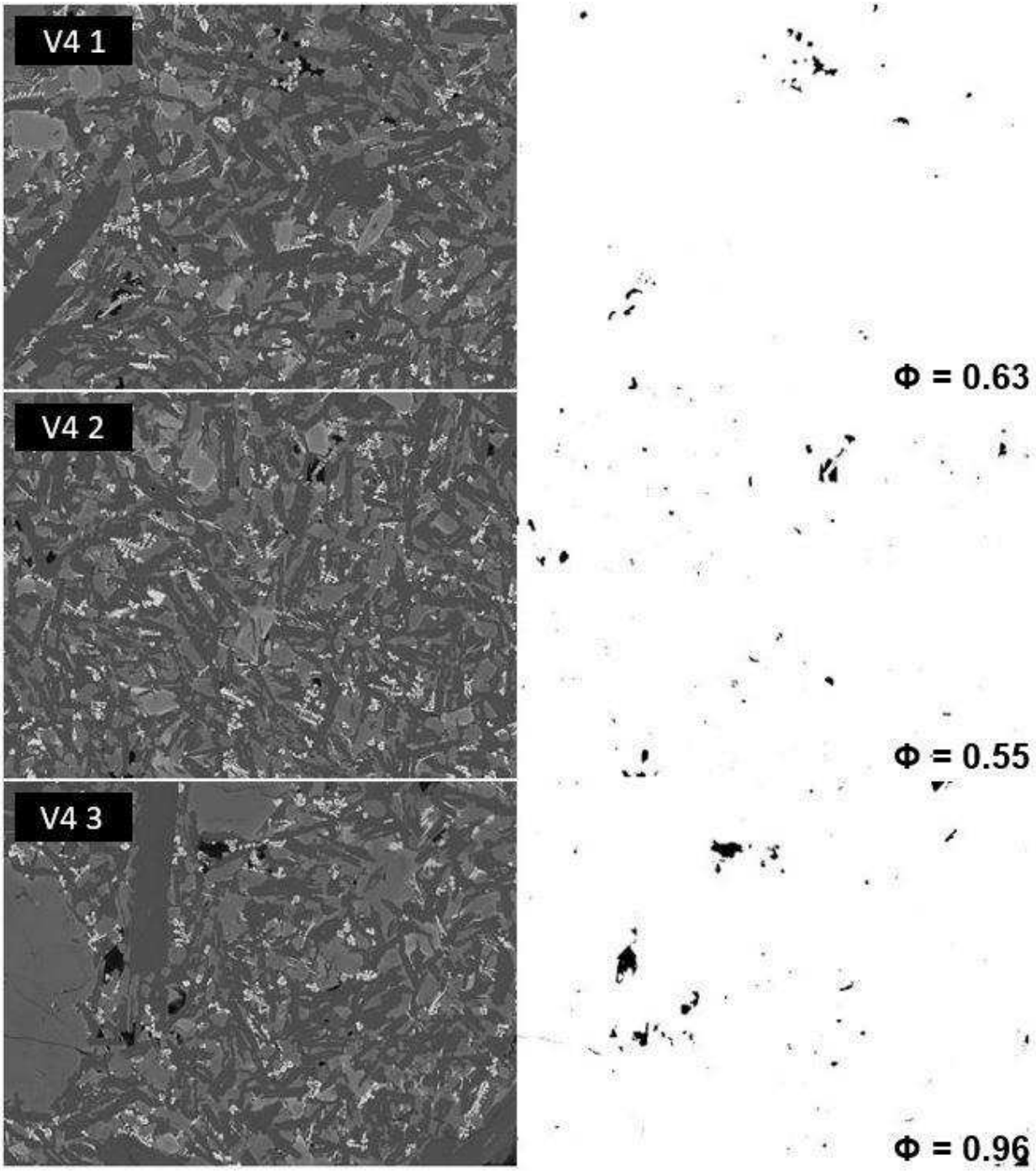


Fig. 2.10. ~300 µm x ~250 µm BSE images from V4 (Group B). The three regions are spatially close to group A groundmass areas sampled in Figure 2.9 but represent a perpendicular cut section. Elongated dark gray shapes are plagioclase, similar to that in Figure 2.9. Only plagioclase ≤150 µm based on the long axis measurement were considered here.

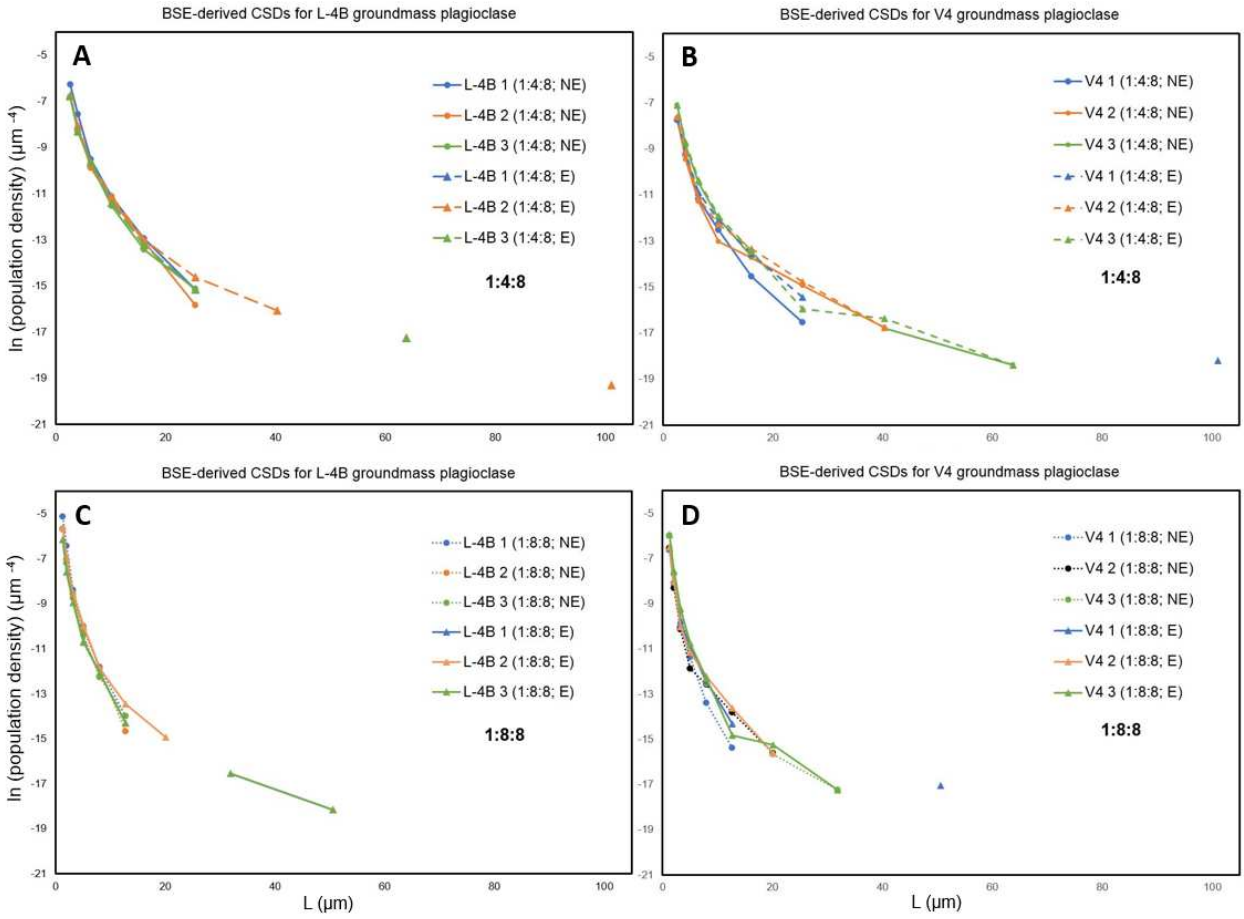


Fig. 2.11. Groundmass-only CSD curves generated from BSE images for orthogonal sets of proximal pairs: L-4B 1 is orthogonal and proximal to V4 1. L-4B 2 to V4 2, and L-4B 3 to V4 3. Two aspect ratios representing two slightly different shapes (1:4:8 = prismatic = Figures A and B; 1:8:8 = tabular = Figures C and D) still produce strong correlations within samples NE (non-edge) represents BSE analyses that ignore particles that border image edges. E represents BSE analyses where edge-bordering particles were included. Figures A and C (left column) show strong correlations in CSD curve patterns, suggesting similarity in orientation patterns and in contiguity styles of groundmass plagioclase. Divergence occurs at the larger sizes. Floating points at the largest sizes are due to bin counts < 3. Five bins per decade were used.

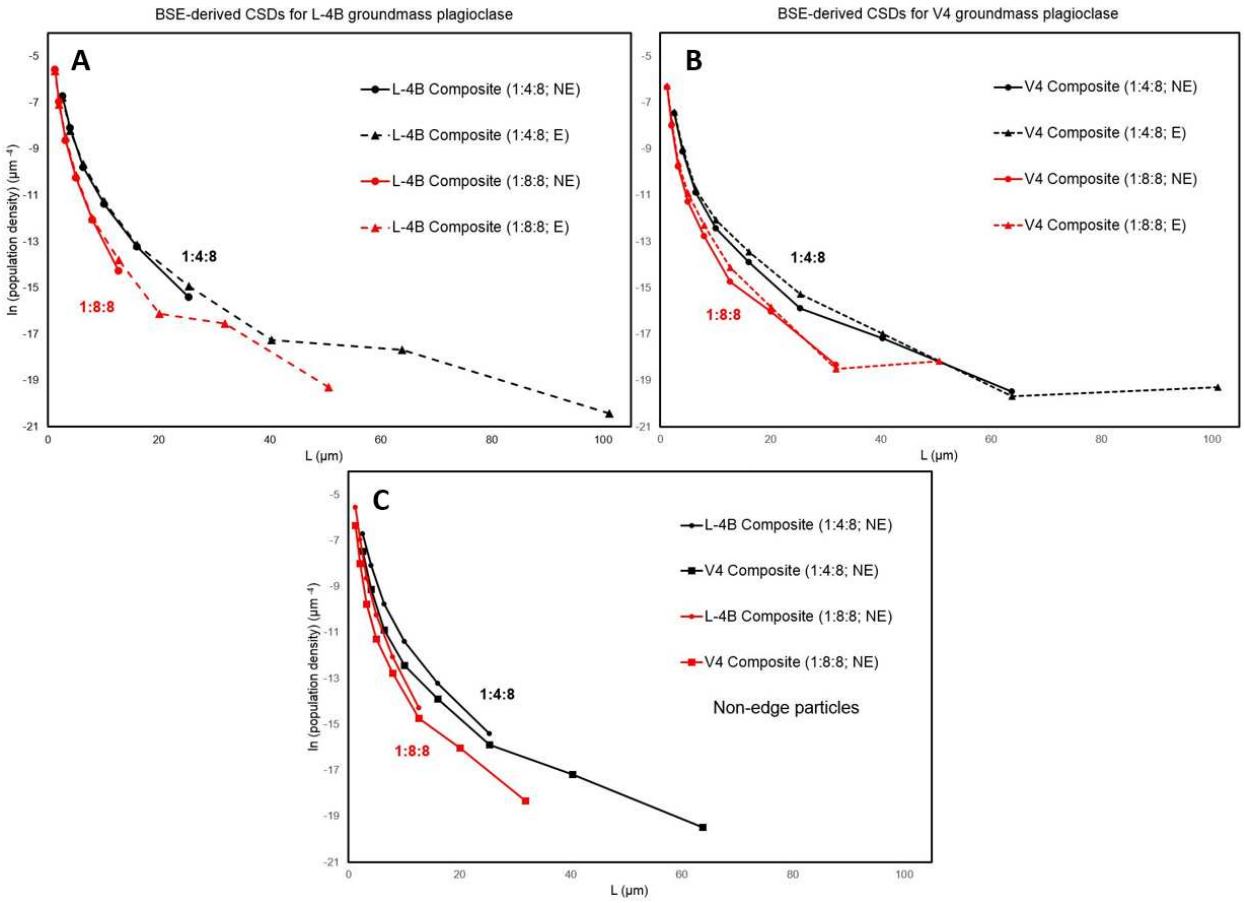


Fig. 2.12. Comparisons between L-4B and V4 groundmass plagioclase, emphasizing aspect ratio effects from non edge-bordering and edge-bordering BSE image processing in ImageJ. Figures A and B compare the effects of tabular (1:8:8) and prismatic (1:4:8) shapes. Including edge-bordering particles creates flatter curves at the larger L values (Figures A and B triangular points). Irregularities are likely due to small sample sizes for larger L values. However, trends are similar within each aspect ratio. Edge-bordering curves always have their smallest L values below that of non edge-bordering curves on the y-axis. Figure C shows that L-4B produces greater nucleation population densities than V4. Curve shapes are still similar and differences between 1:4:8 and 1:8:8 curves are strictly due to aspect ratio choice.

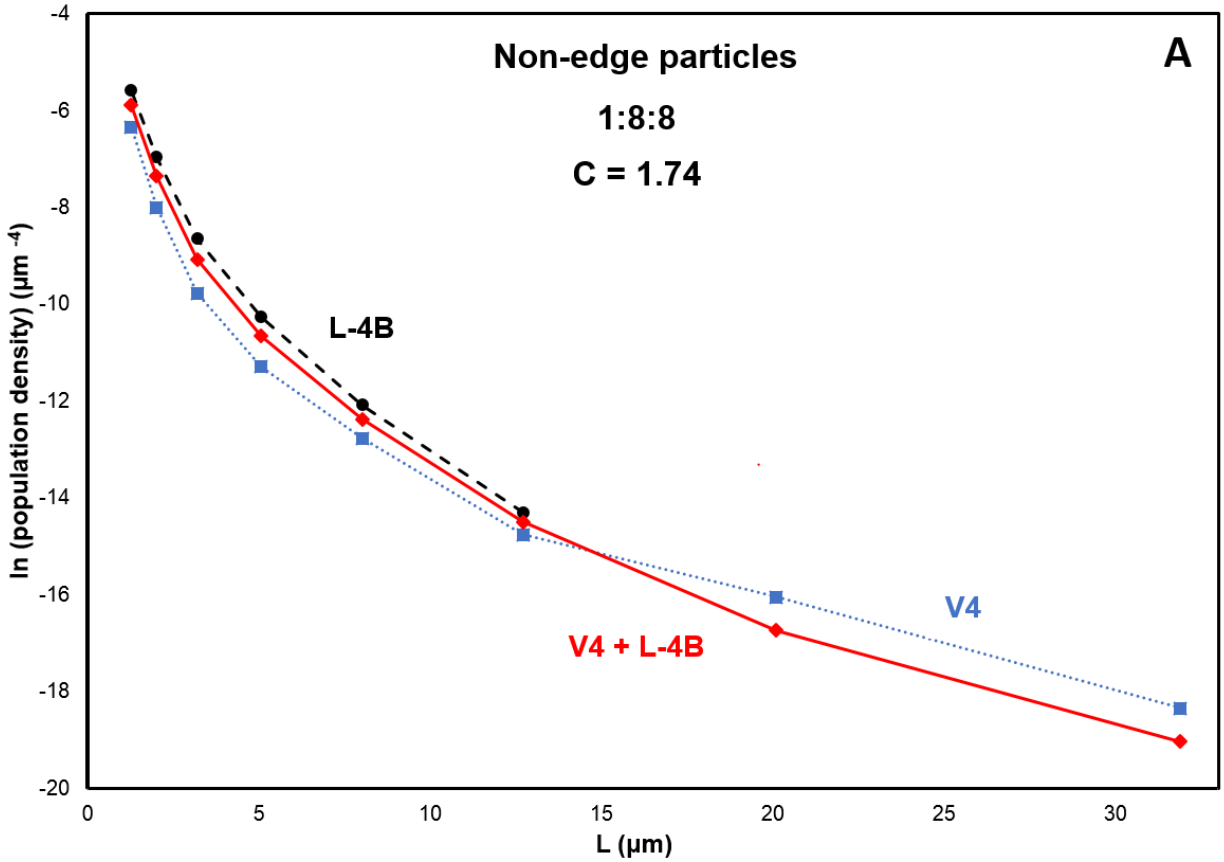


Fig. 2.13. Combined results for L-4B and V4 (composite) for a single aspect ratio (1:8:8) reflecting a tabular form with non-edge analysis in ImageJ. C represents the average particle size in µm. Random orientation of tabular plagioclase microlites is assumed for analysis. The V4+L-4B curve (red curve) shows the combined results in CSDCorrections using the three sampled areas for L-4B and the three sampled areas for V4.

Most image processing that focuses on particle size measurements removes edge-bordering particles from size counts, which is reasonable as edge particles do not represent full apparent lengths in 2D cut sections. Figure 2.12 C and Figure 2.13 show the results of E and NE-style analyses. Figure 2.12 suggests that variations in CSDs that are more strongly affected by choice of aspect ratio rather than edge effects, where nucleation densities approach similar values for a single aspect ratio. Figure 2.13 shows that combining the six sampled groundmass regions from L-4B and V4 produces a single CSD curve that suggests a common pattern of an increasingly fast-cooling lava where groundmass growth rates increase over time. This result is surprising given the high degree of crystal contiguity that was expected to mask

this common pattern seen in erupting lavas. This finding suggests that despite the contiguous groundmass, the general crystallization style may still be preserved in the CSD.

### 2.8.2 CSDs from TIMA and manually-traced images

Large scans of plagioclase of L-4B and L-E (Table 2.3) were initially acquired over 133.406 and 170.208 $mm^2$, respectively, with over 400000 plagioclase particles defined for each sample. These areas were cropped for ImageJ analysis, resulting in 92.57 $mm^2$ (L-4B, 8901 x 2600 pixels) and 163.94 $mm^2$ (L-E, 3600 x 11387 pixels). Full thin section scans were not performed as acquisition times for L-4B and L-E were already 6+ hours and 17+ hours, respectively. Zero-plagioclase pixels occurred in some of the largest phenocrysts and rarely in the groundmass. L-4B displays three major occurrences of regions of non-plagioclase pixels (Fig. 2.14), and this issue was addressed before image processing with ImageJ by manually assigning the missing pixels the same greyscale color as the plagioclase present. L-E was highly porphyritic and contained up to 50 variably affected phenocrysts which were addressed in a similar manner to L-4B. The remaining phenocrysts were either not affected by non-assigned pixels or minimally affected to the extent that relict small-crystal populations were infrequently created (Fig. 2.15).

Table 2.3. TIMA results of isolated-particle image editing from multi-field (panorama) phase maps. Column C includes the removal of any particles consisting of fewer than four pixels, resulted from digital clipping. Column B includes mis-stitched and edge-bordering particles. Columns A, B and C are exclusive of each other. Min and Max size columns are derived from TIMA's default size bins and represent bins defined by the diameter of an equal-area circle.

| Multi-field scan characteristics (panorama) | | | | | | | |
|---|---|---|---|---|---|---|---|
| Group A | Min size bin (µm) | Max size bin (µm) | No. of fields | **A** No. of particles created | **B** No. of particles deleted | **C** No. of particles created and then deleted | Total number of particles after **A, B, C** |
| L-4B | [2.2, 2.6) | [185, 217) | 56 | 149 | 33 | 17 | 425508 |
| L-E | | [298, 349) | 114 | 4163 | 661 | 531 | 419378 |

.

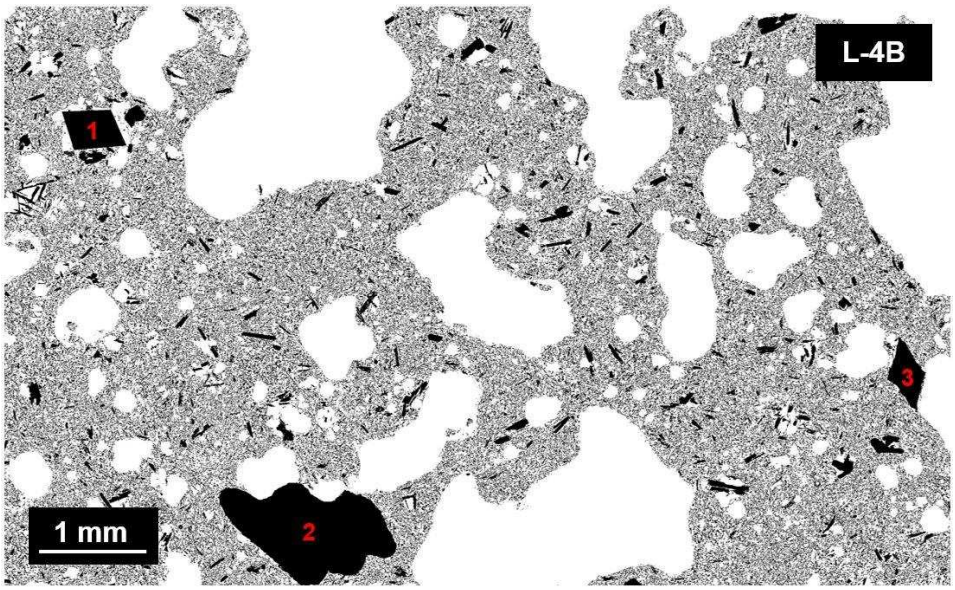


Fig. 2.14. A thresholded image of part of the L-4B panorama for all plagioclase species. The three largest phenocrysts, numbered above, have been filled in with black for improved ImageJ analysis. The phenocrysts showed significant amounts of zero-plagioclase points and were corroborated with photomicrographs. Zero-points were not due to internal sieving.

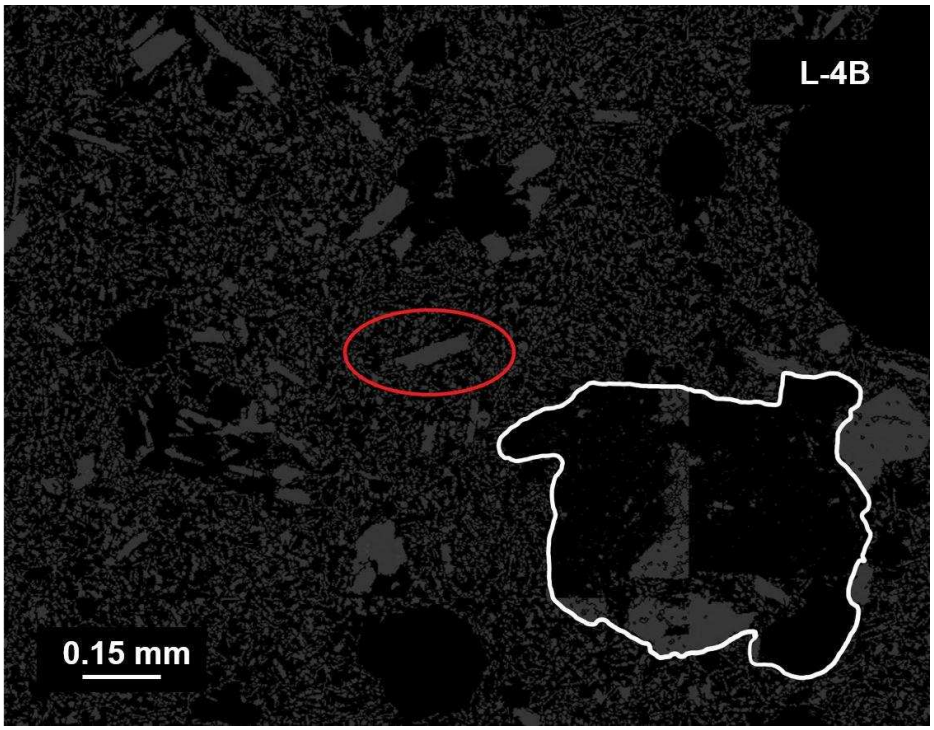


Fig. 2.15. An example of the original TIMA grayscale all-plagioclase image. The area outlined in white is a region of vesicle and plagioclase. This region was checked against the thin section in XPL to approximate the original plagioclase border and size (phenocryst 1, Fig. 2.14). The red circle represents the smaller phenocrysts that were not affected during the scan.

The minimum phenocryst size for both TIMA panoramas and isolated-particle images was determined by visual inspection. Where the size of the smallest, coherent particles was equivalent to ~150 μm (longest-length method,) the diameter of the best-fit circle provided by TIMA software was noted. The size was ~80 μm for L-4B and ~90 μm for L-E. Long axes of best-fit ellipses were then calculated by ImageJ. Phenocrysts in cross-polarized light (XPL) photomicrograph equivalents of TIMA panoramas were traced, and the long axes of best-fit ellipses were determined with ImageJ.

CSDSlice was used to obtain best-fit aspect ratios of 1.0: 3.0: 6.0 ($R^2$ = 0.6353) and 1.0: 2.5: 5.5 ($R^2$ = 0.8486) for L-4B phenocrysts using isolated-particle and panorama images, respectively. The L-4B isolated-particle image did not provide the minimum number of phenocrysts for reliable shape determination (67 phenocrysts), and this low crystal count likely affected the best-fit aspect ratio. The panorama image provided 422 phenocryst long-axis measurements ≥ 91.10 μm. Further removal of smaller populations of phenocrysts in an attempt to improve the correlation strength of an aspect ratio had the reverse effect, as $R^2$ values were reduced.

L-E aspect ratios for isolated-particle and panorama images were 1:0: 2.1: 5.5 ($R^2$ = 0.8153) and 1.0: 2.5: 5.0 ($R^2$ = 0.8156), respectively. Since L-E is texturally seriate, the populations for both isolated-particle (732 phenocrysts) and panorama (3211 phenocrysts) images were examined with the largest 50% and 25% of population sizes (long axes) to determine if there was an improvement in a best-fit shape. $R^2$ values increased slightly to 0.8206 and 0.8203 at 50% and 25% for the panorama and decreased slightly for isolated-particle images, to 0.8153 and 0.8110. All adjustments to phenocryst populations as described above resulted in negligible changes to aspect ratios.

Photomicrograph phenocryst tracings for L-4B and L-E were performed over similar areas compared to TIMA scans. Recognizable plagioclase crystals were traced even when groundmass sizes were reached for L-E; due to the seriate nature, a groundmass size categorization does not guarantee a separate and distinct aspect ratio. In this case, the minimum longest-lengths measured for plagioclase were ~45 μm for L-E and ~70 μm for L-4B. Tracings were processed with ImageJ and converted to

dimensions of best-fit ellipses. For L-4B, since groundmass and phenocrysts appear strongly bimodal in XPL, 291 distinct phenocrysts were traced. Where glomerocrysts existed, individual plagioclase crystals were traced to account for as many discrete crystal occurrences as possible to avoid skewing of aspect ratios. CSDSlice determined a best-fit aspect ratio of 1.0: 3.6: 7.0 for L-4B with $R^2 = 0.8897$. For L-E, the seriate texture required individual treatments of different size populations for their associated aspect ratios. When all tracings resulting in long-axes measurements of >10 μm were analyzed (1497 crystals), a best-fit aspect ratio of 1.0: 3.2: 8.0 with $R^2 = 0.8092$ resulted. The largest 75% and 50% long-axes populations were also examined and resulted in aspect ratios of 1.0: 3.6: 7.0 ($R^2 = 0.8360$) and 1.0: 5.0: 9.0 ($R^2 = 0.8552$), respectively. The largest 50% of the population equated to 749 crystals with a minimum size of 147.9 μm.

Crystal size distributions comparing isolated-particle, panorama, and XPL tracings are summarized in Figure 2.16. The resulting kinetic characteristics are in Table 2.4. For L-4B, each method's CSD accounted for 35% porosity and the aspect ratio determined by CSDSlice. Therefore, three different aspect ratios were used as determined by each method. Another set of CSDs were produced using crystal lengths from each of the three methods but with the aspect ratio determined from XPL tracing only (Figs. 2.16A and B, new aspect ratio).

Discontinuities in CSD curves occurred at the largest L bins due to an insufficient sample size for those bins. For L-4B (Fig. 2.16) XPL tracings provided the most consistent and continuous data for all size populations ≥ 150 μm. Isolated-particle images did not provide adequate data points at the coarsest sizes, likely due to fractured phenocrysts which ImageJ interpreted as multiple smaller particles. Panorama images provided similar small-L bin behavior but like isolated-particle images, caused CSD discontinuities at the coarsest bins due to phenocryst fracturing. However, the downturn at the finest fractions is preserved by all methods, and so downturns suggest that more sampling needed to occur below the 150 μm threshold. The use of the photomicrograph-derived aspect ratio with isolated-particle and panorama crystal lengths caused a slight shift of the CSD to lower L-values. Depending on which

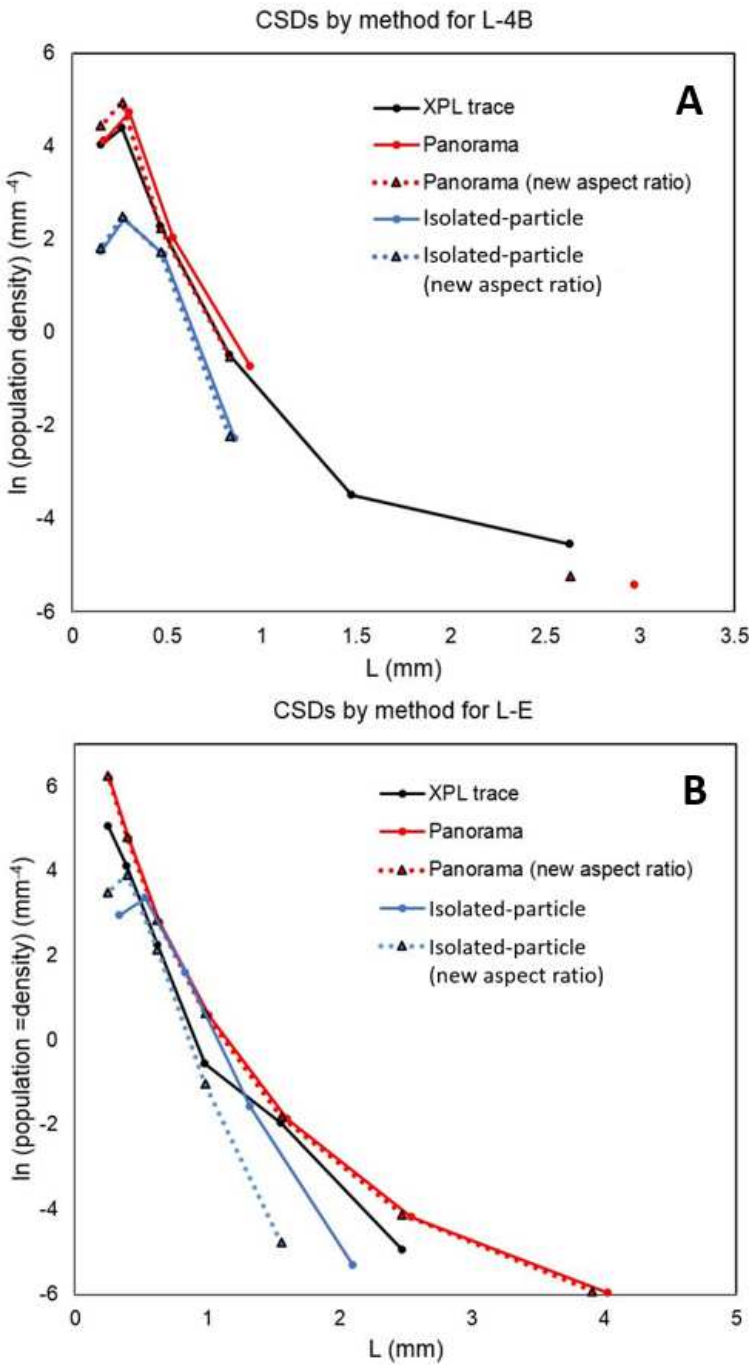


Fig. 2.16. A comparison of CSDs from L-4B and L-E. Length measurements for plagioclase phenocrysts were derived from manual tracings of photomicrographs and from panoramas and isolated-particle images. Four bins per decade were used for Figure A and 5 bins per decade for Figure B. *New aspect ratio* represents the use of the photomicrograph aspect ratio. The turndown at the smallest L-values are likely due to an insufficient crystal count for the smallest L-value bins. Figure B shows an insufficient number of the largest phenocrysts such that floating points result. Panorama-sourced measurements consistently create the largest nucleation population densities while isolated-particle images produce the lowest.

Table 2.4. Kinetic characteristics derived from the isolated-particle phase images, panoramas, and photomicrographs used to determine CSDs. C = average crystal size, J = nucleation rate and $n^0$ = nucleation density. Table values were determined as follows, based on an assumed crystal growth rate of $G = 10^{-10}$ mm/s: C was calculated using regression slopes from CSDCorrections (m), where C = -1/m; $n^0$ was determined from directly from CSD corrections; J = exp ($\ln(n^0)$) *G; and $\tau$ is defined as C/G/($3.154*10^7$). S: I: L = short: intermediate: long.

**CSD characteristics by method (phenocryst size populations)**

| Method | Slope | | ln ($n^0$) | | C (mm) | | mean $\tau$ (days) | | J (mm-3 $s^{-1}$) | | Aspect ratio (S: I: L) | |
|---|---|---|---|---|---|---|---|---|---|---|---|---|
| | L-4B | L-E | L-4B | L-E | L-4B | L-E | L-4B | L-E | L-4B | L-E | L-4B | L-E |
| **Isolated particle** | -5.01 | -4.91 | 3.90 | 5.75 | 0.345 | 0.538 | 39896 | 62269 | 4.94E-09 | 3.14E-08 | 1.0: 3.0: 6.0 | 1.0: 2.1: 5.5 |
| **Panorama** | -8.58 | -6.51 | 7.04 | 7.62 | 0.296 | 0.324 | 34213 | 37500 | 1.14E-07 | 2.04E-07 | 1.0: 2.5: 5.5 | 1.0: 2.5: 5.0 |
| **Manual tracing** | -5.62 | -6.26 | 5.51 | 6.50 | 0.274 | 0.339 | 31713 | 39236 | 2.47E-08 | 6.65E-08 | 1.0: 3.6: 7.0 | 1.0: 3.6: 7.0 |

portion of the curve one bases a regression line to determine nucleation density, this curve shift may have the effect of slightly reducing the nucleation density, but by less than an order of magnitude.

For L-E, CSD curve continuity was maintained due to the large number of measurements obtained. The downturn over small L-values for CSDs from isolated-particle images was likely an artifact of equating the TIMA-defined size of ~80 μm to a 150 μm longest-length measurement. Panorama images provided a similar shape profile to that created from XPL tracing, but the largest particle measurements reflect inflated values due to particle contiguity within plagioclase-dominant glomerocrysts. The panorama-derived curve is smooth compared to the XPL-derived curve and suggests that although the former method produced an artificially large number of larger particles, the method in general detected more particles than manual tracing provided. As with L-4B, only minor horizontal shifts in CSDs occurred when the XPL-derived aspect ratio was used.

### 2.8.3 CSDs using TIMA images for groundmass sizes

High resolution scans can provide valuable information on groundmass size-distributions. TIMA-based panorama phase maps have the potential to convey size information for particles that are too small to efficiently resolve by manual means in photomicrographs. Assuming that manual tracing provides the most reliable size information for phenocrysts that can be confidently identified, TIMA can then be used to supplement sample sizes at the groundmass fraction. Here we combine the length measurements from XPL tracing of phenocrysts for L-E (L-4B was not considered due to an insufficient phenocryst population count) with panorama images for groundmass crystal sizes.

CSD Slice can only process measurements for 65528 particles at a time. 733 of those particles originated from phenocrysts from XPL tracing. The remaining 64795 particles were groundmass particles with major axes as small as 5.58 μm. Given a scan resolution of 2 μm, we left the lower size range at 5.58 μm. CSDSlice determined a best-fit aspect ratio of 1:0: 2.5: 5.0 with $R^2 = 0.8354$. CSDCorrections can only process 20001 entries at a time for a single CSD. Therefore, only 19268 groundmass measurements were used with the smallest major axes measurements at 14.38 μm. Results from combining XPL-derived

phenocrysts and TIMA-derived groundmass are shown in Figure 2.16. This combined-measurement method produced a slightly curved CSD (sub log-linear) that invokes multiple interpretations. If it is assumed that measurements have incurred only small errors, then a curved CSD may suggest some history of a non-steady state environment without having reached the extremes of significant signs of textural coarsening (i.e. equilibrium growth). The seriate nature of the plagioclase size distribution, the dominantly euhedral shapes of plagioclase, along with chemical zonation, already suggest a dominantly steady-state system with changes in carrier melt geochemical characteristics.

The CSD curve provides information in addition to what can already be gleaned from a photomicrograph as a first-order approximation. The steeper slope at the smaller size ranges may suggest increased nucleation and therefore a sudden decrease in temperature (increased undercooling). The slope increase may be indicative of a sudden surge from the magma chamber. Another unexplored likelihood is that the presence of swallowtail microlites contribute to the small-size populations when cut sections intersect tail-ends. Given that rare phenocrysts showed strong internal sieving (Fig. 2.5 D), magma mixing is also possible.

If the steep slope in the CSD curve is due to a method-induced bias, then the CSD curve may be of limited value in determining nucleation density. However, an initial inspection of the microlight population in thresholded images suggests that when holes are included for image analysis, microlite border integrity is preserved, thus reducing bias in panoramic measurements of microlites. This degree of microlite measurement accuracy cannot be accomplished using microphotographs. Figure 2.16 produces a nucleation density (y-intercept) of 10.96 based on a regression slope of -14.1. These values are significantly larger than those indicated by the other methods in Table 2.4, suggesting that TIMA-generated images may provide upper boundaries of maximum nucleation population densities, if not more accurate nucleation densities than manual tracing methods allow.

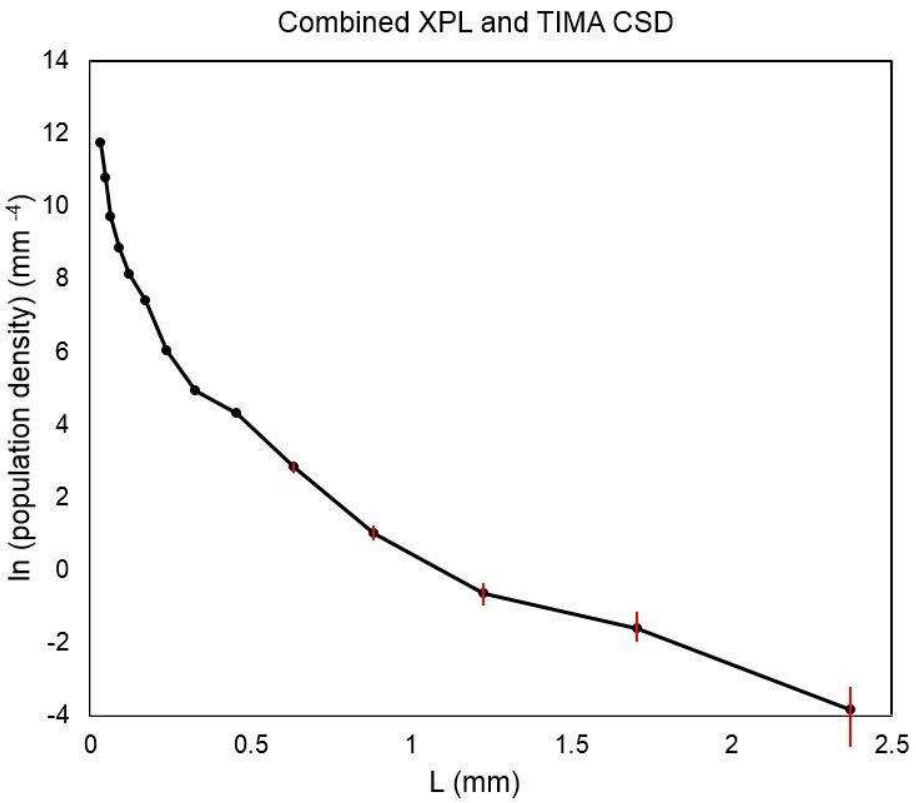


Fig. 2.17. CSD using phenocrysts from an photomicrograph tracing of sample L-E and groundmass information from a TIMA panorama image. The curve reflects seven bins per decade. A single aspect ratio was used (1.0: 2.5: 5.0) based on results from CSDSlice for the entire population. Removing larger phenocrysts and adding more groundmass particles either resulted in the same aspect ratio or in an increase of the long dimension from 5.0 to 5.5. Compositionally, the curve includes all plagioclase species from $An_0$ to $An_{100}$. Error bars reflect counting statistics only.

### 2.8.4 EBSD detection of fabric and discrete crystals in a complex cluster

Complex plagioclase twining, as viewed in static photomicrographs, can visually obscure boundaries of crystals that are components of dense clusters. Twinning presents challenges to obtaining accurate crystal lengths with manual methods. We compared the length measurements derived from a complex cluster and surrounding groundmass, from sample L-E, using four types of images: 1) photomicrograph, 2) BSE, 3) TIMA-derived phase image, and 4) EBSD-derived orientation map (Fig. 2.18). Only crystals that were components of the all-plagioclase cluster were measured, and the surrounding groundmass was ignored. BSE and TIMA phase images (Figs. 2.18B and C) only produce a single, contiguous particle although the cluster morphology suggests multiple crystals are present. EBSD detected 40 crystals that were

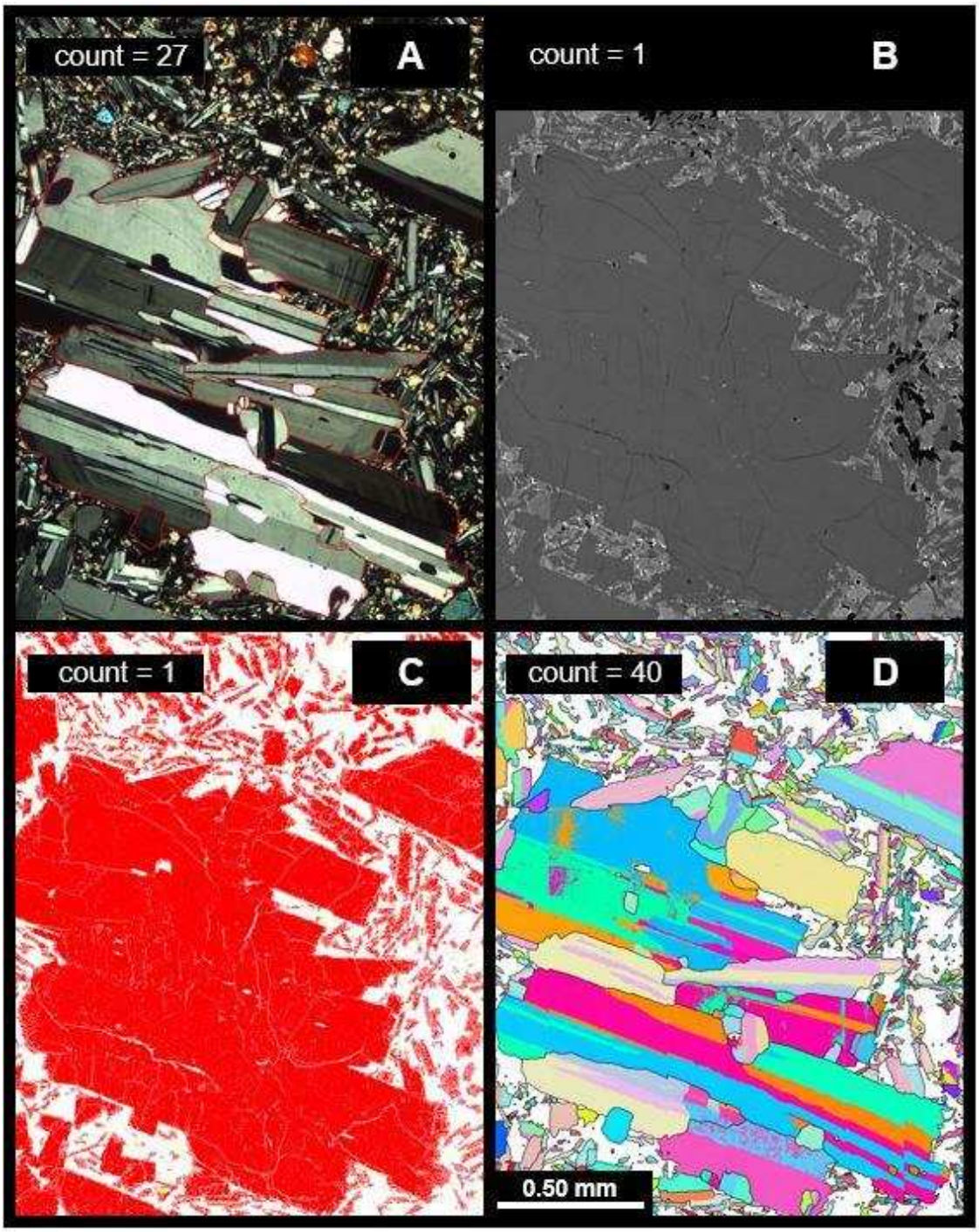


Fig. 2.18. A complex all-plagioclase glomerocryst, with surrounding groundmass, from sample L-E. Figure A shows outlines for 27 discrete crystals visually determined from a photomicrograph. B (BSE) and C (TIMA image) show the central cluster as a single, contiguous particle. D shows a color orientation map where different colors represent different orientations of plagioclase. The crystal count is greater for EBSD versus microphotograph and is mostly reflected in the groundmass-sized crystals that occur in the cluster (Table 2.4).

Table 2.5. Crystal detection from two of the four types of images in Figure 2.18. Measurements reflect longest-length types. XPL measurements here do not include an error of ~ ± 4 pixels (~13 μm) depending on XPL image shadowing and the extent of indistinct boundaries.

| EBSD and XPL discrete crystals within a single glomerocryst | | | | |
|---|---|---|---|---|
| Method | Number of crystals | | Longest-length range (μm) | Average phenocryst length (μm) |
| | Phenocryst | Groundmass | | |
| EBSD | 13 | 28 | 9.16-1561 | 642 |
| XPL | 16 | 11 | 40-1557 | 527 |

members of the cluster (Fig. 2.18D) whereas 27 were manually detected from the photomicrograph (Fig. 2.18A). The number of discrete phenocrysts and groundmass crystals detected as cluster components are summarized in Table 2.5. EBSD more accurately detected individual crystals than manual methods. Whereas photomicrographs require visual interpretation and user bias in determining discrete crystal boundaries, EBSD does not. For the all-plagioclase cluster from sample L-E, EBSD determined fewer crystal components than manual tracing (13 versus 16). This difference becomes significant with cluster-rich samples, as an average of three unidentified discrete phenocrysts across multiple clusters within a sample will variably affect CSDs.

In addition to crystal lengths, EBSD orientation maps yielded information on any preferred orientations of plagioclase phenocrysts and groundmass populations (separated by a 150 μm size threshold) as well as twin types. MTEX determined the following twin types (Fig. 2.18D): 29% albite, 12% carlsbad, 17% albite-carlsbad, 1.3% pericline and <1% other. MTEX also produced a qualitative fabric analysis using M-indices. A groundmass M-index of 0.05 and a phenocryst M-index of 0.09 suggest only mild orientation for the phenocryst population and almost no preferred orientation for the groundmass population. M-indices suggest agreement with assumptions of random microlite orientation for CSD analysis using CSDSlice and CSDCorrections. The groundmass M-index, however, only represents a very small area and caution should be applied to a fabric assumption. In the case of the

cluster from sample L-E, vesicle areas were purposely avoided because plagioclase lath alignment was noticed along vesicle walls. Increased vesicle presence may correlate to localized plagioclase alignment and so highly vesiculated samples may require a more thorough fabric analysis.

## 2.9 Discussion

The strengths of the various methods explored here for acquiring length measurements of crystals for CSD analysis are texturally and geochemically controlled. While manual tracing of high resolution images can provide accurate crystal lengths, this is a time-consuming method and discourages investigations of crystallization kinetics through CSD behavior. Automated analysis increases both accuracy and efficiency in obtaining length measurements, provided textural and geochemical characteristics of samples are acknowledged. Pixel sizes selected for automated analysis using SEM and EDX should reflect the size population sought after. A 2 μm pixel size for SEM scans may not be necessary if the crystal size population is suspected to be coarser. For very fine groundmasses typical of lavas, a high-resolution scan is appropriate but scan time (and cost) increases. In such cases, a smaller representative region of a larger thin-section may yield enough crystals to provide both robust aspect ratios and CSD plots.

Crystal contiguity may offset crystal fracturing such that CSD curves do not suggest that either factor dominates. Samples should ideally possess minimum crystal fracturing as well as minimal crystal contiguity. One way to resolve this for plagioclase is to create an increased number of narrower anorthite bins such that multiple size populations may be distinguished geochemically. More importantly, this distinction in geochemistry can be used to create images where crystal populations can be measured by thresholding the different size populations by color (Fig. 2.19). Adjusting anorthite bins to reflect the dominant anorthite content of size populations is necessary, as too many bins may create too many colors. Multiple colors within a single crystal should be avoided (Fig. 2.19, inset). Another approach involves thresholding multiple colors so that a single grayscale is produced.

Editing particles in isolated-particle images (clipping glomerocrysts into multiple plagioclase crystals) relies on an initial inspection of texture with a polarizing microscope and also on user

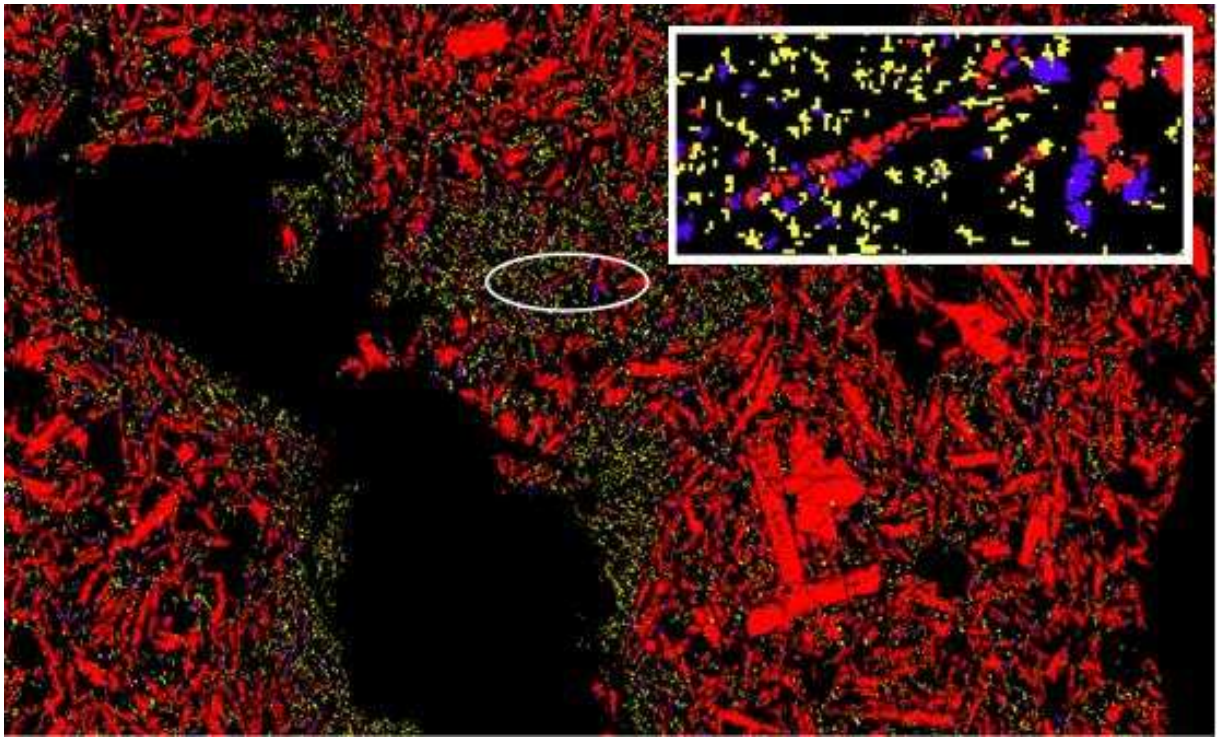

Fig. 2.19. TIMA-derived panorama phase image showing anorthite trends of phenocrysts versus groundmass. The field of view is ~3.5mm across. Phenocrysts are predominantly red, denoting $An_{64-89}$. In this example, yellow pixels represent $An_{0-50}$ and may be localized alterations of previously higher anorthite contents. The inset image in the upper right shows two elongated plagioclase crystals form the circled region, showing lower anorthite content on crystal ends and higher anorthite content centrally.

experience. More accurate counts of discrete crystals in a glomerocryst are acquired from tracing photomicrographs than using TIMA isolated-particle images. However, clustering behavior related to synneusis has the potential to be quantified by comparing TIMA glomerocryst images to manual tracings that extract the individual crystals from the clusters.

Groundmass plagioclase crystal measurements are challenging to obtain with certainty from a single photomicrograph. Although much of a single plagioclase crystal can be recognized in an image, groundmass sizes reach a lower size-threshold where borders are indistinct or unrecognizable. At this scale, bias in tracing methods can shift crystals to adjacent bins in a CSD. We experienced difficulty in tracing some crystals and so length errors reflect ~ 4-pixel distance from crystal borders. This results in a maximum of 8 pixels when applied to opposite crystal sides, which equates to ~16 μm maximum. For this research we attempted to use a stylus, but the method introduced even more error into measurements as

the tip is not physically small enough to provide pixel-level detail. Simple trackball control provided more accuracy in tracing than a stylus.

For plagioclase, the ability to constrain and refine size populations by geochemistry deserves more investigation. Since plagioclase is a solid solution series, the ability to determine phenocryst size while simultaneously ignoring the lower anorthitic groundmass population (or any other crystal population with a different anorthite content) is a valuable tool. Using elemental information, preferably refined by microprobe analysis or similar, can assist in correlating composition to size populations. Although we use a semi-quantitative approach to define anorthite content in samples by assuming stoichiometric composition, the approach is the same: refine size populations by chemical character and then analyze populations by that chemical character or any combination thereof.

EBSD analysis suggests that for certain textures, orientation-based imaging may provide more accurate crystal sizes and counts than phase-based imaging. The choice involves a fundamental difference in the purpose of the images created by the two approaches: where TIMA SEM-EDS defines a crystal based on geochemically-defined area, EBSD imaging defines a crystal based on crystal orientation. In finalizing EBSD images, multiple re-indexings and a noise-reduction process are often performed to "fill-in" missing pixels (Fig 2.20). In effect, this minimizes any internal pixel loss of crystal image due to minor fracturing or inclusions of other phases. Textures that show significant fracturing may be more suitable for EBSD imaging rather than TIMA imaging. EBSD can also recognize polymorphs, which element-based imaging cannot. Again, geochemistry and texture are the controlling factors in choosing the proper imaging method.

EBSD is not affected by contiguity issues of densely-packed monophase textures and instead relies on an orientation threshold between adjacent orientation points (scan points). For resolving glomerocrysts into discrete crystals in our EBSD analysis, a larger step size would be more appropriate than the 2.5 μm step we chose. However, with that smaller step size and accounting for twin offsets in MTEX, 1345 plagioclase crystals were accounted for in the area shown in Figure 2.18D. With a TIMA-based image, over 6000 particles were detected, and this result may have been due to a strongly fractured

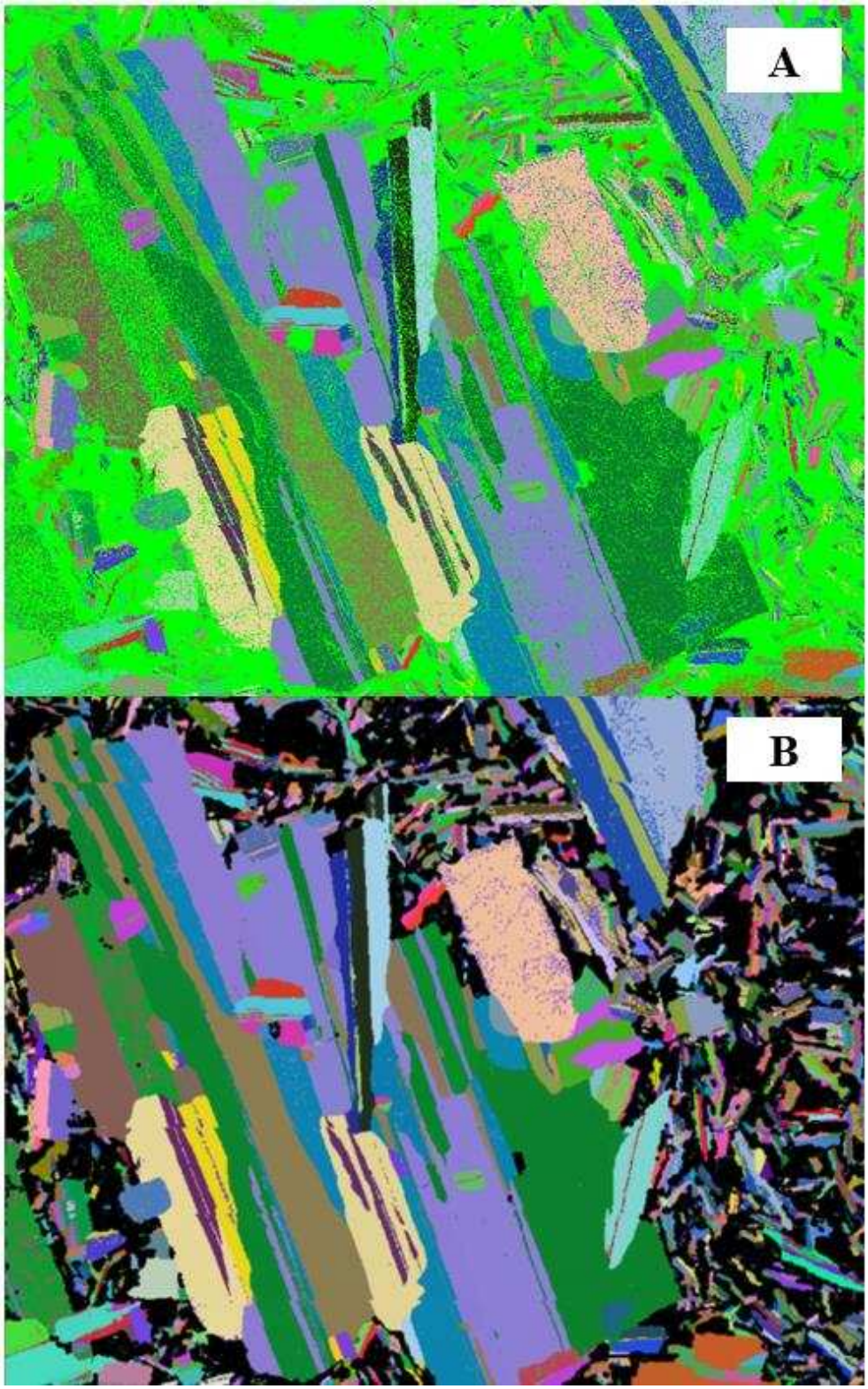


Fig. 2.20. EBSD orientation images before (A) and after two additional re-indexings and an extensive noise reduction process (B). Bright green in A denotes points of zero-solutions as only plagioclase was scanned for. The background color in B was changed from green to black for visual clarity.

sample. Although using noise correction in ImageJ (the Despeckle function was applied four times) eventually produced ~1390 particles over a similar area, noise correction can also introduce increased particle contiguity.

Although the EBSD M-index characterizes fabric qualitatively from 0 to 1, a number close to 0 may only describe localized orientation and therefore multiple analyses are required. The glomerocryst we examined in sample L-E consisted of discrete plagioclase crystals that simultaneously go extinct in polarized light microscopy. This strong optical continuity occurs for multiple glomerocrysts in the larger thin section. Provided that these types of glomerocrysts are all randomly oriented, true aspect ratios may not be significantly affected. However, over a small sample size when the largest plagioclase crystals are bound in one or a few glomerocrysts that show optical continuity of extinction, an inaccurate aspect ratio may result which may affect CSD curves.

The effects of swallowtail forms (and cut-sections made through their tails) on a potential increase in the finer groundmass size populations were not examined. Although there should be some contribution to the smaller groundmass size population, the count may be offset by the fact that swallowtail termination cut-sections may be smaller than the thickness of the thin-section (the intersection-probability effect). Although approaches have been devised that model random cuts through simple solids (Morgan and Jerram, 2006), more complicated forms have not been similarly analyzed.

Automated scan methods are costly when compared to BSE image acquisition and manual tracing of XPL images. A combination of manual methods, proper sample textural considerations and preparation, along with the assistance of automated analysis, can produce accurate crystal length measurements for meaningful CSDs.

### 2.10 Implications and future research

Challenges in crystal size distribution application stem from 1) resolving the sizes of the finest crystal fractions, 2) properly converting cut-section shapes and lengths from 2D thin sections into accurate volumetric equivalents, and 3) reducing the amount of time that traditional manual tracing methods require. Automated analysis has the potential to address the small-size fraction crystal lengths

using either geochemical signatures or crystallographic information, the choice of which depends on the phase in question and the overall sample texture. For stereological issues, the dominance of anhedral crystal shapes such as swallowtail plagioclase and dendritic magnetite are problematic to model mathematically. Instead, irregular crystal shapes require direct modelling to constraint aspect ratios from random cut-sections. The work of Morgan and Jerram (2006) in modelling random cuts through polyhedra is a indication that more modelling is required. One of the approaches recommended is that of voxel modeling. By using 3D pixels to create irregular shapes, random cut-sections may be applied to constrain statistically significant aspect ratios. The approach is already used in GIS and animation, and so an opportunity exists to create a program where the user creates a set of shapes through which random cuts are applied. Another approach for refining aspect ratios for size populations is to perform tomographic analyses on selected crystals of multiple sizes. By creating a 3D image from stacked-slice images of crystals in a natural sample, real-world aspect ratios can be correlated, confirmed and refined against modelled results.

The Laki fissure eruptions are significant in that the event produced a volumetrically significant and historic magma outpouring that disrupted the climate and human survivability for years. Each of the ten eruptions are part of a complex, multi-textured and multi-lobed pahoehoe flow. This type of flow can serve as an analogue for other terrestrial flow events in our solar system. A per-lobe analysis of changes in texture and geochemistry lengthwise and vertically across each flow is warranted. The Laki region serves as a rich source of information on large scale basalt eruptions, and although research continues in the area, a lack of diverse perspectives mandates a reconsideration of sampling logic and a re-evaluation of magma chamber processes and flow dynamics.

CHAPTER 3

# INSIGHTS INTO GROUNDMASS-DEFINED CRYSTAL SIZE DISTRIBUTIONS AND CRYSTALLIZATION KINETICS USING AUTOMATED ANALYSIS

A paper to be submitted to *American Mineralogist*

K.A. Cone, R. F. Wendlandt, K. Pfaff

## 3.1 Abstract

Volcanic textures present challenges in constraining kinetic parameters through crystal size distributions (CSDs). Manual tracing of groundmass crystals is often time consuming and high-resolution images are often required. Automated SEM analysis can efficiently produce multi-field phase images at high-resolutions and offers an opportunity to address the size populations of tens of thousands of groundmass crystals during a single scan, thus eliminating the need for manual tracing of crystals from photomicrographs. Since plagioclase is ubiquitous in basalts, various crystal size populations of this phase are often present in a single sample and thus record long-term geochemical and kinetic aspects of lava crystallization history. Here we used four samples from the well-documented Laki, Iceland fissure eruptions of 1783-1784. Crystal size distributions were produced using two approaches: 1) length measurements of plagioclase crystals were obtained from photomicrographs by manual tracing of phenocrysts ≥ 150 μm, and 2) length measurements combining the above with those from multi-field phase images from automated SEM analysis for plagioclase crystals < 150 μm. Automated SEM results suggest an increasing rate of nucleation over time for erupting magma systems and nucleation population densities up to three orders of magnitude greater than regressions through CSD curves defined by only manually traced phenocrysts. CSD curves produced here for our Laki samples are similar in shape to those previously reported. Automated SEM analysis can refine the interpretation of groundmass populations, thus permitting detection of subtle variations in kinetic characteristics across samples.

## 3.2 Introduction

Crystal size distributions (CSDs) are an aspect of textural analysis often used as a companion tool to the traditional methods of geochemical major, minor and trace elemental analyses. Where geochemical

analysis provides fundamental information on the temperature, pressure and composition of evolving melt environments, CSDs provide the associated quantitative kinetic information through crystal size populations (Marsh, 1988; Cashman and Marsh, 1988; Higgins, 2000, 2006). These size populations reveal nucleation and growth histories by comparisons to theoretical end-member behaviors, and deviations from these ideal populations indirectly reveal probable physical mechanisms at work in magma chambers as well as in post-eruptive environments (Marsh 1988, 1998). The use of CSDs alongside geochemical analyses therefore provides a more complete crystallization history than geochemical analyses alone.

Volcanic rocks often originate from magma systems where nucleation and growth occur simultaneously over time, and this is evidenced in seriate textures. Even a classic bimodal appearance contains some degree of simultaneous nucleation and growth, and as such, most "bimodal" rocks may not actually be truly bimodal (Hersum and Marsh, 2007). Given that magma chambers are open to an underlying plumbing system and to periodic recharge, CSDs for volcanic rocks are often modeled using an ideal steady-state, open igneous system. Here, there is a log-linear relationship when crystal population density is plotted against size for a single phase: $\ln(n(L)) = - L/(G\tau) + \ln (n^0)$. The first term represents population density, L is crystal length, G is the average crystal growth rate, $\tau$ is residence time, and $n^0$ is nucleation density. Other characteristics may be derived from this equation. The average crystal size (i.e. characteristic length, C) can be calculated as $G\tau$ (as well as by -1/regression slope) and the nucleation rate (J) as $n^0G$. The most common use of CSDs in igneous petrology is to extract nucleation rates and residence times.

Multiple challenges exist in obtaining CSDs. One issue is the interpretation of nucleation rates from CSD curves where back-extrapolation is performed to the y-axis (the population density axis) to infer a nucleation density. This approach is a result of the common practice of manually tracing phenocrysts from either backscatter electron images (grayscale digital images) or from photomicrographs where image resolution often dictates the minimum size of a crystal confidently measured. Crystal lengths derived from only manual tracing creates uncertainty of crystal population sizes at the finest-size

fractions. To address this concern, we combine the use of manual tracing and automated SEM phase-imaging at high resolution for obtaining plagioclase crystal sizes for the finest-size fractions (refer to Chapter 2 for a complete method overview). Plagioclase is ubiquitous in volcanic rocks and crystallizes over a wide range of temperatures and pressures, from early formed phenocrysts to late-stage groundmass, while also serving as a sensitive fingerprint of evolving magma geochemistry.

Another challenge lies in the interpretation of two-dimensional, linear measurements. CSD analysis requires not only accurate 2D measurements derived from thin section images, but also an accurate interpretation of those 2D measurements so that they best represent real-world volumetric equivalents. This problem is not only compounded by measurement bias inherent in manual methods, but also by measurements of crystal shapes other than perfect, non-contiguous spheres. Because crystals are not perfect spheres, length measurements must be stereologically converted (Higgins 2000, 2006; Mock and Jerram 2005; Morgan and Jerram 2006). Since plagioclase assumes a wide range of aspect ratios reflecting evolving crystallization conditions, a single shape about which length measurements are converted to volumetric equivalents cannot be assumed. Changes in shape during growth is of particular interest here since we use samples from the historic Laki, Iceland fissure eruptions that have been interpreted to contain entrained phenocrysts from crystal mush (Passmore et al., 2013; Neave et al. 2013, 2017). To address changes in plagioclase crystal shapes and sizes, we use two programs: 1) CSDSlice to determine the best-fit aspect ratio of various plagioclase populations; and 2) CSDCorrections to address cut-section effects (maximum crystal widths are rarely produced from random cuts) and intersection-probability effects (larger crystals are more likely to be intersected than smaller ones).

### 3.3 The Laki eruptions of 1783-1784

The historic Laki fissure eruptions were a voluminous eight-month long eruptive event in the Eastern Volcanic Zone (EVZ) of Iceland that resulted from the spreading between the European and North American plates. The larger two-year volcano-tectonic event culminated in more than 15 $km^3$ of lava distributed over an area of 565 $km^2$, with most of the discharge (~90%) produced within the first five months (Thordarson and Self, 1993; Fig. 3.1). A set of ten en-echelon fissures propagated from the

southwest towards the northeast, with each fissure representing one of the ten discrete eruptive episodes. Earthquake swarms began in May of 1783 followed by the first of eruptive episode in June. Individual eruptions were discerned based on preserved tephra deposits, stratigraphy, and historical accounts, with each being observed to have displayed early phreatomagmatic behavior due to the intersecting water table. Eruptive styles evolved to sub-Plinian and then to Hawaiian as the water table lowered (Thordarson and Self 1993; Guilbaud et al. 2007). The ~27 km mixed-cone row that resulted from the eight-month long eruption is segmented into eastern and western halves by the centrally located Laki mountain. The first five episodes occurred on the west side of Laki mountain with discharge directed toward the south within the Skaftá river gorge. The last five episodes occurred on the east side of Laki with discharge directed south within the Hverfisfljót river gorge.

More recent analyses of Laki lavas suggested that earlier conclusions of geochemical homogeneity (Sigmarsson et al. 1991) were incorrect. In an extensive determination of major, minor and trace element concentrations, Passmore et al. (2012) considered 47 basalt samples and 7 tephra samples across the entire ten-fissure event. They concluded that bulk rock geochemistry was strongly influenced by phenocryst abundance and that more primitive phenocryst characteristics were noted in the later stages of the eruption through crystal mush entrainment and contamination. Neave et al. (2013) investigated the relationship between crystal and carrier melt for the Laki system and suggested that trace element analysis of olivine-hosted melt inclusions pointed to concurrent mixing and crystallization of different mantle melts. They concluded that zoned plagioclase cores were the most primitive in composition of all phenocrysts and that these crystals originated in the shallow mantle. Neave et al. (2017) attempted an analysis of four Laki lava samples using automated SEM-based analysis to assess both geochemical character and crystal size distributions and also concluded that crystal mush entrainment was more efficient during later stages of the eruption.

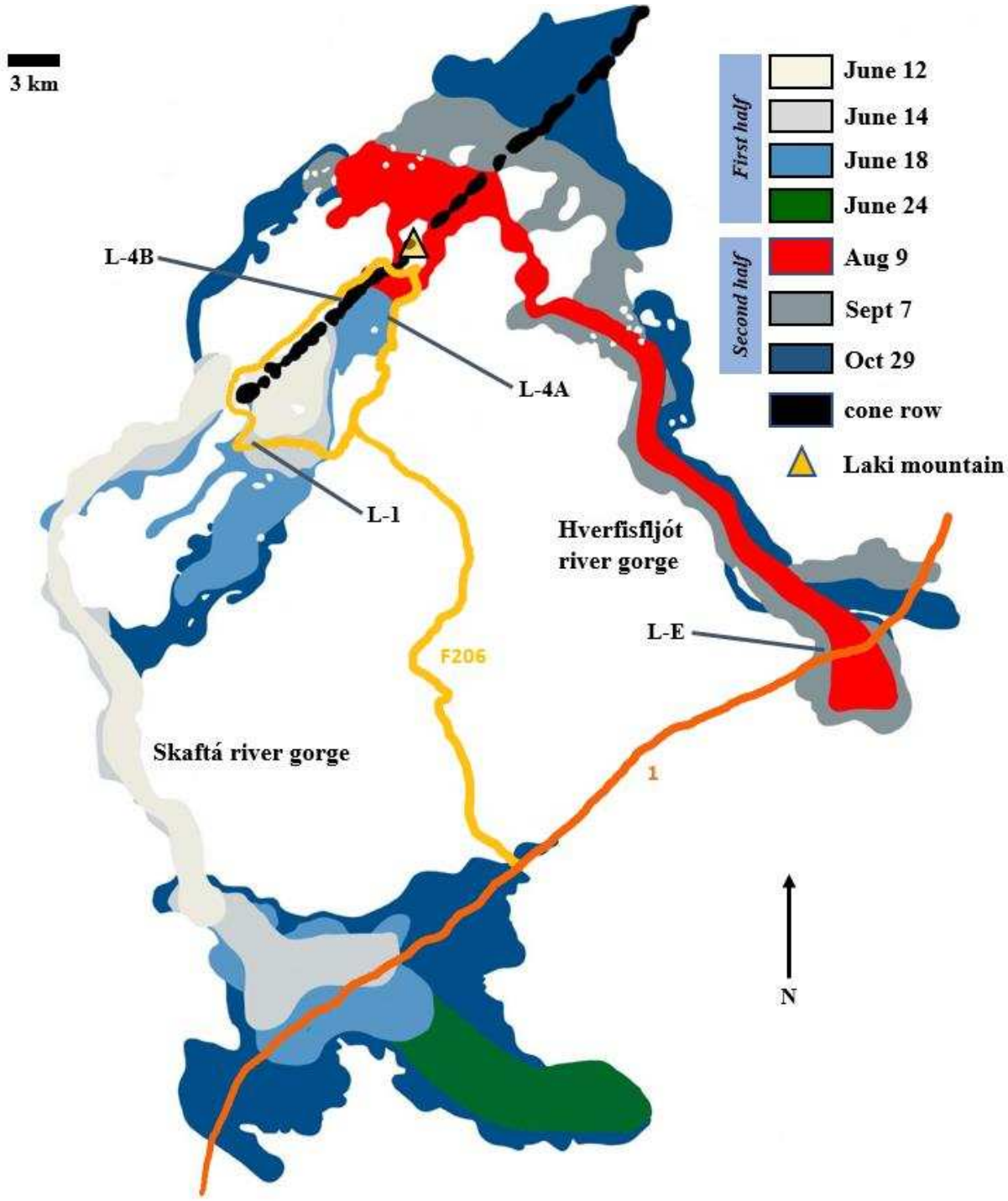


Fig. 3.1. The Laki flows, with locations for L-4A, L-4B, L-1 and L-E indicated. The two main branches are marked and likely preserved a consistently high temperature gradient for flows that terminated at the end of the branches. The yellow triangle at the center of the cone row represents Laki mountain and is used to define NE and SW segments that each contain five eruptive events, and therefore, five fissures. Route locations are approximate. Figure modified from Passmore et al. (2012).

### 3.4 Petrographic and textural characteristics

Four thin sections from four lava samples from the Laki eruption were prepared by Wagner Petrographics, Utah, and polished to 0.25 μm. Dominant phenocryst styles (discrete crystals and crystal clusters) as well as vesicle area are summarized in Tables 3.1, 3.2 and 3.3. For consistency in comparisons of Laki analyses between our work and Passmore et al. (2012) and Neave et al. (2013, 2017), we maintain their size definitions of phenocryst and groundmass using their defining size of 150 μm. All samples contained the same basic phases: plagioclase, clinopyroxene, olivine and groundmass-only dendritic opaques. The samples represent a mineralogically simple tholeiitic basalt (sample images are available in the digital repository). All our samples suggest vesicles percentages less than ~30 on a whole thin-section scale, as determined by ImageJ (Schneider et al., 2012), where photomicrographs were digitally traced for vesicle content and then converted to 8-bit grayscale images for thresholding.

Mineralogy of the Laki basalts suggests a homogenized tholeiitic basalt where early-formed phenocrysts consist of plagioclase, clinopyroxene and olivine (rare) in a groundmass of plagioclase, clinopyroxene, olivine and Ti-Fe oxides (dendritic titanomagnetite). Mineralogical determination has remained consistent over multiple studies (Bindeman et al. 2006; Guildbaud et al. 2005; Passmore et al. 2012; Neave et al. 2013, 2017).

Table 3.1. Vesicle percent as determined in ImageJ. Low, medium and high headings designate subjective area percents based on threshold grayscale adjustment: low designates incomplete vesicle grayscale saturation due to extreme, early groundmass color saturation that matched that of vesicles. High suggests that a volume of groundmass has reached the vesicle saturation grayscale such that the groundmass volume visually matches the non-saturated portions of the vesicles by area. Medium suggests that some balance between low and high conditions was visually achieved.

Vesicle % area for group A thin sections

| | Low | Medium | High |
|---|---|---|---|
| L-4A | 27 | 30 | 33 |
| L-4B | 21 | 24 | 29 |
| L-1 | 17 | 19 | 20 |
| L-E | 15 | 16 | 17 |

Table 3.2. Major petrographic characteristics for all four samples for discretely occurring phenocrysts. *Rare occurrences of large sieved plagioclase are similar to that mentioned and shown by Guilbaud et al. (2007). **In some instances, all-cpx clusters may actually be cpx+pl (minor) clusters.

Laki basalt phenocryst characteristics (Discrete)

| Sample | Phase | ~Size (mm) | Shape | Twin style | Texture/Observations |
|---|---|---|---|---|---|
| L-4A | pl | up to 0.50 | ~7:1 (l:w) | polysynthetic and simple | greater l:w for smaller crystals (non-groundmass); zoned |
| | cpx | up to 0.20 | equant | simple and sector zoned | sometimes near sub-ophitic or anhedral; equant to subequant |
| | ol | up to 0.25 | equant to sub-equant | none observed | euhedral to near euhedral; some show resorption |
| L-4B | pl | up to 0.70 | subhedral to euhedral | polysynthetic and simple | zoned, sub-euhedral to euhedral |
| | cpx | up to 0.15 | euhedral, equant | simple and sector zoned | subophitic** to true cluster |
| | ol | up to 0.30 | subhedral, equant to subequant | none observed | minor border resorption, rare Fe alteration (brown) |
| L-1 | pl | up to 1.20 for internally sieved*; up to 0.40 for most | elongate to acicular (rare exceptions) * | polysynthetic and simple | large sieved plagioclase occurs only once in thin section*; zoned |
| | cpx | up to 0.20 | equant | simple and sector zoned | subhedral to euhedral |
| | ol | up to 0.30 | subelongate | none observed | anhedral to euhedral: euhedral only observed in groundmass |
| L-E | pl | up to 0.80 | subhedral to euhedral | polysynthetic and simple | some fractured crystals (as a product of more 1:1 forms); zoned; rarely internally sieved |
| | cpx | up to 0.30 | equant | simple and sector zoned | most occur as cluster members; largest crystals are cluster members |
| | ol | up to 0.45 | subhedral euhedral | none observed | some fractured-as-discrete forms; more subhedral forms show internal resorption |

Table 3.3. Major petrographic characteristics for phenocrysts that occur as crystal clusters (i.e. glomerocrysts).

Laki basalt phenocryst characteristics (Clusters)

| Sample | Style | ~Size (mm) | Texture/Observations |
|---|---|---|---|
| L-4A | pl-only | up to 1.5 | sometimes continuous extinction; zoned and twinned (x2) |
| | cpx-only | up to 0.30 | rarely observed without pl; restricted to two or three crystals, sometimes in optical continuity |
| | pl+cpx | up to 1.25 (rare), typically up to 0.75 | often sub-ophitic |
| | pl+cpx+ol | up to 0.25 | rarely observed |
| L-4B | pl-only | up to 2.0 | sometimes continuous extinction; zoned and twinned (x2) |
| | cpx-only | up to 0.25 | clusters of two to four crystals |
| | pl+cpx | up to 1.35 | often sub-ophitic with smaller occurrences larger ones are discrete-discrete clusters |
| | pl+cpx+ol | up to 0.40 | rare |
| L-1 | pl-only | up to 1.15 | double all-pl clusters occur (rare) |
| | cpx-only | up to 0.20 | up to two contiguous crystals |
| | pl+cpx | up to 0.35 | often sub-ophitic; also discrete-discrete cluster |
| | pl+cpx+ol | up to 0.40 | appears fractured when in clusters |
| L-E | pl-only | up to 3.5 | microlite flow alignment around largest cluster/s (product of two joined discrete-clusters?) |
| | cpx-only | up to 0.40 | up to three contiguous members |
| | pl+cpx | up to 2.0 | often sub-ophitic; largest cluster contains the largest cpx crystals, up to 1.1mm |
| | pl+cpx+ol | up to 0.90 | rarely observed |

### 3.5 Methods and materials for length determination

#### 3.5.1 Manual tracing and imaging

Thin section photomicrographs were captured on a polarizing microscope and traced for plagioclase crystals ≥ 150 µm using Adobe Photoshop. Trace times were directly related to the area and number of phenocrysts present and varied from three hours to ~20 hours (sample L-E). In all cases, well-defined crystals (i.e. crystals with defined borders) that could be confidently recognized that were several microns smaller than 150 µm were also traced. Discrete plagioclase crystals occurring in glomerocrysts were also isolated by manual tracing so that cluster sizes were reduced to represent more accurate length measurements of crystal members. This approach is necessary to prevent artifact enlargement effects of the larger phenocrysts (which in turn affects CSDCorrections size population interpretations). The longest-length dimension was used to determine the minimum size of 150 µm. Accuracy in tracing was predicted by visual estimation, and in most cases, this produced possible variations by up to ~5 pixels, which in turn equated to ~7.5 µm. This type of error was mostly due to crystal borders that displayed various degrees of resorption or crowding by other crystals. Traced plagioclase crystals from microphotographs were then imported into ImageJ (Schneider et al., 2012) imaging software for length and width determination for each crystal using a best-fit ellipse. Photomicrographs were calibrated against automated-SEM phase images for consistency in length measurements between image types. Both manually-traced and automated-SEM derived measurements were produced with ImageJ (8-bit grayscale thresholding, best-fit ellipse dimensions) and then treated with CSDSlice and CSDCorrections. Each of the four samples was divided into three populations: the manually-traced phenocryst population (≥ 150µm), the next smallest population (groundmass, GM1) and then the next smallest population (groundmass, GM2). GM1 and GM2 each consist of 4088 crystals and are derived from automated-SEM phase images. Each of the three populations were then treated separately with CSDSlice to determine if different aspect ratios were inherent in different crystal size populations. CSDCorrections was then used to produce bin values for CSD diagrams. All phenocryst populations were binned at 8 bins per decade.

To obtain length measurements of plagioclase crystals from either photomicrographs or automated-SEM phase images, ImageJ settings were as follows: Type → 8-bit binary, Adjust → Threshold (to include all peaks, and therefore all plagioclase species), Set Measurements → Area, Centroid, Fit ellipse (same centroid and orientation of the original particle), Limit to threshold, Decimal places → 3. Analyze Particles was finally performed to obtain major and minor axes measurements using the following settings: Size → 10-Infinity (to remove any outliers), Pixel units, Circularity → 0.00 – 1.00, Outlines (optional), Include holes (optional, depending on the degree of mottling present).

### 3.5.2 Automated SEM analysis (TIMA)

Automated analysis was performed at the Colorado School of Mines' Automated Mineralogy Laboratory using a TESCAN-VEGA 3 Model LMU VP-SEM with four PulseTor 30 $mm^2$ EDX detectors, a YAG scintillator BSE detector, and TIMA software version 1.5.26. Analysis was initiated using the control program TIMA3. Scan conditions for EDX analysis included an accelerating voltage of 25 keV and a beam intensity of 14.5.

Plagioclase was calibrated by first establishing a representative BSE brightness range from point analysis of samples. Brightness values ranged from 19.8 to 22.5. An EDX X-ray spectrum is acquired at each scan point that falls within the BSE brightness range. EDX spectra for each pixel was produced from 1000 X-ray counts at a spatial resolution of 2 µm. The EDX spectra are compared against a database which allows a mineral assignment on a per-pixel basis. Scan times ranged from ~6 hours for L-4B and ~17 hours for L-E. Definitions were created for the degree of anorthite content shown in the bins listed above so that spectra produced images reflecting the binned values. Spectra are acquired for smaller regions (fields) and TIMA software automatically stitches the fields together to produce the full, larger image. The result is a digital image of plagioclase crystals superimposed onto a BSE image.

TIMA phase images of plagioclase were binned as $An_0 – An_{50,}$ $An_{50} – An_{64,}$ $An_{64} – An_{89,}$ and $An_{89} – An_{100}$, following the logic of the Passmore et al. (2012) definition of a plagioclase groundmass minimum and maximum values of $An_{51}$ and $An_{64,}$ as well as plagioclase core values up to $An_{89}$. These anorthite bins are also similar to the reported values in Guilbaud et al. (2007) (primitive plagioclase cores

>$An_{70}$ and groundmass and phenocryst rims of ~$An_{49-70}$). Neave et al. (2017) utilized $An_{64}$ to distinguish between groundmass and phenocryst. Because automated analysis is a semiquantitative method of determining elemental composition, plagioclase formulas were assumed to be stoichiometric and consisted only of Ca, Na, Al, Si, and O. These stoichiometric formulas defined the anorthite percents that determined plagioclase bin boundaries of $An_0$, $An_{50}$, $An_{64}$, $An_{89}$ and $An_{100}$. To determine length measurements, all anorthite concentrations were considered in phase images (i.e. all plagioclase pixels from $An_0$ to $An_{100}$ were included in measurements). Images were processed with ImageJ by converting the original image to an 8-bit grayscale and then thresholded for best-fit ellipse dimensions, similar to the manual tracing method. Our basalt samples show mineralogical consistency against descriptions reported by Passmore et al. (2012) for over 54 Laki samples. Incorrect binning for some pixels is expected but not to the extent that size measurements are affected by more than the maximum length measurement errors from manually traced thin sections.

### 3.5.3 Stereological corrections and crystal size distributions

The CSDSlice version 5 (Morgan and Jerram, 2006) program compares a database of 2D shape curves produced from random cross-section cuts of 703 different habits against uncorrected 2D measurements. This produces a series of ranked, best-fit aspect ratios required for further stereological correction and CSD production in CSDCorrections (Higgins, 2000). CSDCorrections version 1.51 was used in this study to produce 3D length equivalents from raw 2D measurements from thin sections (photomicrographs and TIMA phase images). All measurements were extracted from images using a best-fit ellipse method with ImageJ. CSDCorrections accounts for the intersection probability effect (larger particles are more likely to be intersected than smaller ones) as well as for the cut-section effect (cut-sections rarely reflect maximum lengths). These approaches are discussed in detail by Higgins (2000, 2006).

Crystal size distributions show the true, reinterpreted length measurement (L) plotted against a crystal population in units of n(L) $mm^{-4}$. In other words, the number of crystals (n) of a given corrected

2D length measurement (L) per unit volume are plotted on the y-axis as a function of corrected length (L). Binning occurred at 8 bins per decade unless otherwise noted.

Although most silicate kinetic growth rates have been reported to be similar at ~$10^{-10}$ or $10^{-9}$ mm/s (Cashman 1990; Higgins 2006) and have been used in numerous studies, other rates have been reported to vary over five orders of magnitude depending on the main crystallization drivers (Brugger and Hammer 2010, and references therein). Here we chose a slow rate of crystallization at $10^{-10}$ mm/s given the volumetric enormity of the flow (~15km$^3$ of lava) and the predicted thermally efficient transport of lava flows over great distances (Guilbaud et al. 2007). A growth rate is necessary to calculate all other kinetic parameters from CSDs. All errors in CSDs produced by CSDCorrections result from counting statistics only and do not reflect inconsistencies in measurements (Higgins 2000, 2006).

### 3.6 Results

Aspect ratios for each of three crystal populations for samples L-4A, L-4B, L-1 and L-E are shown in Figure 3.2. For statistically significant aspect ratios determined by CSDSlice, at least 75 crystals are required for tabular shapes, at least 250 crystals for acicular shapes, and more than 250 crystals when the shape distribution is unknown (Morgan and Jerram, 2006). Traced phenocryst totals for the samples are as follows and are sufficient for robust aspect ratios: L-4A (366), L-4B (111), L-1 (352), and L-E (733). Larger rectangular prisms with length-to-width ratios of a minimum of 5:1 and a maximum of 10:1 occur and are similar to the reported minimum length-to-with ratio of > 4 by Neave et al. (2017). Phenocryst populations showed greater length-to-width ratios than either GM1 or GM2 populations, and GM1 aspect ratios also showed greater length-to-width ratios than the finer-sized GM2 populations. Our processing of crystal sizes by multiple population for aspect ratios suggest that populations vary in shape more frequently for seriate samples like L-E than for more bimodal textures such as L-4B.

Groundmass crystal measurements (< 150 μm) from TIMA images were combined with measurements from manual tracings of phenocrysts (≥ 150 μm) in microphotographs and resulted in curved-upward CSDs with increased slopes and increased linear trends at the smallest L-values

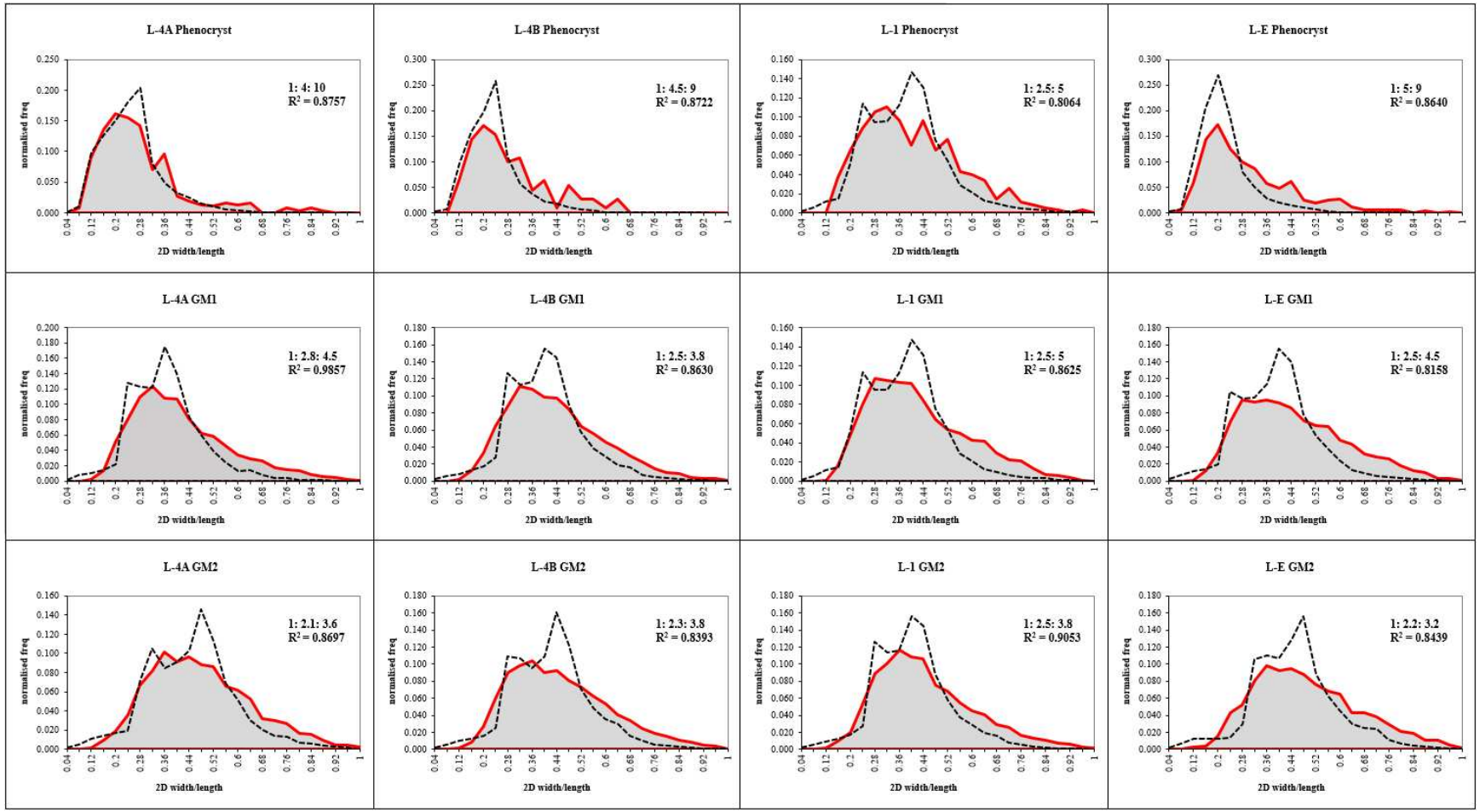


Fig. 3.2. Evolution of plagioclase aspect ratios as a function of population size. Each column represents one of the four samples, with traced phenocryst aspect ratios in the top row, GM1 in the center, and GM2 in the bottom row. $R^2$ values determined from CSDSlice suggest strong fits against model aspect ratios. Lower rows reflect smaller, less prismatic crystals and shorter length-to-width values. Upper rows suggest greater length-to-width aspect ratios and more prismatic shapes.

(Fig. 3.3). CSDs from phenocryst-only photomicrograph tracings show turndowns at the smallest L-values (Fig. 3.4), likely due to inadequate crystal counts in the associated bins.

The choice of where to place regressions through CSD curves is based on where the user chooses to define a nucleation density. In the case of curved-upward volcanic CSD curves, multiple regression lines may be used to define multiple nucleation densities for different parts of the curve (i.e. different portions of a crystallization history, but this approach may also be invoked when magma mixing is suspected). Here, we chose two approaches for derived kinetic data for Table 3.4: 1) placing regressions through curves from manually traced phenocryst measurements (TR, Fig. 3.4), and 2) placing regressions through curves from combining manual tracing and TIMA images measurements (TR+AM). Based on the regression slopes indicated in Table 3.4 (i.e. through the entirety of curves in Figures 3.3 and 3.4), kinetic characteristics suggest nucleation population densities vary by a factor of 3, as indicated by "TR" and "AM+TR" $\ln(n^0)$ values (Table 3.4). Because refining groundmass sizes causes increased slopes, residence times are directly affected and shortened, as suggested by $\tau$ values. The more seriate textures of L-E and sub-seriate texture of L-1 show the smallest changes in nucleation rates (J) between TR and TR+AM values, with L-E showing the least change. These observations suggest that strongly seriate textures may only require back-extrapolation from CSD curves produced by manual tracing to provide robust kinetic data. Table 5.4 suggests a general trend of increased correlation of kinetic data with increased seriate texture.

### 3.7 Discussion

Although both groundmass-driven CSD curves (Fig. 3.3) and phenocryst-based CSDs (Fig 3.4) show concave-up curves, nucleation densities resulting from TIMA phase images were always greater. A similar conclusion was reached by Neave et al. (2017) using automated analysis (QEMSCAN; Qualitative Evaluation of Minerals by SCANning electron microscopy) in investigating Laki basalts. Although manually tracing phenocrysts from high-resolution photomicrographs still provides an accurate method for obtaining length measurements of crystals $\geq 150\mu m$ (particularly since plagioclase twinning and

Table 3.4. Kinetic parameters from both plagioclase groundmass-derived and phenocryst-derived CSDs, as shown in Figures 3.3 and 5.4. TR = measurements from traced phenocrysts, and AM = automated mineralogy (TIMA-based) phase-image measurements. C = average crystal size, J = nucleation rate and $n^0$ = nucleation density. Table values were determined as follows, based on an assumed crystal growth rate of G = $10^{-10}$ mm/s: C was determined using the calculated regression slopes from CSDCorrections (m), where C = -1/m; $n^0$ was determined from CSD corrections; J = exp ($\ln(n^0)$) * G; and $\tau$ is defined as C/G/($3.154*10^7$).

**TIMA-derived versus tracing-derived kinetics**

| Sample | Slope | | ln ($n^0$) | | C (mm) | | mean $\tau$ (yrs) | | J ($mm^{-3}$ $s^{-1}$) | |
|---|---|---|---|---|---|---|---|---|---|---|
| | TR | AM+TR | TR | AM+TR | TR | AM+TR | TR | AM+TR | TR | AM+TR |
| L-4A | -5.30 | -6.78 | 6.55 | 8.63 | 0.189 | 0.147 | 60 | 47 | 6.99E-08 | 5.60E-07 |
| L-4B | -4.32 | -6.44 | 4.31 | 7.32 | 0.231 | 0.155 | 73 | 49 | 7.44E-09 | 1.51E-07 |
| L-1 | -8.15 | -10.2 | 7.46 | 9.23 | 0.123 | 0.098 | 39 | 31 | 1.74E-07 | 1.02E-06 |
| L-E | -5.06 | -5.26 | 6.26 | 6.64 | 0.198 | 0.190 | 63 | 60 | 5.23E-08 | 7.65E-08 |

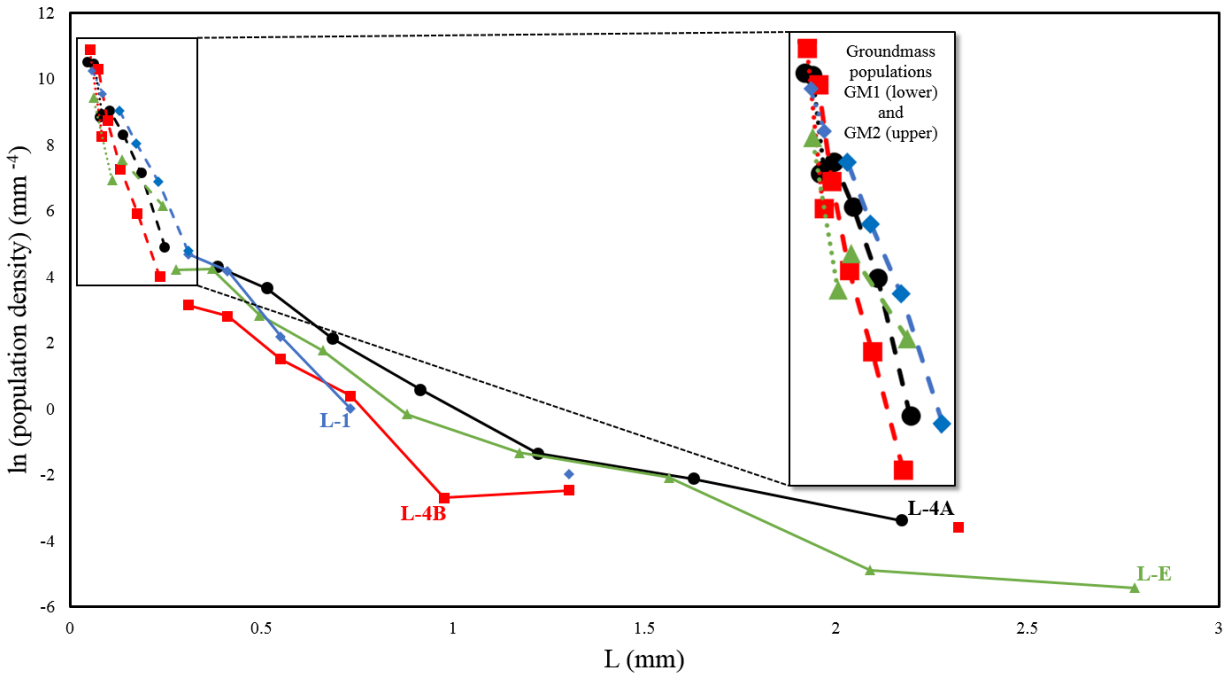


Fig. 3.3. CSDs for the four Laki samples using a combination of measurements from automated analysis phase image groundmass crystals and manually traced phenocrysts. Solid lines represent phenocrysts, dashed lines represent GM1 and dotted lines represent GM2. For L-4B GM2, L-1 GM 2, and L-E GM1/GM 2, fewer bins were used (5, 6, and 4, respectively). This was done to preserve linearity, as groundmass crystals (calculated with different aspect ratios than those used for phenocrysts) naturally increase in number as size decreases, and so binning logic here preserves the general trend.

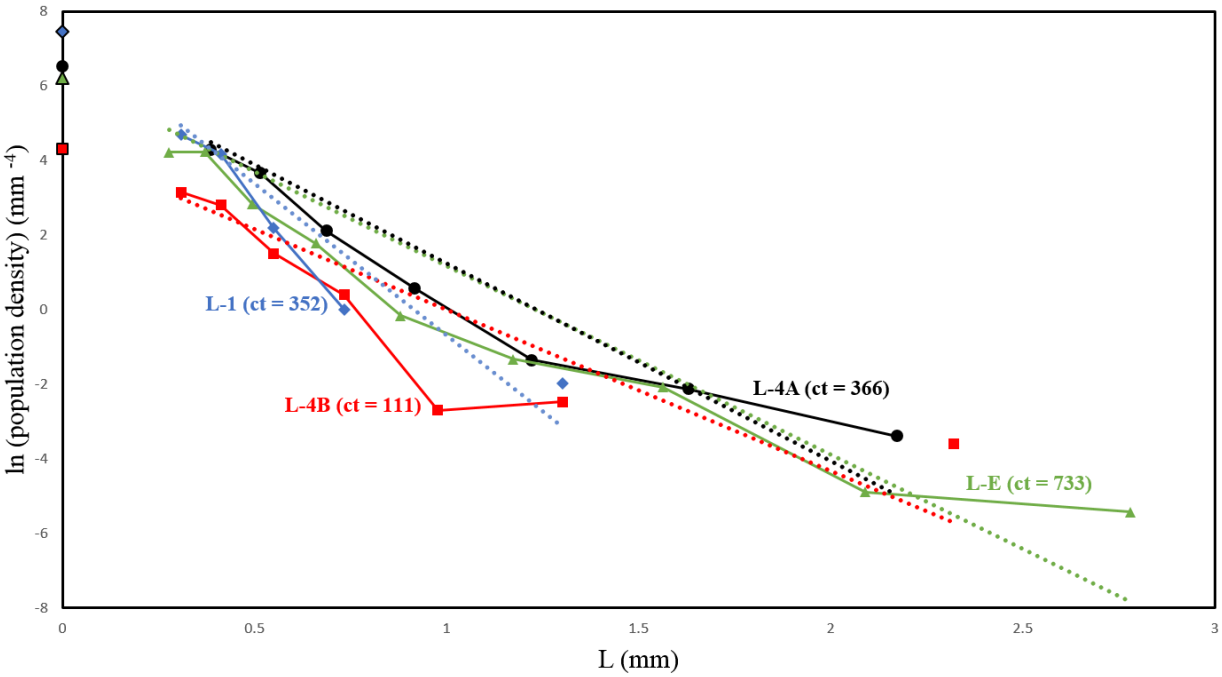


Fig. 3.4. CSDs based on manually traced phenocrysts only. Regressions for each curve are shown by the dotted lines of the same color. Projections to nucleation population densities for each regression are shown by matching colored markers on the y-axis.

extinction styles under a polarizing microscope help distinguish contiguous crystals), care should be taken when extracting nucleation densities from the y-axis in CSD plots by back-extrapolation. Volcanic CSDs can curve upward as a result of evolving cooling rates during crystallization, and so linearly back-extrapolation of regressions through CSD curves may only provide minimum nucleation population densities. Distances travelled by our samples range from an on-vent distance of ~0 km, to L-4B's estimated travel distance of ~3 km, to L-1's travel distance of ~9 km, and finally to L-E's distance of ~33 km. In all cases, the degree to which a specific sample represents a thermally-preserved flow (as through long-distance flows through large-diameter lava tubes) is indeed reflected in the final texture considering the entire distance travelled, but again, the effect of contiguity and natural cooling-induced fracturing on CSDs (as reflected by TIMA phase images) does affect the interpretation of residence times.

Aspect ratios vary over crystal size populations, and this idea is reinforced by the results shown in Figure 3.2. Assumptions of no preferred-orientation in samples is often invoked with non-flow volcanic samples. However, we noticed that in highly vesiculated samples a preferred flow alignment of plagioclase microlites can form in the exterior vesicle walls. This calls into question the effects of preferred crystal alignment in highly vesiculated samples on aspect ratio determination and on CSD plots. If highly vesiculated samples show increased preferred orientation along vesicle walls, then CSD analysis should be based on thin-section regions away from vesicles, if at all possible, as performed in our study. GM1 and GM2 crystal groundmass populations for all four samples, however, show similar aspect ratios and so the effects of crystal alignment along vesicle walls may be minimal.

Downturns at the smallest lengths (x-axis) for the phenocryst-based CSD (Fig. 3.4) is presumably due to insufficient crystal counts. This downturn causes skewing of regressions drawn through the whole-curve that force lower nucleation population densities. The choice of binning phenocryst populations in CSDCorrections (5, 6, 7 and 8 bins per decade) did not change the general shape of the curve but often produced varying degrees of turndowns at the smallest L-values. Downturns reinforce the idea that manually tracing crystals should extend past the 150 μm threshold when automated analysis is not available. In addition to the effects of insufficient crystal counts on nucleation population densities,

swallowtail microlites were observed. These two-pronged, V-shaped terminations on plagioclase are common during fast cooling and have been documented in the Laki basalts by Guilbaud et al. (2007) and were noticed in our samples. Depending on their prevalence, cut sections through swallowtail terminations could serve to increase the small-length population while simultaneously (and artificially) reducing the length of the main body of the crystal from which the swallowtails have generated. This apparent reduction of microlite body length may partially account for the behavior of the GM2 curve for sample L-4B in Figure 3.3. As CSDSlice and CSDCorrections assume simple polyhedral forms such as rectangles, the cut-sections of swallowtail forms require further investigation.

Crystal residence times based on regression lines through 1) phenocrysts only and through 2) GM1+GM2 show significant differences for samples L-4A and L-4B, up to 39% in the case of the latter. The residence times are directly related to the population-size densities of the groundmass. Relatedly, L-4B shows the greatest variation in nucleation densities between the two CSD approaches used here, by three orders of magnitude. Groundmass dominated textures suggest that a more rigorous approach is required to constrain crystallization kinetics of natural samples, and that manually tracing bimodal textures with an exceptionally fine groundmass may yield misleading CSD curves. Automated methods solve this by producing high-resolution images from which crystal lengths may be quickly extracted using freeware programs such as ImageJ.

### 3.8 Implications

The advantages of automated analysis in quickly producing multi-field phase images for length measurement extraction appear best suited for textures where crystal contiguity of a given phase is minimal, or ideally, non-existent. More crowded, multi-phase textures may still be examined with phase imaging as long as the presence of other phases can serve as spatial separators so that the effects of contiguity are decreased.

Groundmass-dominated natural volcanic samples, especially quickly-cooled ones, pose challenges by offering atypical crystal forms that CSDSlice and CSDCorrections cannot fully address. Quickly cooled natural samples also have inherent fracturing, and so length determination can be difficult

to resolve with phase-based images where fracture widths can create artificially inflated size populations. In both cases, further research is warranted. Modelling of anhedral crystal shapes will serve to constrain aspect ratios for accurate CSD interpretation.

TIMA images can assist in constraining the kinetic parameters of crystallization by providing maximum nucleation population densities. Here, we chose to emphasize a high scan resolution (2 μm) over increased thin section area. This tradeoff presented problems with forming smooth and continuous CSD curves at 8 bins-per-decade from samples with an insufficient number of phenocrysts in certain size ranges (for example, L-4B in Figs. 3.3 and 3.4). We would have benefitted from an increased area of analysis as this would have also stabilized the large-length (x-axis) portions of the CSD curves which in turn influence the interpretation of smaller, subsequent bins. However, this does not rule out the possibility that certain phenocryst populations may be absent or removed from ideal, open-system environments due to effects such as crystal settling or synneusis. It could be argued that during certain eruptive episodes, phenocryst populations were differentially entrained and therefore the coarser phenocrysts would not be expected to follow a theoretical, steady-state CSD curve. A larger phenocryst sample size than we provided would have been required to constrain this possibility.

In terms of our interpreted kinetic parameters using the two methods for obtaining length measurements, CSDs were also extracted from Laki samples by Neave et al. (2013, 2017). Similarities in CSD curves between our findings and Neave et al. (2017) suggest that late-stage degassing and decompression-induced increases in groundmass size populations created steep slopes at the smallest length values. This extreme slope behavior was demonstrated by Brugger and Hammer (2010) in a series of decompression experiments. Guilbaud et al. (2007), also working on the Laki system, concluded that a loss of water of ~1% created significant undercooling during degassing-on-eruption. This undercooling would have permitted a sudden occurrence of very fine groundmass production that would not have followed a linear trend with the rest of the CSD curve. Sample LAK04 from Neave et al. (2017) was located in a similar place as our L-4B. Their CSD was created using CSDSlice and CSDCorrections and show back-extrapolations from the CSD curve at approximately 0.15 mm. Their nucleation population

density (y-axis intersection) was ~ln (6) $mm^{-4}$ where ours was approaching ~ln (12) $mm^{-4}$ based on the trend of the GM2 population alone and ~ln (7.32) $mm^{-4}$ for the TR+AM method. This difference is likely due to our method of refining groundmass populations but also may be in part due to natural textural variations that are spatially controlled during the eruptions (i.e. no two textures are exactly similar).

For example, by combining kinetic information derived from CSD curves with geochemical characteristics as well as with first-order textural characteristics from polarizing microscopy (Fig. 3.5), a more complete crystallization history may be revealed. BSE imaging of plagioclase phenocrysts was performed to determine zoning behavior, a reflection of physiochemical processes that occur during crystallization (Figs. 3.6 and 3.7). The variation from $An_{68}$ to $An_{86}$ in plagioclase phenocrysts suggests the initial nucleation and growth environments for plagioclase phenocrysts varied significantly during crystallization histories. Certain flow events may have been relatively depleted in earlier-formed, more primitive plagioclase phenocrysts. For example, the flow designated by sample L-1 follows the flow represented by sample L-4B, and shows the lowest-anorthite cores in the early stages of the eruption. The low-An cores in L-1 may reflect a condition where deeper-seated, more anorthite rich-cores do not surface until a sufficient volume of discharge has occurred, forcing lower-depth phenocrysts upward. An extensive analysis of multiple zoned plagioclase phenocrysts across the eight Laki eruptive episodes are necessary to draw a more definitive conclusion.

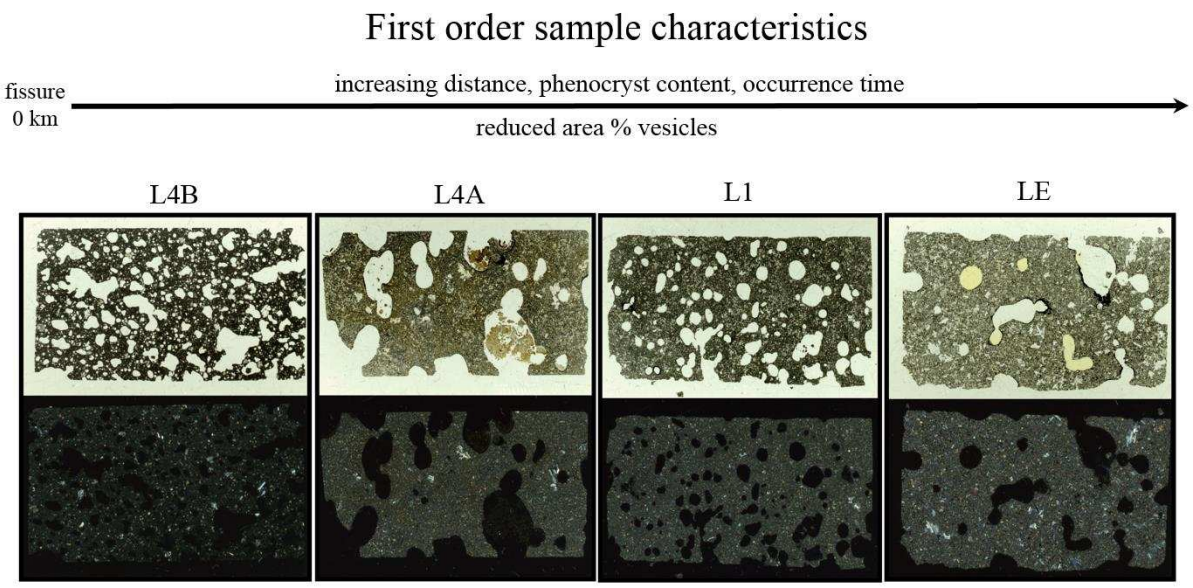


Fig. 3.5. First-order textural characteristics as suggested by polarized microscopy. Textural aspects vary with distance from the originating fissure in vesicle percent, date of occurrence, and phenocryst content.

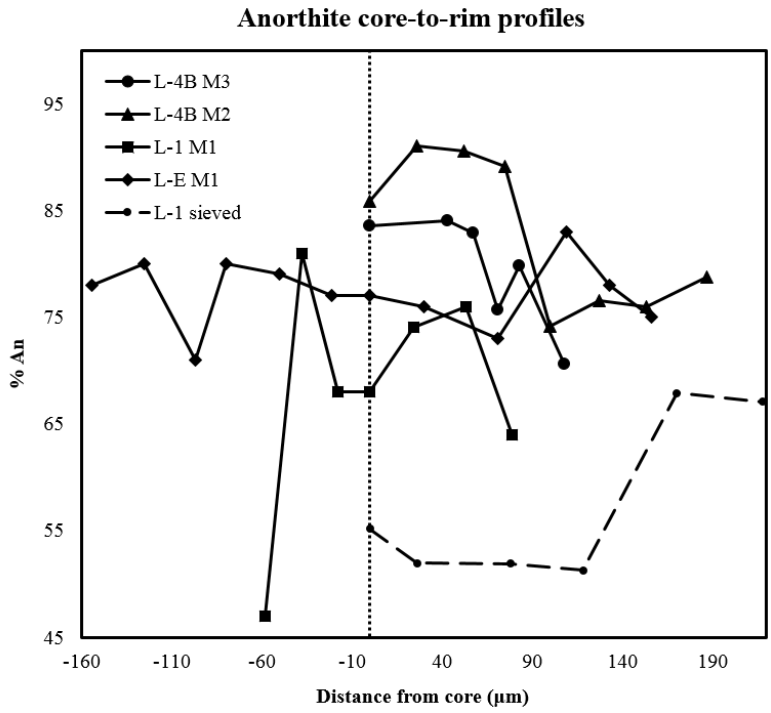


Fig. 3.6. Anorthite percents from four phenocrysts, plotted against distance from the core (or closest point to the core that was analyzed, reflected in Figure 6.8). The dotted line indicates 0 µm (the relative core position for each sample). The two curves that span across the vertical dotted line represent rim-core-rim analyses. Any errors are reflected by a maximum of ± 1.1 mole % Ca before anorthite calculation. Core anorthite contents vary and suggest different initial crystallization environments.

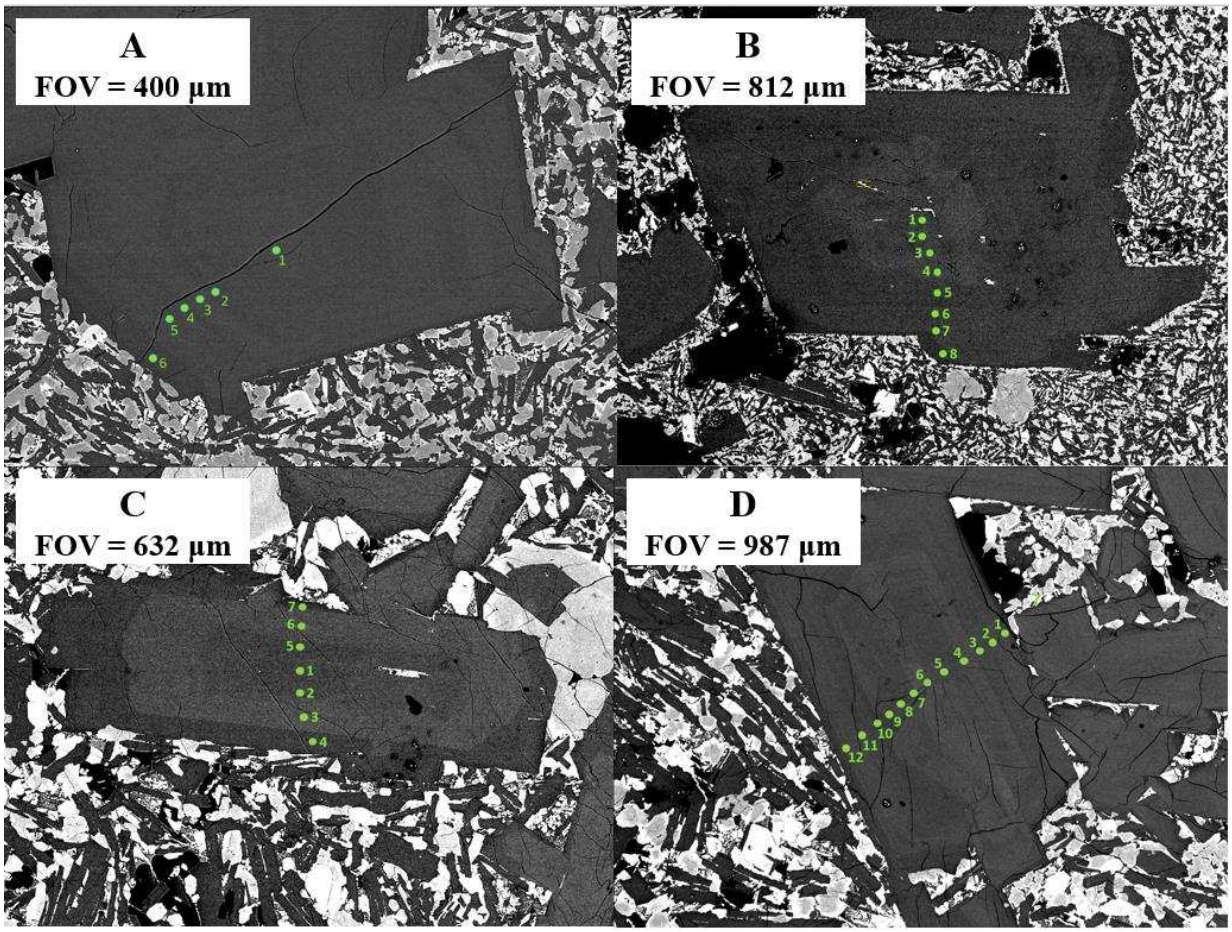


Fig. 3.7. Four zoned plagioclase phenocrysts from samples from L-4B (A, B), L-1 (C), and L-E (D). Green dots represent points of core-to-rim spot analyses for relative changes in anorthite (Ca/(Ca+Na+K)) using elemental mole percents. Numbered points are matched in Figure 6.9 core-to-rim anorthite percent plots.

# CHAPTER 4

## GENERAL CONCLUSIONS

Manual methods provide the most accurate lengths for crystal size distributions, with a minimum size-limit dictated by image resolution for very-fine groundmass. Linear CSDs reflect an open-system, steady-state environment. However, since most lavas show curved CSDs (or some type of curve kinking) and may undergo decompression crystallization at the end-stages of eruption, increases in undercooling are the most likely explanation for curved CSDs. Because of late-stage decompression-induced crystallization, linear trends CSD curves should not be expected, and therefore back-extrapolation based on lengths of manually-traced phenocrysts do not provide meaningful nucleation population densities. The exception to this appears to be strongly seriate textures where back-extrapolation provides similar kinetic information compared to that derived from TIMA images.

Automated analysis addresses problematic groundmass crystal population counts by utilizing geochemistry to produce high-resolution images which assist in removing user bias from measurements derived from manually traced images. However, samples must be carefully chosen and prepared, and the best methods must be determined by sample texture and composition. Crystal counts for plagioclase may be improved by using phase images after manipulation of compositional bins to best reflect population sizes, defining multiple, narrow anorthite bins. Electron backscatter diffraction shows the most promise in discerning crystal borders when contiguity is an issue or when polymorphs are present. However, scan times at high resolutions prevent this method from being practical, as cost is a factor. Scanning carefully selected areas from thin sections that represent the general texture of a sample should provide the necessary orientation data for stereological corrections that result in more accurate CSDs.

The Laki fissure eruptions serve as an analogue for small-scale flood basalt events. The mineralogy and geochemistry as well as the timeline of events are well-constrained across multiple research. Geochemistry and kinetics may be teased out of individual flows to characterize the evolution of an entire system. Here, crystal size distributions suggest that sudden decompression-induced undercooling caused steepening of CSD curves for all four samples. However, based on Passmore et al. (2012) and

Neave et al. (2013), variable crystal mush entrainment should also have assisted in creating curved CSDs for the Laki eruptions, but there were insufficient larger, zoned phenocryst counts to suggest this. A larger sample size is required to make a definitive analysis using crystal size distributions alone. Plagioclase phenocryst core-to-rim analysis shows that variable core anorthite contents suggest nucleation and growth origins in multiple melt environments. Taken together, plagioclase phenocryst zoning and curved CSDs hint at mixing processes, with crystal mush entrainment possibly triggered by earthquakes at the onset of the two-year volcano-tectonic event (Neave et al., 2017). Given the maximum distance traveled by flows was as much as 70 km (not accounting for changes in elevation) and that the minimum surface transport rate was ~2 km/day (Neave et al., 2017), the June 24$^{th}$ event (episode IV) could have taken as long as 35 days to texturally evolve (assuming thermally efficient transport to the base of the flow in lava tubes, as reported by Guilbaud et al. (2007)). The complexity of thermally efficient flow conditions is increased by the variable depth of the two river gorges in which the bulk of the lava traveled. Constraining the dynamics of large-volume flows serves as analogue for similar processes that occurred on Mars and Venus.

REFERENCES CITED

Bindeman, I., Sigmarsson, O. and Eiler, J. (2006) Time constraints on the origin of large volume basalts derived from O-isotopes and trace element mineral zoning and U-series disequilibria in the Laki and Grímsvötn volcanic system. Earth and Planetary Science Letter, 245, 245-259.

Brugger, C.R. and Hammer, J.E. (2010) Crystal size distribution analysis of plagioclase in experimentally decompressed hydrous rhyodacite magma. Earth and Planetary Letters, 300, 246-254.

Brugger, C.R. and Hammer, J.E. (2015) Prevalence of growth twins among anhedral plagioclase microlites. American Mineralogist, 100, 385-395.

Cashman, K.V. and Marsh, B.D. (1988) Crystal size distribution (CSD) in rocks and the kinetics and dynamics of crystallization II: Makaopuhi lava lake. Contributions to Mineralogy and Petrology, 99, 292-305.

Cashman, K.V. (1990) Textural constraints on the kinetics of crystallization of igneous rock. Reviews in Mineralogy, 24, 259-314.

Cashman, K.V. (1993) Relationship between plagioclase crystallization and cooling rate in basaltic melts. Contributions to Mineralogy and Petrology, 113, 126-142.

Castro, J.M., Cashman, K.V., and Manga, M. (2003) A technique for measuring 3D crystal size distributions of prismatic microlites in obsidian. American Mineralogist, 88, 1230-1240.

Cheng, L., Costa, F. and Carniel, R. (2017) Unraveling the presence of multiple plagioclase populations and identification of representative two-dimensional sections using a statistical and numerical approach. American Mineralogist, 102, 1894-1905.

Gottlieb, P., Wilkie, G., Sutherland, D., Ho-tun, E. Suthers, S., Perera, K., Jenkins, B., Spencer, S., Butcher, A.R., and Rayner, J. (2000) Using quantitative electron microscopy for process mineralogy applications. Journal of the Minerals, Metals and Materials Society, 52, 24-25.

Gu, Y. (2003) Automated Scanning Electron Microscope Based Mineral Liberation Analysis - An Introduction to JKMRC/FEI Mineral Liberation Analyser. Journal of Minerals and Materials Characterization and Engineering, 2, 33-41.

Gu, Y., Schouwstra, R.P., and Rule, C. (2014) The value of automated mineralogy. Minerals Engineering, 58, 100-103.

Guilbaud, M.N., Blake, S., Thordarson, T. and Self, S. (2007) Role of syn-eruptive cooling and degassing on textures of lavas from the AD 1783-1784 Laki eruption, south Iceland. Journal of Petrology, 48, 1265-1294.

Hersum, T.G. and Marsh, B.D. (2007) Igneous textures: On the kinetics behind the words. Elements, 3, 247-252.

Higgins, M. (2000) Measurement of crystal size distributions. American Mineralogist, 85, 1105-1116.

Higgins, M. (2006) Quantitative Textural Measurements in Igneous and Metamorphic Petrology. Cambridge University Press, Cambridge, 276 pp.

Kirkpatrick, R.J. (1977) Nucleation and growth of plagioclase, Makaopuhi and Alae lava lakes, Kilauea volcano, Hawaii. Geological Society of America Bulletin, 88, 78-84.

Mainprice, D., Bachmann, F., Hielscher, R. and Schaeben, H. (2015) Descriptive tools for the analysis of texture projects with large datasets using MTEX: strength, symmetry and components. Geological Society of London, Special Publications, 409, 251-271.

Marsh, B.D. (1988) Crystal size distribution (CSD) in rocks and the kinetics and dynamics of crystallization I: Theory. Contributions to Mineralogy and Petrology, 99, 277-291.

Marsh, B.D. (1998) On the interpretation of crystal size distributions in magmatic systems. Journal of Petrology, 39, 553-599.

Mock, A. and Jerram, D.A. (2005) Crystal size distributions (CSD) in three dimensions: Insights from the 3-D reconstruction of a highly porphyritic rhyolite. Journal of Petrology, 46, 1525-1541.

Morgan, D.J. and Jerram, D.A. (2006) On estimating crystal shape for crystal size distribution analysis. Journal of Volcanology and Geothermal Research, 154, 1-7.

Neave, D., Buisman, I., and Maclennan, J. (2017) Continuous mush disaggregation during the long-lasting Laki fissure eruption, Iceland. American Mineralogist, 112, 2007-2021.

Neave, D., Passmore, E., Maclennan, J., Fitton, G. and Thordarson, T. (2013) Crystal-melt relationships and the record of deep mixing and crystallization in the AD 1783 Laki eruption, Iceland. Journal of Petrology, 54, 1661-1690.

Passmore, E., Maclennan, J., Fitton, G. and Thordarson, T. (2012) Mush disaggregation in basaltic magma chambers: evidence from the ad 1783 Laki eruption. Journal of Petrology, 53, 2593-2623.

Prior, D., Boyle, A.P., Brenker, F., Cheadle, M.C., Day, A., Lopez, G., Peruzzo, L., Potts, G.J., Reddy, S., Spiess, R., Timms, N., Trimby, P., Wheeler, J. and Zetterström, L. (1999). The application of backscatter diffraction and orientation contrast imaging in the SEM to textural problems in rocks. American Mineralogist, 84, 1741-1759.

Randolph, A.D., and Larson, M.A. (1971) Theory of particulate processes. Academic Press, New York, 251 pp.

Schneider, C. A., Rasband, W. S. and Eliceiri, K. W. (2012) NIH Image to ImageJ: 25 years of image analysis. Nature Methods, 9, 671-675.

Sigmarsson, O., Condomines, M., Grönvold, K., and Thordarson, T. (1991) Extreme magma homogeneity in the 1783–84 Lakagígar Eruption: Origin of a large volume of evolved basalt in Iceland. Geophysical Research Letters, 18, 2229-2232.

Skemer, P., Katayama, I., Jiang, Z. and Karato, S. (2005) The misorientation index: Development of a new method for calculating the strength of lattice-preferred orientation. Tectonophysics, 411, 157-167.

Sutherland, D. (2007) Estimation of mineral grain size using automated mineralogy. Minerals Engineering, 20, 452-460.

Thordarson, T. and Self, S. (1993) The Laki (Skaftár Fires) and Grímsvötn eruptions in 1783-1785. Bulletin of Volcanology, 55, 233-263.

Xu, C., Zhao, S-R., Li, C. and He, X. (2016) Plagioclase twins in a basalt: an electron backscatter diffraction study. Journal of Applied Crystallography, 49, 2145-2154.

APPENDIX A

THIN SECTION IMAGES

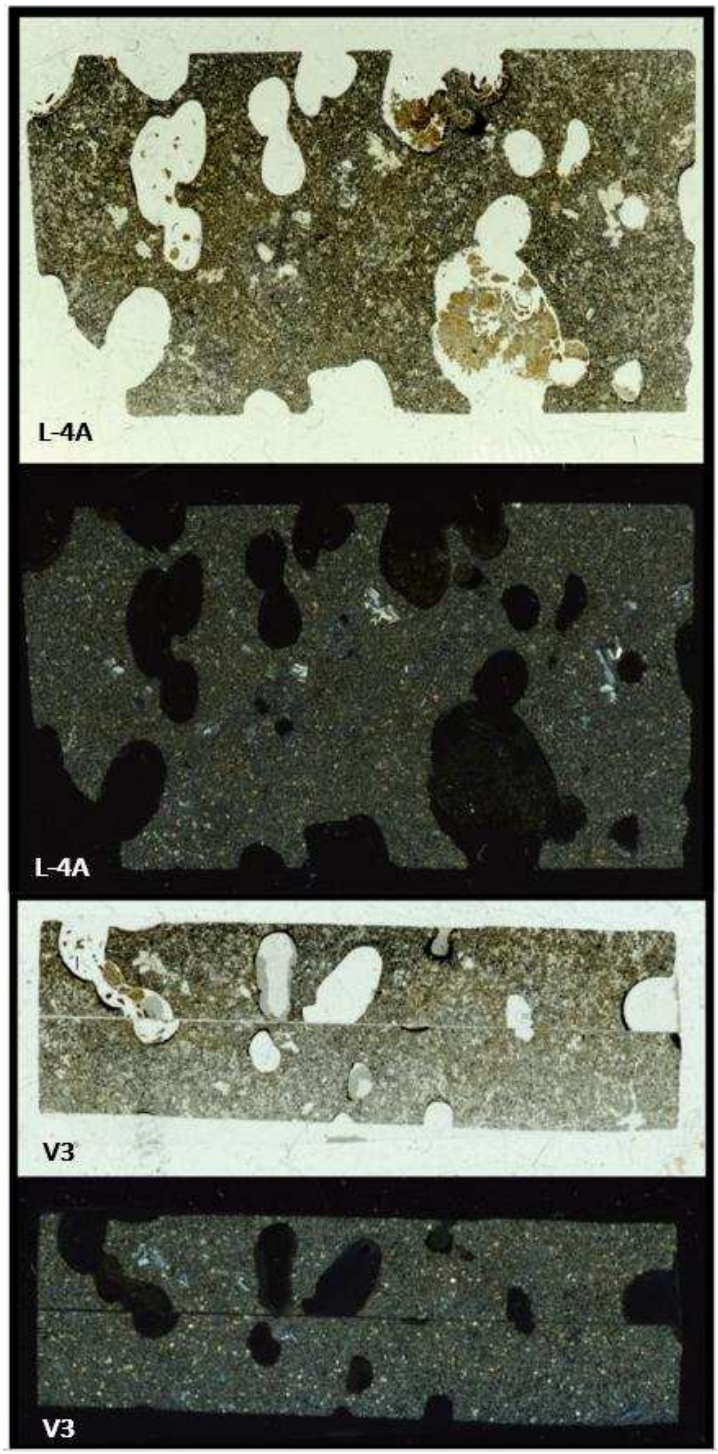


Figure A.1. Full thin section scans of sample L-4A under plane polarized light (light images) and cross polarized light (dark images). V3 represents orthogonal cuts.

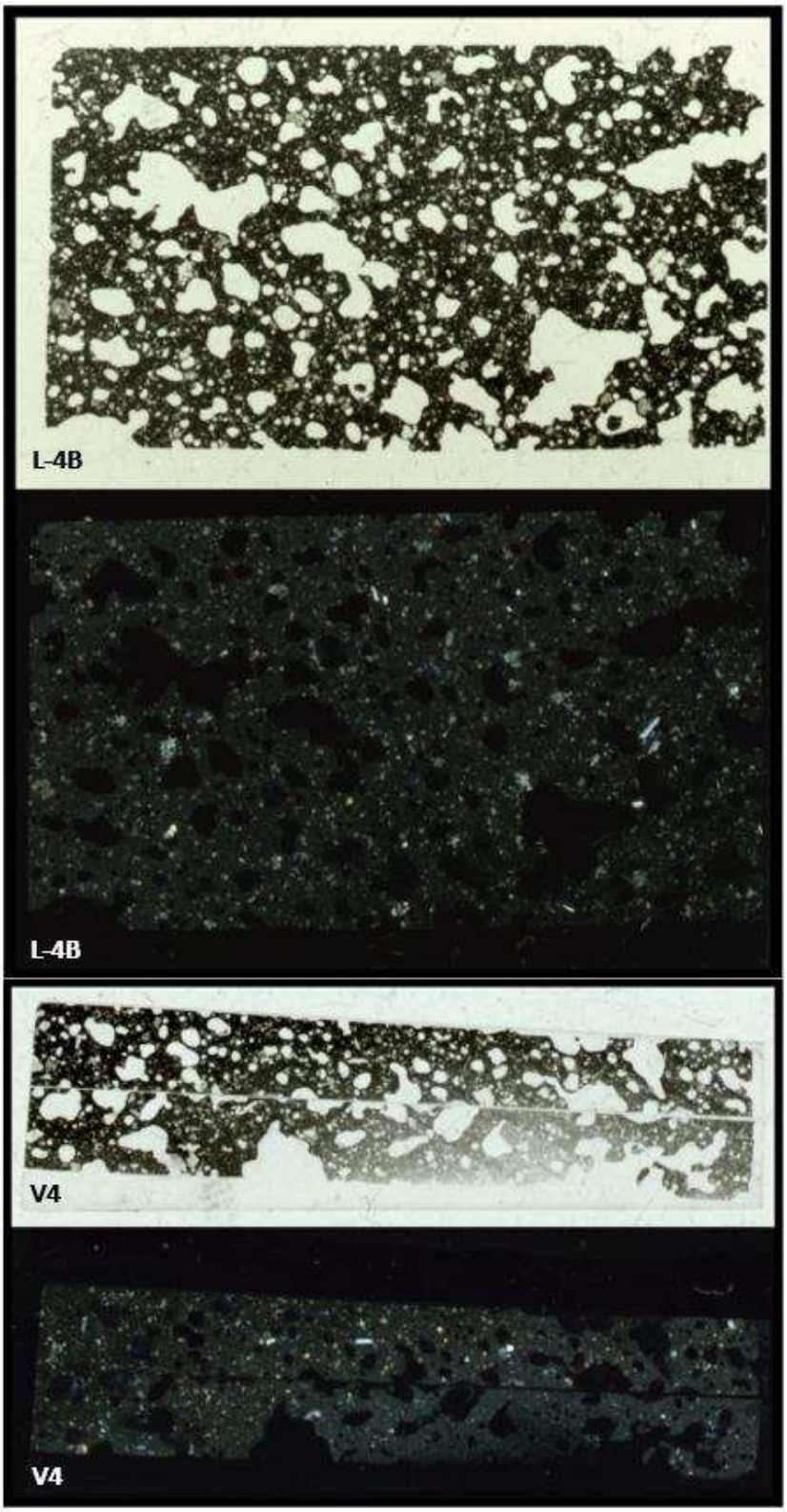


Figure A.2. Full thin section scans of sample L-4B under plane polarized light (light images) and cross polarized light (dark images). V4 represents orthogonal cuts.

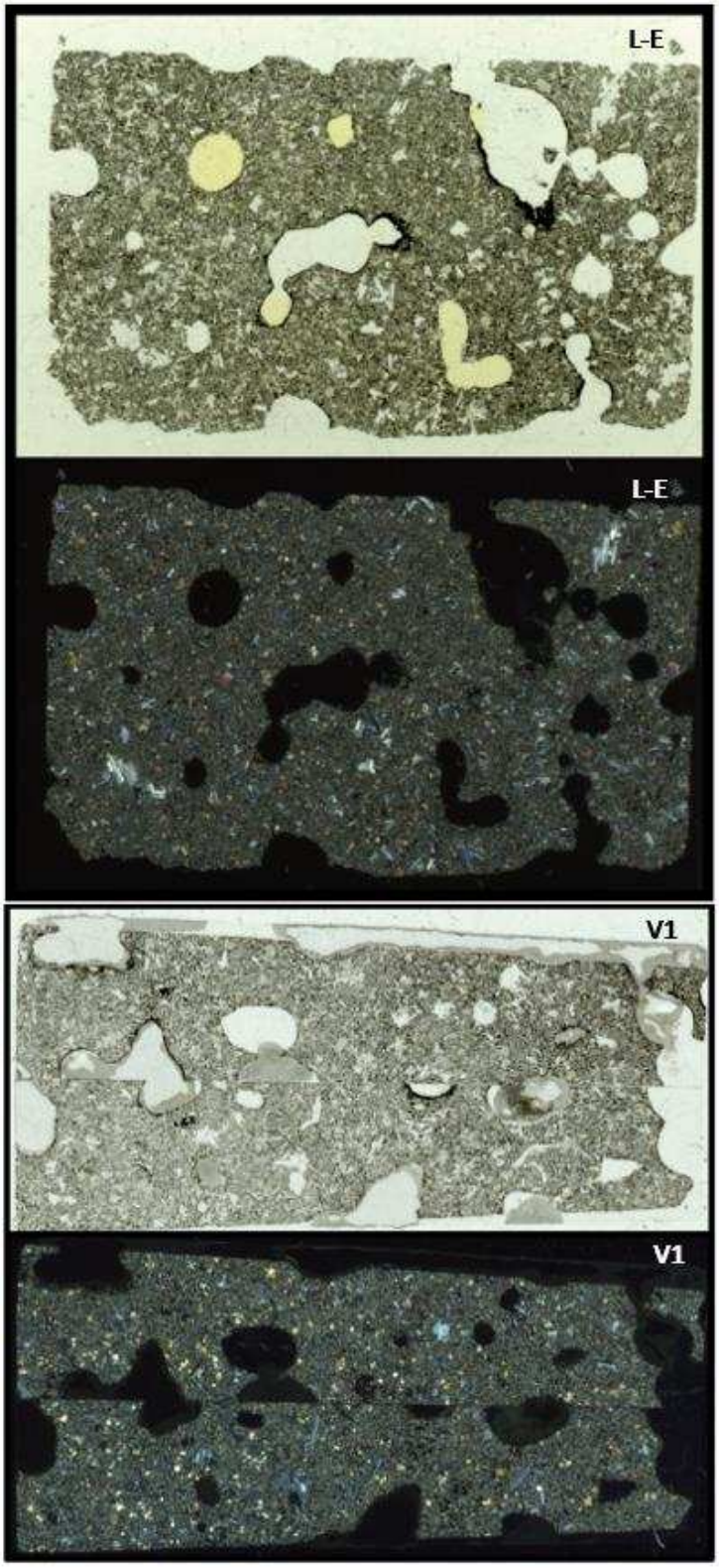


Figure A.3. Full thin section scans of sample L-E under plane polarized light (light images) and cross polarized light (dark images). V1 represents orthogonal cuts.

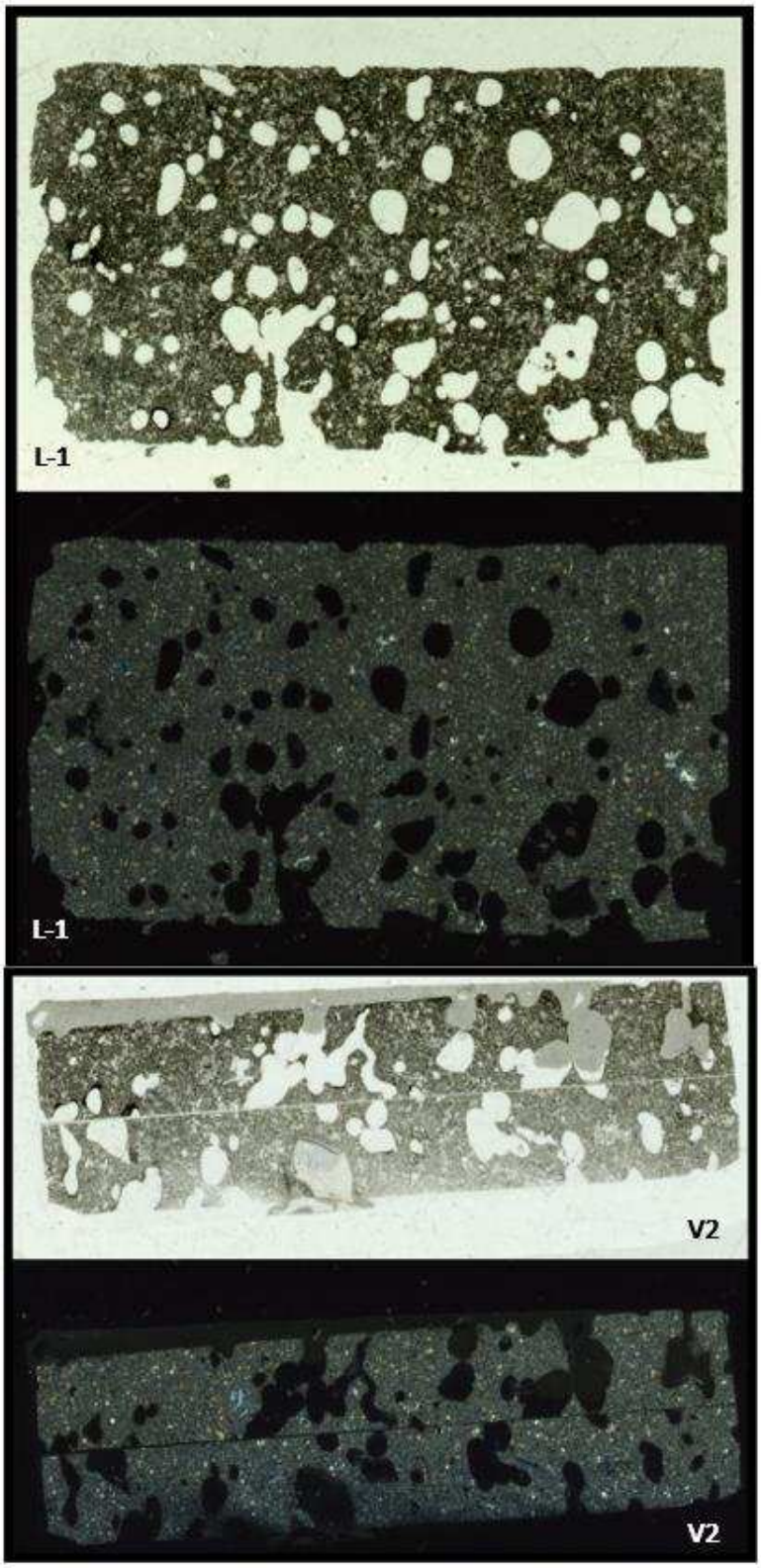


Figure A.4. Full thin section scans of sample L-4A under plane polarized light (light images) and cross polarized light (dark images). V2 represents orthogonal cuts.

APPENDIX B

MTEXT SCRIPT

```
close all
clear all

%% Import Script for EBSD Data
%
% This script was automatically created by the import wizard. You should
% run the whoole script or parts of it in order to import your data. There
% is no problem in making any changes to this script.

% Specify Crystal and Specimen Symmetries

% crystal symmetry
CS = {...
  'notIndexed',...
  crystalSymmetry('-1', [8.1797 12.8748 14.1721], [93.13,115.89,91.24]*degree, 'X||a*', 'Z||c', 'mineral',
'Anorthite', 'color', 'blue')};

% plotting convention
setMTEXpref('xAxisDirection','north');
setMTEXpref('zAxisDirection','outOfPlane');

% Specify File Names

% path to files THIS WILL CHANGE FROM COMPUTER TO COMPUTER
pname = 'C:\Users\Julianskye\Documents\MATLAB\mtex-4.5.1\Samples\Kim A. Cone';

% which files to be imported
fname = [pname '\STITCHED_LE_RI_5570_NR.cpr'];

% Import the Data

% create an EBSD variable containing the data
ebsd = loadEBSD(fname,CS,'interface','crc',...
  'convertEuler2SpatialReferenceFrame');


diary('STITCHED_LE_RI_5570_NR raw EBSD map properties.txt')
ebsd
diary off

save('STITCHED_LE_RI_5570_NR_ebsd','ebsd');

fig_resolution = [0 0 1200 700];

%% Calculating Plagioclase boundaries (1 degrees)
load 'STITCHED_LE_RI_5570_NR_ebsd.mat'
fig_resolution = [0 0 1200 700];
```

```
% perform grain reconstruction, the '1*degree' terms in this section are
% what determines the threshold for a high-angle grain boundary
[grains_pl, ebsd.grainId] = calcGrains(ebsd,'angle',1*degree,'boundary','tight');
%then reassign the unindexed areas to not be filled in
notIndexed = grains_pl('notIndexed');
% the "not indexed grains" we want to remove
toRemove = notIndexed(notIndexed.grainSize ./ notIndexed.boundarySize<0.8);
% now we remove the corresponding EBSD measurements
ebsd(toRemove) = [];
% remove all grains with less than 3 measurements
large_grains = grains_pl(grains_pl.grainSize >= 3);
%// perform new grain reconstruction
ebsd_cleaned_pl = ebsd(large_grains);
[grains_cleaned, ebsd_cleaned_pl.grainId, ebsd_cleaned_pl.mis2mean] =
calcGrains(ebsd_cleaned_pl,'angle',1*degree,'boundary','tight');
% And now we can get rid of some of that nasty staircasing effect on the grain boundaries
grains_smoothed_pl = smooth(grains_cleaned);
% Fill the zero solutions using the calculated grains
ebsd_filled_pl = fill(ebsd_cleaned_pl);

% Some handy analyses that show up in the command window and are saved to a
% text file (if the text file already exists, the new stuff is appended
diary('STITCHED_LE_RI_5570_NR EBSD map properties_pl.txt')
'NEW ENTRY NEW ENTRY NEW ENTRY NEW ENTRY NEW ENTRY NEW ENTRY NEW
ENTRY NEW ENTRY NEW ENTRY NEW ENTRY'
clock
% Basic info on phases (modal %, symmetries, # of orientations per phase)
ebsd
ebsd_cleaned_pl
ebsd_filled_pl
% Info on reconstructed grains
grains_pl
grains_smoothed_pl
diary off

% save the variables
save('STITCHED_LE_RI_5570_NR_ebsd_cleaned_pl','ebsd_cleaned_pl');
save('STITCHED_LE_RI_5570_NR_ebsd_filled_pl','ebsd_filled_pl');
save('STITCHED_LE_RI_5570_NR_grains_pl','grains_pl');
save('STITCHED_LE_RI_5570_NR_grains_smoothed_pl','grains_smoothed_pl');
%}

% General reference map plots

figure
[~,mP] = plot(ebsd);
mP.micronBar.visible = 'off'
legend off;
set(gcf,'Position',fig_resolution)
export_fig 'STITCHED_LE_RI_5570_NR ebsd.png' -transparent
figure
```

```
[~,mP] = plot(ebsd_filled_pl);
mP.micronBar.visible = 'off'
legend off;
set(gcf,'Position',fig_resolution)
export_fig 'STITCHED_LE_RI_5570_NR ebsd_filled.png' -transparent

legend on
legend('Location','eastoutside')
legend('boxoff')
export_fig 'STITCHED_LE_RI_5570_NR ebsd legend.png' -native

figure
[~,mP] = plot(grains_smoothed_pl);
mP.micronBar.visible = 'off'
legend('hide')
set(gcf,'Position',fig_resolution)
export_fig 'STITCHED_LE_RI_5570_NR grains_smoothed_pl5.png' -transparent

%% Starting by loading variables instead of re-importing
% if you've already run the above two sections and don't want to spend time re-importing and re-
calculating the grains, you can
% comment out those two sections and start here by loading the variables.

% plotting convention
setMTEXpref('xAxisDirection','north');
setMTEXpref('zAxisDirection','outOfPlane');
setMTEXpref('defaultColorMap',hot)

%{
load('STITCHED_LE_RI_5570_NR_ebsd_cleaned_pl','ebsd_cleaned_pl');
load('STITCHED_LE_RI_5570_NR_ebsd_filled_pl','ebsd_filled_pl');
load('STITCHED_LE_RI_5570_NR_grains_smoothed_pl','grains_smoothed_pl');
%}

fig_resolution = [0 0 1200 700];

%% Grain boundary misorientations

load 'STITCHED_LE_RI_5570_NR_grains_smoothed_pl.mat'

% Use boundary('Plagioclase','Plagioclase') to chose only Plagioclase-Plagioclase boundaries
gB = grains_smoothed_pl.boundary.reorder;
gB_PlPl = gB('Anorthite','Anorthite');

% specifying the crystal symmmetry (this is also embedded in the 'ebsd'
% variable during import, but it can be helpful to define it as an individual
% variable
CS = crystalSymmetry('-1', [8.1797 12.8748 14.1721], [93.13,115.89,91.24]*degree, 'X||a*', 'Z||c');

% make a quick inverse pole figure to see if there are any super-obvious trends in
% grain boundary misorientations, this is less helpful in triclinic systems
```

```
%{
figure
plotAngleDistribution(gB_PlPl.misorientation)

figure
plotAxisDistribution(gB_PlPl.misorientation,'contour')
%}

% Twinning definitions

Albite_twinning = orientation('axis',Miller(0,1,0,CS,'hkl'),'angle',180*degree,CS,CS);
Carlsbad_twinning = orientation('axis',Miller(0,0,1,CS,'uvw'),'angle',180*degree,CS,CS);
AC_twinning = orientation('axis',Miller(1,0,0,CS,'pole'),'angle',180*degree,CS,CS);
Pericline_twinning = orientation('axis',Miller(0,1,0,CS,'uvw'),'angle',180*degree,CS,CS);
Ala_twinning = orientation('axis',Miller(1,0,0,CS,'uvw'),'angle',180*degree,CS,CS);
Manebach_twinning = orientation('axis',Miller(0,0,1,CS,'pole'),'angle',180*degree,CS,CS);
Baveno_twinning = orientation('axis',Miller(0,2,1,CS,'pole'),'angle',180*degree,CS,CS);
AlbiteAla_twinning = orientation('axis',Miller(0,0,1,CS,'pole'),'angle',180*degree,CS,CS);
Prism110_twinning = orientation('axis',Miller(1,1,0,CS,'pole'),'angle',180*degree,CS,CS);
Prism1_10_twinning = orientation('axis',Miller(1,-1,0,CS,'pole'),'angle',180*degree,CS,CS);
Prism130_twinning = orientation('axis',Miller(1,3,0,CS,'pole'),'angle',180*degree,CS,CS);
Prism1_30_twinning = orientation('axis',Miller(1,-3,0,CS,'pole'),'angle',180*degree,CS,CS);

% restrict to twinnings with threshold 5 degree and have MTEX use the
% definitions to start identifying plag-plag boundaries with those specific
% twinning relationships

isTwinning_Albite = angle(gB_PlPl.misorientation,Albite_twinning) < 5*degree;
Albite_twin_Boundary = gB_PlPl(isTwinning_Albite);

isTwinning_Carlsbad = angle(gB_PlPl.misorientation,Carlsbad_twinning) < 5*degree;
Carlsbad_twin_Boundary = gB_PlPl(isTwinning_Carlsbad);

isTwinning_AC = angle(gB_PlPl.misorientation,AC_twinning) < 5*degree;
AC_twin_Boundary = gB_PlPl(isTwinning_AC);

isTwinning_Pericline = angle(gB_PlPl.misorientation,Pericline_twinning) < 5*degree;
Pericline_twin_Boundary = gB_PlPl(isTwinning_Pericline);

isTwinning_Ala = angle(gB_PlPl.misorientation,Ala_twinning) < 5*degree;
Ala_twin_Boundary = gB_PlPl(isTwinning_Ala);

isTwinning_Manebach = angle(gB_PlPl.misorientation,Manebach_twinning) < 5*degree;
Manebach_twin_Boundary = gB_PlPl(isTwinning_Manebach);

isTwinning_Baveno = angle(gB_PlPl.misorientation,Baveno_twinning) < 5*degree;
Baveno_twin_Boundary = gB_PlPl(isTwinning_Baveno);

isTwinning_AlbiteAla = angle(gB_PlPl.misorientation,AlbiteAla_twinning) < 5*degree;
AlbiteAla_twin_Boundary = gB_PlPl(isTwinning_AlbiteAla);
```

```
isTwinning_Prism110 = angle(gB_PlPl.misorientation,Prism110_twinning) < 5*degree;
Prism110_twin_Boundary = gB_PlPl(isTwinning_Prism110);

isTwinning_Prism1_10 = angle(gB_PlPl.misorientation,Prism1_10_twinning) < 5*degree;
Prism1_10_twin_Boundary = gB_PlPl(isTwinning_Prism1_10);

isTwinning_Prism130 = angle(gB_PlPl.misorientation,Prism130_twinning) < 5*degree;
Prism130_twin_Boundary = gB_PlPl(isTwinning_Prism130);

isTwinning_Prism1_30 = angle(gB_PlPl.misorientation,Prism1_30_twinning) < 5*degree;
Prism1_30_twin_Boundary = gB_PlPl(isTwinning_Prism1_30);

% Make a quick command-line summary of the twin proportions in the map,
% helpful so that you can only plot the ones that occur in meaninful
% quantities in the next bit
%{
diary('STITCHED_LE_RI_5570_NR twin boundary proportions.txt')
Albite = 100*length(Albite_twin_Boundary)/length(gB_PlPl)
Carlsbad = 100*length(Carlsbad_twin_Boundary)/length(gB_PlPl)
AC = 100*length(AC_twin_Boundary)/length(gB_PlPl)
Pericline = 100*length(Pericline_twin_Boundary)/length(gB_PlPl)
Ala = 100*length(Ala_twin_Boundary)/length(gB_PlPl)
Manebach = 100*length(Manebach_twin_Boundary)/length(gB_PlPl)
Baveno = 100*length(Baveno_twin_Boundary)/length(gB_PlPl)
AlbiteAla = 100*length(AlbiteAla_twin_Boundary)/length(gB_PlPl)
Prism110 = 100*length(Prism110_twin_Boundary)/length(gB_PlPl)
Prism1_10 = 100*length(Prism1_10_twin_Boundary)/length(gB_PlPl)
Prism130 = 100*length(Prism130_twin_Boundary)/length(gB_PlPl)
Prism1_30 = 100*length(Prism1_30_twin_Boundary)/length(gB_PlPl)
diary off
%}

% plot the twinning boundaries as overlays onto a plot of the grains
% colorized by mean average orientation
%{

plot(grains_smoothed_pl('Anorthite'),grains_smoothed_pl('Anorthite').meanOrientation)
%plot(ebsd('indexed'),ebsd('indexed').orientations)
hold on
plot(Albite_twin_Boundary,'linecolor','red','linewidth',2,'displayName','Albite twin boundary')
plot(Carlsbad_twin_Boundary,'linecolor','green','linewidth',2,'displayName','Carlsbad twin boundary')
plot(AC_twin_Boundary,'linecolor','blue','linewidth',2,'displayName','AC twin boundary')
plot(Pericline_twin_Boundary,'linecolor','cyan','linewidth',2,'displayName','Pericline twin boundary')
hold off
set(gcf,'Position',fig_resolution)
export_fig 'STITCHED_LE_RI_5570_NR all major twin boundaries.png' -transparent
%}

%}
```

```
%% Create the new grain set by ignorning the identified twin boundaries
load 'STITCHED_LE_RI_5570_NR_ebsd_filled_pl.mat'
load 'STITCHED_LE_RI_5570_NR_grains_smoothed_pl.mat'

% In this section, you have to merge the twin boundaries one at a time,
% which means you also have to re-calculate which remaining boundaries are
% twin boundaries. It's a bit redundant to the section above, but seems to
% work and doesn't take TOO long.

%

[mergedGrains,parentId] = merge(grains_smoothed_pl,Albite_twin_Boundary,'calcMeanOrientation');

gB = mergedGrains.boundary.reorder;
gB_PlPl = gB('Anorthite','Anorthite');
isTwinning_Carlsbad = angle(gB_PlPl.misorientation,Carlsbad_twinning) < 5*degree;
Carlsbad_twin_Boundary = gB_PlPl(isTwinning_Carlsbad);
[mergedGrains,parentId] = merge(mergedGrains,Carlsbad_twin_Boundary,'calcMeanOrientation');

gB = mergedGrains.boundary.reorder;
gB_PlPl = gB('Anorthite','Anorthite');
isTwinning_AC = angle(gB_PlPl.misorientation,AC_twinning) < 5*degree;
AC_twin_Boundary = gB_PlPl(isTwinning_AC);
[mergedGrains,parentId] = merge(mergedGrains,AC_twin_Boundary,'calcMeanOrientation');

gB = mergedGrains.boundary.reorder;
gB_PlPl = gB('Anorthite','Anorthite');
isTwinning_Pericline = angle(gB_PlPl.misorientation,Pericline_twinning) < 5*degree;
Pericline_twin_Boundary = gB_PlPl(isTwinning_Pericline);
[mergedGrains,parentId] = merge(mergedGrains,Pericline_twin_Boundary,'calcMeanOrientation');

gB = mergedGrains.boundary.reorder;
gB_PlPl = gB('Anorthite','Anorthite');
isTwinning_Ala = angle(gB_PlPl.misorientation,Ala_twinning) < 5*degree;
Ala_twin_Boundary = gB_PlPl(isTwinning_Ala);
[mergedGrains,parentId] = merge(mergedGrains,Ala_twin_Boundary,'calcMeanOrientation');

gB = mergedGrains.boundary.reorder;
gB_PlPl = gB('Anorthite','Anorthite');
isTwinning_Manebach = angle(gB_PlPl.misorientation,Manebach_twinning) < 5*degree;
Manebach_twin_Boundary = gB_PlPl(isTwinning_Manebach);
[mergedGrains,parentId] = merge(mergedGrains,Manebach_twin_Boundary,'calcMeanOrientation');

gB = mergedGrains.boundary.reorder;
gB_PlPl = gB('Anorthite','Anorthite');
isTwinning_Baveno = angle(gB_PlPl.misorientation,Baveno_twinning) < 5*degree;
Baveno_twin_Boundary = gB_PlPl(isTwinning_Baveno);
[mergedGrains,parentId] = merge(mergedGrains,Baveno_twin_Boundary,'calcMeanOrientation');

gB = mergedGrains.boundary.reorder;
gB_PlPl = gB('Anorthite','Anorthite');
```

```
isTwinning_AlbiteAla = angle(gB_PlPl.misorientation,AlbiteAla_twinning) < 5*degree;
AlbiteAla_twin_Boundary = gB_PlPl(isTwinning_AlbiteAla);
[mergedGrains,parentId] = merge(mergedGrains,AlbiteAla_twin_Boundary,'calcMeanOrientation');

gB = mergedGrains.boundary.reorder;
gB_PlPl = gB('Anorthite','Anorthite');
isTwinning_Prism110 = angle(gB_PlPl.misorientation,Prism110_twinning) < 5*degree;
Prism110_twin_Boundary = gB_PlPl(isTwinning_Prism110);
[mergedGrains,parentId] = merge(mergedGrains,Prism110_twin_Boundary,'calcMeanOrientation');

gB = mergedGrains.boundary.reorder;
gB_PlPl = gB('Anorthite','Anorthite');
isTwinning_Prism1_10 = angle(gB_PlPl.misorientation,Prism1_10_twinning) < 5*degree;
Prism1_10_twin_Boundary = gB_PlPl(isTwinning_Prism1_10);
[mergedGrains,parentId] = merge(mergedGrains,Prism1_10_twin_Boundary,'calcMeanOrientation');

gB = mergedGrains.boundary.reorder;
gB_PlPl = gB('Anorthite','Anorthite');
isTwinning_Prism130 = angle(gB_PlPl.misorientation,Prism130_twinning) < 5*degree;
Prism130_twin_Boundary = gB_PlPl(isTwinning_Prism130);
[mergedGrains,parentId] = merge(mergedGrains,Prism130_twin_Boundary,'calcMeanOrientation');

gB = mergedGrains.boundary.reorder;
gB_PlPl = gB('Anorthite','Anorthite');
isTwinning_Prism1_30 = angle(gB_PlPl.misorientation,Prism1_30_twinning) < 5*degree;
Prism1_30_twin_Boundary = gB_PlPl(isTwinning_Prism1_30);
[mergedGrains,parentId] = merge(mergedGrains,Prism1_30_twin_Boundary,'calcMeanOrientation');

%}
%{
figure
plot(ebsd_filled_pl('Anorthite'),ebsd_filled_pl('Anorthite').orientations)
hold on
%plot(gB_MgMg,angle(gB_MgMg.misorientation,twinning),'linewidth',4)
plot(mergedGrains.boundary,'linecolor','k','linewidth',1,'displayName','merged grains')
hold off
set(gcf,'Position',fig_resolution)
export_fig 'STITCHED_LE_RI_5570_NR all Twins Merged.png' -transparent
%}
save('STITCHED_LE_RI_5570_NR_merged_grains','mergedGrains');
%
%% Comparison between pre-merged (all twins their own grain) and merged
% this section generates an orientation distribution function for groups of
% grains and plots them as contoured pole figures

% calculate the orientation distribution function using a full width at
% half-maximum calculated using a Kullback-Leibler optimization scheme
% (more mathematically sound that just using '10 degrees' like almost
% everyone else who does EBSD
%{
psi_beforetwins = calcKernel(grains_smoothed_pl('Anorthite').meanOrientation)
```

```
psi_merged = calcKernel(mergedGrains('Anorthite').meanOrientation)

odfbeforetwins = calcODF(grains_smoothed_pl('Anorthite').meanOrientation,psi_beforetwins);
odfmerged = calcODF(mergedGrains('Anorthite').meanOrientation,psi_merged);

save('STITCHED_LE_RI_5570_NR_odf','odfbeforetwins','odfmerged');


% explictly define the crystallographic planes and axes that you're
% interested in seeing plotted

%Anorthite_beforetwins
cs_Anorthite_beforetwins = ebsd_filled_pl('Anorthite').CS;
h_Anorthite_beforetwins=[Miller(0,0,1,cs_Anorthite_beforetwins),
Miller(1,0,0,cs_Anorthite_beforetwins),Miller(1,1,1,cs_Anorthite_beforetwins),Miller(1,1,0,cs_Anorthite
_beforetwins),Miller(0,1,0,cs_Anorthite_beforetwins)];
o_Anorthite_beforetwins = grains_smoothed_pl('Anorthite').meanOrientation;

h_axes_Anorthite_beforetwins =[Miller(1,0,0,cs_Anorthite_beforetwins,'uvw'),
Miller(0,1,0,cs_Anorthite_beforetwins,'uvw'),Miller(0,0,1,cs_Anorthite_beforetwins,'uvw'),Miller(1,0,1,c
s_Anorthite_beforetwins,'uvw'),Miller(1,1,0,cs_Anorthite_beforetwins,'uvw')];
o_axes_Anorthite_beforetwins = grains_smoothed_pl('Anorthite').meanOrientation;

%Anorthite_merged
cs_Anorthite_merged = ebsd_merged('Anorthite').CS;
h_Anorthite_merged=[Miller(0,0,1,cs_Anorthite_merged),
Miller(1,0,0,cs_Anorthite_merged),Miller(1,1,1,cs_Anorthite_merged),Miller(1,1,0,cs_Anorthite_merged
),Miller(0,1,0,cs_Anorthite_merged)];
o_Anorthite_merged = mergedGrains('Anorthite').meanOrientation;

h_axes_Anorthite_merged =[Miller(1,0,0,cs_Anorthite_merged,'uvw'),
Miller(0,1,0,cs_Anorthite_merged,'uvw'),Miller(0,0,1,cs_Anorthite_merged,'uvw'),Miller(1,0,1,cs_Anort
hite_merged,'uvw'),Miller(1,1,0,cs_Anorthite_merged,'uvw')];
o_axes_Anorthite_merged = mergedGrains('Anorthite').meanOrientation;

% Plotting
figure
plotPDF(o_Anorthite_beforetwins,h_Anorthite_beforetwins,'uer','projection','eangle','contourf');
CLim(gcm,'equal');
mtexColorbar
%set(gcf,'Position',fig_resolution)
export_fig 'STITCHED_LE_RI_5570_NR Anorthite_beforetwins planes.png' -m1 -transparent
close(figure)
figure
plotPDF(o_axes_Anorthite_beforetwins,h_axes_Anorthite_beforetwins,'uer','projection','eangle','contourf'
);
CLim(gcm,'equal');
mtexColorbar
%set(gcf,'Position',fig_resolution)
export_fig 'STITCHED_LE_RI_5570_NR Anorthite_beforetwins axes.png' -m1 -transparent
close(figure)
```

```
figure
plotIPDF(odfbeforetwins,[xvector,yvector,zvector],'antipodal','resolution',1*degree,'contourf','colorrange',
'equal');
mtexColorbar('location','eastOutSide','title','mud');
%set(gcf,'Position',fig_resolution)
export_fig 'STITCHED_LE_RI_5570_NR odfAnorthite_beforetwins IPF.png' -m1 -transparent
close(figure)

% Plotting
figure
plotPDF(o_Anorthite_merged,h_Anorthite_merged,'uer','projection','eangle','contourf');
CLim(gcm,'equal');
mtexColorbar
%set(gcf,'Position',fig_resolution)
export_fig '1STITCHED_LE_RI_5570_NR Anorthite_merged planes.png' -m1 -transparent
close(figure)
figure
plotPDF(o_axes_Anorthite_merged,h_axes_Anorthite_merged,'uer','projection','eangle','contourf');
CLim(gcm,'equal');
mtexColorbar
%set(gcf,'Position',fig_resolution)
export_fig 'STITCHED_LE_RI_5570_NR Anorthite_merged axes.png' -m1 -transparent
close(figure)
figure
plotIPDF(odfmerged,[xvector,yvector,zvector],'antipodal','resolution',1*degree,'contourf','colorrange','equ
al');
mtexColorbar('location','eastOutSide','title','mud');
%set(gcf,'Position',fig_resolution)
export_fig 'STITCHED_LE_RI_5570_NR odfAnorthite_merged IPF.png' -m1 -transparent
close(figure)
%}
%% Groundmass differentiation by size
% this section generates an orientation distribution function for groups of
% grains and plots them as contoured pole figures

load 'STITCHED_LE_RI_5570_NR_merged_grains.mat'
load 'STITCHED_LE_RI_5570_NR_grains_pl.mat'

% quick log of how many grains are in the 'porphyroclast' and 'groundmass'
% groups for both the pre-merged and merged grain sets

diary('STITCHED_LE_RI_5570_NR_grains_pl sizes.txt')

groundmass_condition_notwins = grains_pl.diameter>=150;
porphyroclast_condition_notwins= grains_pl.diameter<150;

groundmass_grains_notwins = grains_pl(groundmass_condition_notwins)
porphyroclast_grains_notwins = grains_pl(porphyroclast_condition_notwins)

diary off
diary('STITCHED_LE_RI_5570_NR_merged_grains sizes.txt')
```

```
groundmass_condition = mergedGrains.diameter<=150;
porphyroclast_condition= mergedGrains.diameter>150;

groundmass_grains = mergedGrains(groundmass_condition)
porphyroclast_grains = mergedGrains(porphyroclast_condition)

diary off
%}

% generate the ODF using the same strategy as the above section

psi_groundmass = calcKernel(groundmass_grains('Anorthite').meanOrientation)
psi_porphyroclast = calcKernel(porphyroclast_grains('Anorthite').meanOrientation)

odfgroundmass = calcODF(groundmass_grains('Anorthite').meanOrientation,psi_groundmass);
odfporphyroclast = calcODF(porphyroclast_grains('Anorthite').meanOrientation,psi_porphyroclast);

odfgroundmass10 = calcODF(groundmass_grains('Anorthite').meanOrientation,'halfwidth',10*degree);
odfporphyroclast10 =
calcODF(porphyroclast_grains('Anorthite').meanOrientation,'halfwidth',10*degree);

save('STITCHED_LE_RI_5570_NR_groundmass_grains','groundmass_grains');
save('STITCHED_LE_RI_5570_NR_porphyroclast_grains','porphyroclast_grains');
save('STITCHED_LE_RI_5570_NR_odf','odfgroundmass','odfporphyroclast');

%% Texture indicies and grain info
close all
clear all

load 'STITCHED_LE_RI_5570_NR_merged_grains.mat'
load 'STITCHED_LE_RI_5570_NR_porphyroclast_grains.mat'
load 'STITCHED_LE_RI_5570_NR_groundmass_grains.mat'
load 'STITCHED_LE_RI_5570_NR_odf.mat'

%Generate J and M texture indicies for the odfs just created
diary('STITCHED_LE_RI_5570_NR_merged_grains Texture Indicies.txt')

groundmass_M = calcMIndex(odfgroundmass)
groundmass_J =textureindex(odfgroundmass)

porphyroclast_M = calcMIndex(odfporphyroclast)
porphyroclast_J = textureindex(odfporphyroclast)

diary off

% mean values and standard deviations of physical properties of grains
diary('STITCHED_LE_RI_5570_NR_merged_grains various mean physical measurements.txt')

groundmass_grains_mean_diameter=2*(mean(equivalentRadius(groundmass_grains('Anorthite'))))
groundmass_grains_mean_diameter_std=2*(std(2*(equivalentRadius(groundmass_grains('Anorthite')))))
groundmass_grains_mean_aspectratio=mean(groundmass_grains('Anorthite').aspectRatio)
```

```
groundmass_grains_mean_aspectratio_std=2*(std(groundmass_grains('Anorthite').aspectRatio))

porphyroclast_grains_mean_diameter=2*(mean(equivalentRadius(porphyroclast_grains('Anorthite'))))
porphyroclast_grains_mean_diameter_std=2*(std(2*(equivalentRadius(porphyroclast_grains('Anorthite'))
)))
porphyroclast_grains_mean_aspectratio=mean(porphyroclast_grains('Anorthite').aspectRatio)
porphyroclast_grains_mean_aspectratio_std=2*(std(porphyroclast_grains('Anorthite').aspectRatio))

diary off

% Lists of equal area ellipse properties
[omega,a,b]= principalComponents(groundmass_grains);

%Groundmass grains
diary('STITCHED_LE_RI_5570_NR groundmass grains ellipse principal components (grain
id,long,short).txt')
groundmass_grains_equalareaellipse_principal_components = [groundmass_grains.id,a,b]
diary off

diary('STITCHED_LE_RI_5570_NR groundmass grains aspect ratio.txt')
groundmass_grains_AR = aspectRatio(groundmass_grains)
groundmass_grains_aspectratio = [groundmass_grains.id,groundmass_grains_AR]
diary off

diary('STITCHED_LE_RI_5570_NR groundmass grains longest line inside grain (not ellipse).txt')
groundmass_grains_LL = diameter(groundmass_grains)
groundmass_grains_longest_line = [groundmass_grains.id,groundmass_grains_LL]
diary off

%Porphyroclast grains

[omega,a,b]= principalComponents(porphyroclast_grains);

diary('STITCHED_LE_RI_5570_NR porphyroclast grains ellipse principal components (grain
id,long,short).txt')
porphyroclast_grains_equalareaellipse_principal_components = [porphyroclast_grains.id,a,b]
diary off

diary('STITCHED_LE_RI_5570_NR porphyroclast grains aspect ratio.txt')
porphyroclast_grains_AR = aspectRatio(porphyroclast_grains)
porphyroclast_grains_aspectratio =  [porphyroclast_grains.id,porphyroclast_grains_AR]
diary off

diary('STITCHED_LE_RI_5570_NR porphyroclast grains longest line inside grain (not ellipse).txt')
porphyroclast_grains_LL = diameter(porphyroclast_grains)
porphyroclast_grains_longest_line = [porphyroclast_grains.id,porphyroclast_grains_LL]
diary off

%% Grain ID plotting
load 'STITCHED_LE_RI_5570_NR_merged_grains.mat'
load 'STITCHED_LE_RI_5570_NR_porphyroclast_grains.mat'
```

```
load 'STITCHED_LE_RI_5570_NR_groundmass_grains.mat'

fig_resolution = [0 0 1200 650];

figure
plot(groundmass_grains('Anorthite'),groundmass_grains('Anorthite').meanOrientation,'micronbar','off')
text(groundmass_grains('Anorthite'),int2str(groundmass_grains('Anorthite').id))
%set(gcf,'Position',fig_resolution)
%export_fig 'STITCHED_LE_RI_5570_NR Groundmass Grains Grain IDs.png'


figure
plot(porphyroclast_grains,porphyroclast_grains.meanOrientation,'micronbar','off')
text(porphyroclast_grains,int2str(porphyroclast_grains.id))
%set(gcf,'Position',fig_resolution)
%export_fig 'STITCHED_LE_RI_5570_NR Porphyroclast Grains Grain IDs.png'

%{
% explictly define the crystallographic planes and axes that you're
% interested in seeing plotted
%
%Anorthite_groundmass
cs_Anorthite_groundmass = ebsd_filled_pl('Anorthite').CS;
h_Anorthite_groundmass=[Miller(0,0,1,cs_Anorthite_groundmass),
Miller(1,0,0,cs_Anorthite_groundmass),Miller(1,1,1,cs_Anorthite_groundmass),Miller(1,1,0,cs_Anorthit
e_groundmass),Miller(0,1,0,cs_Anorthite_groundmass)];
o_Anorthite_groundmass = groundmass_grains('Anorthite').meanOrientation;

h_axes_Anorthite_groundmass =[Miller(1,0,0,cs_Anorthite_groundmass,'uvw'),
Miller(0,1,0,cs_Anorthite_groundmass,'uvw'),Miller(0,0,1,cs_Anorthite_groundmass,'uvw'),Miller(1,0,1,c
s_Anorthite_groundmass,'uvw'),Miller(1,1,0,cs_Anorthite_groundmass,'uvw')];
o_axes_Anorthite_groundmass = groundmass_grains('Anorthite').meanOrientation;

%Anorthite_porphyroclast
cs_Anorthite_porphyroclast = ebsd_filled_pl('Anorthite').CS;
h_Anorthite_porphyroclast=[Miller(0,0,1,cs_Anorthite_porphyroclast),
Miller(1,0,0,cs_Anorthite_porphyroclast),Miller(1,1,1,cs_Anorthite_porphyroclast),Miller(1,1,0,cs_Anort
hite_porphyroclast),Miller(0,1,0,cs_Anorthite_porphyroclast)];
o_Anorthite_porphyroclast = porphyroclast_grains('Anorthite').meanOrientation;

h_axes_Anorthite_porphyroclast =[Miller(1,0,0,cs_Anorthite_porphyroclast,'uvw'),
Miller(0,1,0,cs_Anorthite_porphyroclast,'uvw'),Miller(0,0,1,cs_Anorthite_porphyroclast,'uvw'),Miller(1,0
,1,cs_Anorthite_porphyroclast,'uvw'),Miller(1,1,0,cs_Anorthite_porphyroclast,'uvw')];
o_axes_Anorthite_porphyroclast = porphyroclast_grains('Anorthite').meanOrientation;

%{
% Plotting
figure
plotPDF(o_Anorthite_groundmass,h_Anorthite_groundmass,'uer','projection','eangle','contourf');
CLim(gcm,'equal');
mtexColorbar
```

```
%set(gcf,'Position',fig_resolution)
export_fig 'STITCHED_LE_RI_5570_NR Anorthite_groundmass planes.png' -m1 -transparent
close(figure)
figure
plotPDF(o_axes_Anorthite_groundmass,h_axes_Anorthite_groundmass,'uer','projection','eangle','contourf
');
CLim(gcm,'equal');
mtexColorbar
%set(gcf,'Position',fig_resolution)
export_fig 'STITCHED_LE_RI_5570_NR Anorthite_groundmass axes.png' -m1 -transparent
close(figure)
figure
plotIPDF(odfgroundmass,[xvector,yvector,zvector],'antipodal','resolution',1*degree,'contourf','colorrange'
,'equal');
mtexColorbar('location','eastOutSide','title','mud');
%set(gcf,'Position',fig_resolution)
export_fig 'STITCHED_LE_RI_5570_NR odfAnorthite_groundmass IPF.png' -m1 -transparent
close(figure)

% Plotting
figure
plotPDF(o_Anorthite_porphyroclast,h_Anorthite_porphyroclast,'uer','projection','eangle','contourf');
CLim(gcm,'equal');
mtexColorbar
%set(gcf,'Position',fig_resolution)
export_fig '1STITCHED_LE_RI_5570_NR Anorthite_porphyroclast planes.png' -m1 -transparent
close(figure)
figure
plotPDF(o_axes_Anorthite_porphyroclast,h_axes_Anorthite_porphyroclast,'uer','projection','eangle','cont
ourf');
CLim(gcm,'equal');
mtexColorbar
%set(gcf,'Position',fig_resolution)
export_fig 'STITCHED_LE_RI_5570_NR Anorthite_porphyroclast axes.png' -m1 -transparent
close(figure)
figure
plotIPDF(odfporphyroclast,[xvector,yvector,zvector],'antipodal','resolution',1*degree,'contourf','colorrang
e','equal');
mtexColorbar('location','eastOutSide','title','mud');
%set(gcf,'Position',fig_resolution)
export_fig 'STITCHED_LE_RI_5570_NR odfAnorthite_porphyroclast IPF.png' -m1 -transparent
close(figure)
%}
%% Grain C-axis orientations
% this section just produces .txt files reporting the orientations of
% c-axes for each grain in the groundmass and porphyroclast grain sets
% produced earlier, in both a cartesian coordinate system locked to the
% directions of the map XYZ, and in polar coordinates in case one is more
% convenient to use than another. Essentially no new information here -
% all of this is what is visible in the pole figure for the C-axis.
%{
```

```
load 'STITCHED_LE_RI_5570_NR_merged_grains.mat'
load 'STITCHED_LE_RI_5570_NR_porphyroclast_grains.mat'
load 'STITCHED_LE_RI_5570_NR_groundmass_grains.mat'

CS = crystalSymmetry('-1', [8.1797 12.8748 14.1721], [93.13,115.89,91.24]*degree, 'X||a*', 'Z||c');

% groundmass
diary('STITCHED_LE_RI_5570_NR groundmass_grains.txt')
groundmass_grains('Anorthite')
diary off
groundmass_Caxes= groundmass_grains('Anorthite').meanOrientation*Miller(0,0,1,CS);
diary('STITCHED_LE_RI_5570_NR groundmass_grains [001] Cartesian.txt')
groundmass_Caxes.xyz
diary off
diary('STITCHED_LE_RI_5570_NR groundmass_grains [001] Polar.txt')
[theta,rho,r] = polar(groundmass_Caxes)
diary off

figure
plot(groundmass_Caxes,'antipodal','markersize',2)
annotate([vector3d.X,vector3d.Y,vector3d.Z],'label',{'X','Y','Z'},'backgroundcolor','w')
export_fig 'STITCHED_LE_RI_5570_NR groundmass_Caxes.png' -m1 -transparent

% porphyroclasts
diary('STITCHED_LE_RI_5570_NR porphyroclast_grains.txt')
porphyroclast_grains('Anorthite')
diary off
porphyroclast_Caxes= porphyroclast_grains('Anorthite').meanOrientation*Miller(0,0,1,CS);
diary('STITCHED_LE_RI_5570_NR porphyroclast_grains [001] Cartesian.txt')
porphyroclast_Caxes.xyz
diary off

diary('STITCHED_LE_RI_5570_NR porphyroclast_grains [001] Polar.txt')
[theta,rho,r] = polar(porphyroclast_Caxes)
diary off

figure
plot(porphyroclast_Caxes,'antipodal','markersize',2)
annotate([vector3d.X,vector3d.Y,vector3d.Z],'label',{'X','Y','Z'},'backgroundcolor','w')
export_fig 'STITCHED_LE_RI_5570_NR porphyroclast_Caxes.png' -m1 -transparent

%}
%}
```